

MICROMACHINED PDMS ELASTIC POST ARRAYS FOR STUDYING VASCULAR
SMOOTH MUSCLE CELLS

A Thesis

presented to

the Faculty of the Graduate School
at the University of Missouri-Columbia

In Partial Fulfillment

of the Requirements for the Degree

Doctor of philosophy

by

QI CHENG

Dr. Mahmoud Almasri, Thesis Supervisor

MAY 2011

The undersigned, appointed by the dean of the Graduate School,
have examined the dissertation entitled
MICROMACHINED PDMS ELASTIC POST ARRAYS FOR STUDYING VASCULAR SMOOTH
MUSCLE CELLS

Presented by Qi Cheng

**A candidate for the degree of philosophy, doctor of electrical and computer
engineering and hereby certify that, in their opinion, it is worthy of acceptance.**

Dr. Mahmoud Almasri

Dr. Gerald Meininger

Dr. Kevin Gillis

Dr. Guilherme DeSouza

Dr. Naz Islam

ACKNOWLEDGEMENTS

There are many people whose assistance and support are invaluable in both my research and otherwise. First and most, I would like to thank my PhD advisor Mahmoud Almasri, his continuous guidance, support and encouragement during my PhD have made for a truly pleasant and unforgettable experience as well as been as a generator of my inspiration. I would also like to thank Dr. Gerald A. Meininger for his continuous support during my PhD study. In the meantime, I would like to thank to Dr. Zhe Sun for his direct, patient and effective help during my PhD study. I would like to thank my committee members, Dr. Gerald A. Meininger, Dr. Kevin Gillis, Dr. Guilherme DeSouza and Dr. Naz Islam for reviewing my thesis and comprehensive proposal and making guiding comments. I would also give special thanks to my research fellows, Yifan Wu, Jie Lin, Wenchuan Qi, and Muhammad Hai for their help.

My parents and my parents in law helped me by proving financial and especially mental support during my PhD study. I would like to thank them along with my brother Gang Cheng. Finally, I would give my sincere thanks to my wife for her standing along closely with me all the time during my PhD study; thanks to her encouragement and advice which make me keep moving forward.

February 21, 2011

ABSTRACT

Author: Cheng, Qi

Advisor: Dr. Almasri, Mahmoud

This thesis describes the design, modeling, fabrication and characterization of a micromachined array of high density 3-dimensional microposts (100×100) made of flexible material (silicone elastomers) for use to measure quantitatively the cellular traction force generated by vascular smooth muscle cell (VSMC) with high sensitivity and accuracy. The performance of the microposts with base and without base has been carefully analyzed by finite element analysis (FEA) software Coventorware™. The micropost arrays were then fabricated with diameters ranged from 3 to 10 μm , with edge to edge spacing of 5 and 7 μm , and with a height to diameter aspect ratio up to 13 using microfabrication techniques and replica molding. The mechanical properties of the Polydimethylsiloxane (PDMS) microposts with various geometries used in the cell culture experiment were determined experimentally including detailed measurements of Young's modulus (E) and the corresponding spring constant. We have found that microposts with different sizes and geometries have different Young's modulus and spring constant values, ranged between 0.534-1.38 MPa, and 0.44 pN/nm-11.72 nN/nm, respectively.

Vascular smooth muscle cells isolated from male Sprague-Dawley rats (250-350 g) were cultured on top of the micropost arrays and incubated for 2 days before an image acquisition

experiment. The micropost array was then scanned by phase contrast microscope from top to bottom. The ‘top’ and ‘bottom’ images were obtained by focusing on either top or bottom of the micropost. The outlines of the micropost covered by VSMC were successfully recorded as optical images and extracted using image processing in Matlab. The direction and the amplitude of microposts deflections were determined by comparing center location of micropost in ‘top’ and ‘bottom’ images. Hence, the corresponding force generated by cell can be calculated from deviation of the central axis of the micropost (i.e. the top vs. bottom). The force distribution map of a single VSMC was generated using the PDMS micropost array. A minimum displacement of 200 nm can be detected from optical images captured by confocal microscope. For example, micropost with highest aspect ratio (diameter, and height of 3 μm , and 35 μm) can detect the smallest traction force of 38 pN/ μm . The micropost arrays with different geometries were used to study VSMCs. We have also found that the traction force exerted by VSM cell increases as the stiffness of the micropost increases. It demonstrates that VSM cell tends to adjust its traction force to adapt to its physical environment.

VSMCs with integrin-linked kinase enzyme (ILKE), referred to as CK₄ cell, and without ILK module, referred as ILK cell, were also studied using PDMS micropost array. Both cells were able to deflect or pull the microposts towards their physical center. They were also studied in the presence of Angiotensin II (ANGII), a potent VSM contractile agent, and Cytochalasin-D (CYTO), an actin depolymerizing agent. The results demonstrate that the addition of ANGIO protein leads to contraction of CK₄ cell while the ILK cells fail to evoke the contractile response. The VSMC’s contraction disappeared by 6-10 minutes after the ANGIO treatment and the cell

recovered its original morphology. CK₄ cells showed significant relaxation within 15 minutes after adding CYTO to cell bath. Similarly, the ILK cells relaxed in the presence of ANGII and CYTO. No contraction behavior was found out from ILK cells during the experiment. It has also been found that both CK₄ and ILK cells tend to exert larger traction force when they grow on stiffer micropost array. Moreover, the traction forces generated by CK₄ cells are more than 80% larger than that generated by ILK cells when the same size of micropost arrays were used. This study indicates that the function of ILK molecule is involved to the VSMC contraction and the control its traction force.

Finally, high temporal resolution analysis of CK₄ cells was performed on PDMS micropost array. The VSMCs demonstrated that traction sites in CK₄ cells attached to individual microposts ‘oscillate’ when cells were in the resting states. Such behavior becomes noticeable by observing the movement of micropost’s free end in real time. The analysis showed that the oscillation of VSMC has different constant periods. The oscillation was also observed when external stimulation of ANGII and CYTO were added. This analysis showed that the amplitude and the period of oscillation are changeable under the external stimulus. Further work needed to understand the mechanism and significance of the oscillating behavior.

TABLE OF CONTENTS

ACKNOWLEDGEMENTS.....	ii
ABSTRACT.....	iii
TABLE OF FIGURES.....	xi
TABLE OF TABLES.....	xvii
1. INTRODUCTION	1
1.1 OVERVIEW OF BIOMEMS APPLICATIONS	1
1.2 PDMS SUBSTRATE AS A FORCE SENSOR.....	2
1.3 MICROPROBE BASED SENSORS FOR TRACTION FORCE STUDY	3
1.4 MICROCANTILEVER BASED SENSOR FOR TRACTION FORCE STUDY.....	5
1.5 PDMS AS MATERIAL FOR BIOMEMS.....	5
1.6 OUTLINE OF THIS THESIS	7
2. VASCULAR SMOOTH MUSCLE CELLS.....	8
2.1 VASCULAR SMOOTH MUSCLE CELL	8

2.2	PROLIFERATION AND MIGRATION OF VASCULAR SMOOTH MUSCLE CELL	10
2.3	CELL'S TRACTION FORCE STUDY	13
3.	PDMS MICROPOST ARRAY	18
3.1	DESIGN OF PDMS MICROPOST ARRAY	18
3.2	STRUCTURAL AND MECHANICAL ANALYSIS	19
3.2.1	THEORETICAL MECHANICS	19
3.2.2	MODELING AND SIMULATION OF PDMS MICROPOST	20
3.2.3	MECHANICAL AND STRUCTURAL MODELING	24
3.3	CONCLUSION	27
4.	FABRICATION AND CALIBRATION OF PDMS MICROPOST	28
4.1	FABRICATION OF HIGH ASPECT RATIO PDMS MICROPOST ARRAY	28
4.1.1	PHOTORESIST PATTERNING	30
4.1.2	DEEP REACTIVE ION ETCHING (DRIE)	30
4.1.3	DRIE PROCESS AND HIGH ASPECT RATIO SILICON MICROMOLD	32

4.1.4	PDMS PREPARATION AND MICROMOLD SURFACE TREATMENT	35
4.2	CALIBRATION OF PDMS MICROPOST	42
4.2.1	ATOMIC MICROSCOPE (AFM)	43
4.2.2	CALIBRATION EXPERIMENT	43
A.	PREPARATION OF SAMPLE FOR CALIBRATION	43
B.	CALIBRATION SYSTEM SETUP	45
C.	LOCATING MICROPOST FREE END WITH AFM TIP	47
D.	CALIBRATION RESULTS ANALYSIS AND ITS SIGNIFICANCE	48
4.3	CONCLUSION	57
5.	STUDIES ON TRACTION FORCE OF VASCULAR SMOOTH MUSCLE CELL ON MICROPOST ARRAY	58
5.1	PREPARATION OF BIOLOGICAL STUDY	59
5.1.1	CONFOCAL MICROSCOPE AND EXPERIMENT SETUP	59
5.1.2	DEVICE PREPARATION AND CELL CULTURING EXPERIMENT	60
5.1.3	IMAGE PROCESSING	62

B.	IMAGE PROCESSING OF THE ‘BOTTOM’ IMAGE	63
C.	IMAGE PROCESSING OF ‘TOP IMAGE’	68
5.2	STEADY REACTION OF VSMC USING MICROPOST ARRAY	73
5.2.1	VALIDATION OF THE MICROPOST FORCE SENSOR.....	73
5.2.2	STEADY STATE RESPONSE OF VSMC TO MICROPOST ARRAY WITH DIFFERENT STIFFNESS.....	77
5.3	CONCLUSION.....	90
6.	TRANSIENT RESPONSE STUDY OF VSMC USING MICRIPOST ARRAY	92
6.1	EXPERIMENT PREPARATION AND DESIGN.....	92
6.2	TRANSIENT RESPONSE OF VASCUALR SMOOTH MUSCLE CELL IN NORMAL CONDITION.....	96
6.3	TRANSIENT RESPONSE OF VASCUALR SMOOTH MUSCLE CELL UNDER STIMULUS OF ANGII.....	100
6.4	TRANSIENT RESPONSE OF VASCUALR SMOOTH MUSCLE CELL UNDER STIMULUS OF CYTOCHALASIN	104
6.5	TRANSIENT RESPONSE OF A SINGLE VASCUALR SMOOTH MUSCLE CELL AT MULTI-LOCATIONS	108

6.6	CONCLUSIONS.....	110
7.	SUMMARY AND CONCLUSION	111
7.1	HIGH ASPECT RATIO PDMS MICROPOST FORCE SENSOR ARRAY.....	111
7.2	THE STUDY OF LONG TERM MECHANICAL RESPONSE OF VSMC USING PDMS MICROPOST ARRAY.....	112
7.3	THE STUDY OF TRANSIENT RESPONSE OF VSMC USING PDMS MICROPOST ARRAY	113
	REFERENCE.....	115
	VITA.....	129

TABLE OF FIGURES

Figure 1.1 Microprobe based force sensors to measure cell force: a) Schematic b) SEM image [44].....	4
Figure 1.2 SEM images of cells growing on biosensors with vertical cantilevers: a) rat aorta SMCs adhering to the top of PDMS micropost arrays [44], b) human mesenchymal stem cells [46].....	6
Figure 2.1 Different types of cell in blood vessel [57]	9
Figure 3.1. 3-D view of the micropost without PDMS base.....	21
Figure 3.2. 3-D view of the micropost with PDMS base.....	22
Figure 3.3. The relationship between simulation error and mesh size.....	23
Figure 3.4. The micropost deflection and the lateral force applied on the top of the micropost ..	24
Figure 3.5. The relationship between micropost displacement and its diameter	25
Figure 3.6. The relationship between micropost displacement and its height	26
Figure 4.1. Procedures of fabricating PDMS micropost array.....	29
Figure 4.2. Schematic of DRIE system.....	32
Figure 4.3. Profile of micromold after DRIE process.....	34
Figure 4.4. Profile of micromolds with different size after DRIE process	35

Figure 4.5. Initial fabricated micropost array with most of the posts stuck in the micromold	36
Figure 4.6. SEM micrograph of PDMS micropost array with 7 μm of diameter and 25 μm of height.....	39
Figure 4.7. SEM micrograph of PDMS micropost array with a) 7 μm of diameter, 5 μm of height and 7 μm spacing; b) 3 μm of diameter 30 μm of height and 5 μm of spacing	40
Figure 4.8. SEM top view of PDMS micropost array with a) 7 μm of diameter, and 7 μm spacing; b) 3 μm of diameter 10 μm of spacing	41
Figure 4.9. a) A row of microposts is cut from a micropost array for calibration; b) the SEM micrograph of a row of micropost with PDMS substrate	44
Figure 4.10. AFM tip touches the micropost free end during the calibration.....	45
Figure 4.11. Calibration system setup schematic.....	46
Figure 4.12. AFM tip with micropost during calibration.....	47
Figure 4.13. Deflection and force relation in calibration.....	49
Figure 4.14. Force-displacement characteristics of the AFM cantilever beam applying forces on	50
Figure 5.1. a) Schematic of cell experiment setup; b) extracting top and bottom images	61
Figure 5.2. Flow diagram of image processing.....	63

Figure 5.3. a) Image before processing, b) image after processing	65
Figure 5.4. The extracted outline of the micropost.....	66
Figure 5.5. Images after filling the outlines of the microposts with white color	67
Figure 5.6. The micropost mask after image processing	68
Figure 5.7. The ‘top’ image of a micropost with cell growing on top.....	69
Figure 5.8. The ‘top’ image of a micropost after first image processing.....	70
Figure 5.9. The ‘top’ micropost mask after processing	71
Figure 5.10. The mask of microposts in top image after filtering noise.....	72
Figure 5.11. a) phase contract image of one cell cultured micropost array with diameter, height and spacing of 7 μm , 25 μm and 3 μm ; b) and c) shows the extracted ‘bottom’ and ‘top’ images; d) traction force distribution map; e) and f) ‘masks’ of bottom and top images	74
Figure 5.12. Single VSMC grown on micropost array with two different geometries: (a) diameter, height and spacing of 7 μm , 15 μm and 7 μm , respectively (b) diameter, height and spacing of 3 μm , 25 μm and 5 μm , respectively	75
Figure 5.13. Wide-field optical images of single VSMC grown on micropost array with diameter, height and spacing of 5 μm , 25 μm and 7 μm , respectively: (a) recorded at top of the micropost array (b) recorded at bottom of the micropost array, respectively.....	76

Figure 5.14. White field optical images of single CK₄ cell grown on micropost array with a) 3 μ m in diameter, 25 μ m in height and b) 5 μ m in diameter, 25 μ m in height, respectively. The arrow's length in figure 7a is magnified 8 times to make it long enough to be seen..... 78

Figure 5.15. Traction as a function of the spring constant of the micropost a) @ the edge of the cell and b) @ the center of the cell. 81

Figure 5.16. White field optical images of single CK4 cell: a) before adding ANGII and b) 3 minutes after adding ANGII c) 6 minutes after adding ANGII and d) 20 minutes after adding ANGII and e) 30 minutes after adding CYTO..... 83

Figure 5.17. The traction force of CK4 cell applied on post 1 84

Figure 5.18. Wide-field optical images of single ILK cell growing on micropost array with a) 3 μ m in diameter, 25 μ m in height and b) 5 μ m in diameter, 25 μ m in height, respectively. The arrow's length in figure 7a is magnified 8 times to make it long enough to be seen 86

Figure 5.19. Wide-field optical images of single ILK cell: : a) before adding ANGII and b) 3 minutes after adding ANGII c) 6 minutes after adding ANGII and d) 20 minutes after adding ANGII and e) 30 minutes after adding CYTO..... 88

Figure 5.20. The traction force of ILK cell applied on post 1 89

Figure 6.1 Optical micrograph of a VSMC grown on micropost array 95

Figure 6.2 Transient response with sampling interval of 96 seconds 96

Figure 6.3 Transient response with sampling interval of 48 seconds	97
Figure 6.4 Transient response with sampling interval of 48 and 96 seconds	98
Figure 6.5 Transient response with different period.....	98
Figure 6.6 Transient responses with different sampling interval.....	99
Figure 6.7 Transient response with different vibration period	99
Figure 6.8 Transient response with 96 seconds sampling interval	100
Figure 6.9 Transient response with 48 seconds sampling interval	101
Figure 6.10 Transient response with 96 second sampling interval.....	102
Figure 6.11 Transient response with higher vibrating frequency	102
Figure 6.12 Transient response with higher vibrating frequency	103
Figure 6.13 Transient response with 48 seconds sampling interval	103
Figure 6.14 Transient responses with 96 seconds sampling interval.....	105
Figure 6.15 Transient responses with 48 seconds sampling interval.....	105
Figure 6.16 Transient response with higher vibrating frequency	106
Figure 6.17 Transient response with sampling interval of 48 seconds and 96 seconds.....	106

Figure 6.18 Transient response with high vibration frequency 107

Figure 6.19 Transient force change reflected by post 1 to 3.....108

TABLE OF TABLES

Table 3.1 Relationship between mesh configuration the simulation error	23
Table 4.1 Comparison of Bosch and Cryo processes	31
Table 4.2. The condition of bosch process	33
Table 4.3 Young's Modulus of large post measured with AFM Cantilever beams with a tetrahedron	49
Table 4.4 Young's Modulus of small post cured at room temperature for 24 hours	52
Table 4.5 Young's Modulus of small post cured at 65°C for 24 hours	53
Table 4.6 Young's Modulus of large post cured at room temperature for 24 hours.....	53
Table 4.7. Young's Modulus of large post cured at 65°C for 24 hours	54
Table 4.8 Average Young's modulus (E) of PDMS micropost as a function of size and	55
Table 4.9. Summary of the comparison and the corresponding p-value	55
Table 4.10. Spring constant of the micropost with different geometry	56
Table 5-1. Average deflection of the micropost and corresponding traction force generated by cells	79
Table 5.2 Traction force from the labeled posts as a function of observation time.....	80

Table 5.3 Average deflection of the micropost and corresponding traction force generated by cells on micropost array	87
Table 5.4 Traction force from the labeled posts as a function of observation time for ILK cell..	90
Table 6.1 Experiment description of cell's transient response study	94

1. INTRODUCTION

This chapter will discuss several biomedical applications of microelectromechanical system known as a BioMEMS. The mechanical properties of Polydimethylsiloxane (PDMS) will be presented. Microprobe and micro-cantilever force sensors will be described and compared. A general outline of the thesis will also be presented.

1.1 OVERVIEW OF BIOMEMS APPLICATIONS

MicroElectroMechanical System (MEMS) devices were fabricated using highly developed semiconductor fabrication techniques such as photolithography [1-3], reactive ion etching [4], deep reactive ion etching [5, 6], plasma enhanced chemical vapor deposition [7], ion implantation [8], and wet etching [9], which are extensively developed to create ultra/very large scale integrated circuits (U/VLSI) [10, 11]. Similar to microelectronics fabrication, MEMS fabrication techniques produce well-controlled electronic devices in size of millimeters to sub-micrometers. However, most distinctive feature of the MEMS devices is that they often have moving mechanical components which possess physical or analytical functions. Such functions were magnified to more readable forms such as optical, acoustic or electrical signal. A variety of MEMS gadgets and devices were fabricated and tested such as microreservoirs [12], micropump [13, 14], micromixer [15], cantilever [16-18], rotors [19], microchannels [20, 21], microvalve [22] and microsensors.

MEMS can be developed using biocompatible material for biological applications [23-26]. The advancement of manufacturing techniques resulted in more accurate and uniform

devices that can be used in biomedical and pharmaceutical research or industries. The research progress of BioMEMS such as ‘retinal’ implants for vision treatment [27], ‘neural’ implants for signal simulation and recoding from central nervous system [28] and microneedles for painless vaccination [29-31] were typical examples of tremendous progress of biological applications using BioMEMS. Furthermore, the ability of MEMS to work with low power and physiological conditions offer the promising future for these devices to be implemented in the body [32, 33].

1.2 PDMS SUBSTRATE AS A FORCE SENSOR

The ability of BioMEMS devices to act as force sensors to study traction forces of cells has been successfully fabricated and tested. In the 1980, Harris et al. [34] were the first being able to qualitatively observe cellular traction forces using deformable silicone substrate. The substrate showed wrinkles which reflect the strong traction forces exerted by motile fibroblasts. However, such devices could not measure and quantify the traction force due to the complex relationship between the size of the wrinkle and the amplitude of the generated forces. In order to improve the measurement quality, a new technique using elastic gels [35] was developed to avoid the problem mentioned above. A polyacrylamid (PA) gel was used to manipulate the stiffness of the substrate with no wrinkle pattern. Fluorescent beads were embedded into the gel and were used as markers of cell’s deformation when capturing optical images. There was still a drawback in such technique because the microbeads embedded in the substrate strongly affected the mechanical property of the substrate and the positions of such beads before doing experiment were difficult to control. Therefore, a regular array [36] instead of random spread microbeads was introduced as the embedded marker. Such substrates were prepared by microfabrication

techniques. The regular patterns such as micro-grids array [37, 38] were used to accurately measure the quantity and direction of the traction force exerted by different cells.

1.3 MICROPROBE BASED SENSORS FOR TRACTION FORCE STUDY

Recently, the extensive progress of microfabrication technology enabled the development of force microsensors for measurement of traction force of biological cells. Two types of microdevices were used for traction force study. The first was microprobe based force sensor which was used to measure cell traction force ranging from micro Newton to nano Newton level. The second device was a microcantilver beam based force sensor which will be discussed in the next section. The microprobes were used to evaluate the mechanical characteristics of muscle myofibrils or vascular smooth muscle cells [39-42]. Recently, researchers have implemented tungsten needles attached to steel foils to record isometric forces and rate constants of force generation from isolated cardiac myocytes [43]. Although such device made a progress in measuring traction force, its use was limited due to unstable oscillations and very low resonant frequency. Microprobes have also been developed to explore cell mechanical behavior under large deformations [44]. The sensor, (**Figure 1.1**), consisted of a probe and flexible beams, and normally measured cell force response in the range of 1nN to 1 μ N. Both the one (along the x-axis) and two-component (along the x-axis and y-axis) force sensors were developed, and were used in cell experiments. These experiments such as stretch force response, cell indentation force response, and in situ observation of the actin cytoskeleton during indentation showed the

versatility of the force sensors. The results provided significant insight into cell mechanical response under large deformations. The one-component force sensor consisted of a microprobe that contacted a cell, and attached to two parallel fixed flexible sensor beams. A force, F_x , deformed the beams by δ which was recorded optically from the relative displacements between a reference point and the microprobe. The force F_x equals $k\delta$, where k is the combined spring constant of the sensor beams. The sensor was held by a piezo stage that brought the probe in contact with a cell. However, such device had drawbacks. For example, it could not measure the traction force in multiple locations of a single cell at a time. Therefore, it was impossible to study the relationship between traction forces generated from different locations in a single cell. In addition, the fabrication of the device was complicated. There was a need for techniques to permit higher throughput measurements.

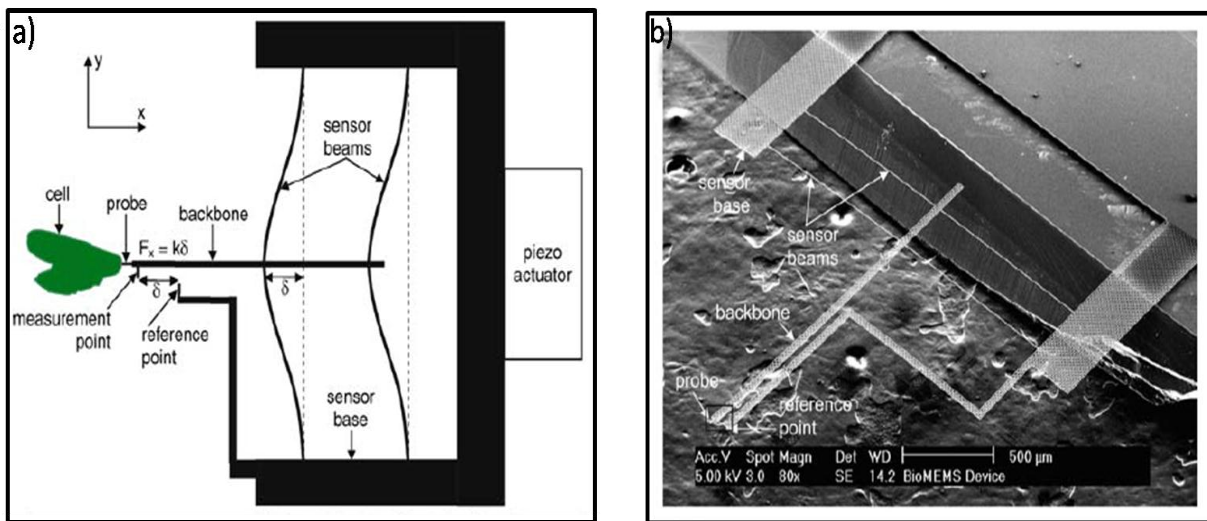


Figure 1.1 Microprobe based force sensors to measure cell force: a) Schematic
b) SEM micrograph [44]

1.4 MICROCANTILEVER BASED SENSOR FOR TRACTION FORCE STUDY

Microcantilever beams were also used for cell traction force study. The most significant feature of this device is that it transduces the physical structural deformation into unique traction force readings. Initially, a horizontal cantilever [45] was fabricated on a silicon wafer where the cell bends the cantilever in the direction of the applied traction forces. Since the sensor was not connected to the substrate directly, the deflection of the cantilever was related directly to the local force applied. The relationship between the force and the deflection was similar to that mentioned in 1.2. This device had a simple structure and resulted in quick force and deflection calculations. However, the horizontal design of the cantilever restricted the measurements of force along one direction. In other words, it could not measure traction forces at multi-location from a single cell. Modified design of micro-cantilever based force sensor used high-density array of vertical oriented cantilevers that improved both the spatial resolution of the force sensor and the multi-location measurement [46-52]. These devices were made of silicone and the single device in the array was a cylindrical cantilever formed from a microfabricated silicon or polymer mold. The new device measured the traction force in multi-direction and mapped the traction force of a single cell. The vertical cantilevers (**Figure 1.2**) were independent from each other and the measurement accuracy was significantly improved.

1.5 PDMS AS MATERIAL FOR BIOMEMS

Polydimethylsiloxane (PDMS), a relative transparent polymer with high flexibility and low stiffness, is composed of an alternating backbone of silicon and oxygen atoms with two

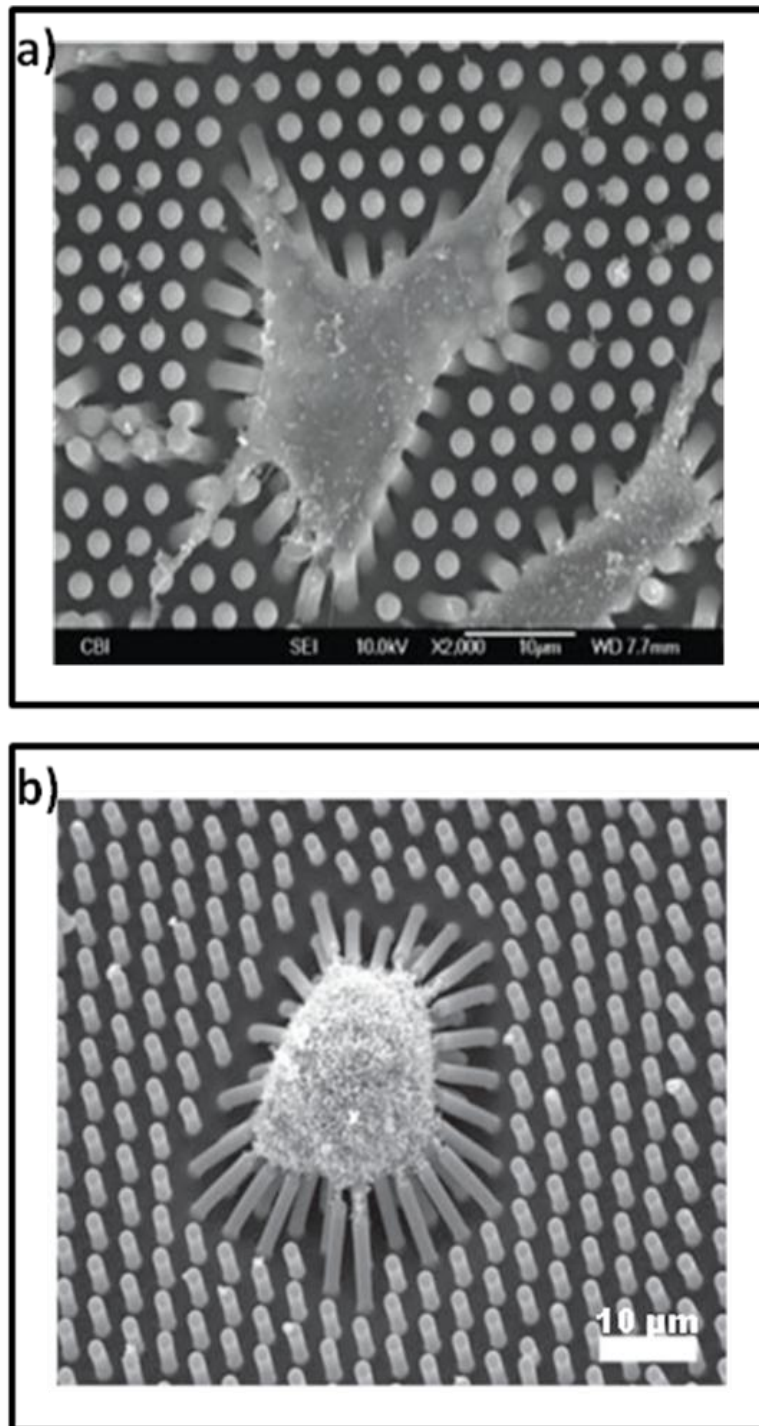


Figure 1.2 SEM images of cells growing on biosensors with vertical cantilevers: a) rat aorta SMCs adhering to the top of PDMS micropost arrays [44], b) human mesenchymal stem cells [46]

organic functionalities attached to each silicon atom [53]. It is also highly resistant to oxidation and chemical etch. Therefore, it is an ideal material for packaging. In addition, PDMS is biocompatible and is widely used in biological studies. It has already been used to make microchannel [54], micropost [48-50], and many other components in MEMS fabrication [55].

The stiffness of PDMS is greatly affected by the ratio of base and curing agent, temperature, feature size and etc. Its reconfigurable stiffness has been reported by many literatures with a wide varied value. The stiffness of PDMS has been extensively analyzed in this thesis and the factors determining the Young's modulus of PDMS has been discussed.

1.6 OUTLINE OF THIS THESIS

The first chapter of this thesis will provide introduction to BioMEMS devices, microscale force sensor and PDMS micropost arrays for cell traction force study. The second chapter will explain the purpose of this work and the biology of vascular smooth muscle cell. The third chapter will discuss the design, modeling, fabrication of PDMS micropost array. The theoretical calculation and experimental calibration of mechanical property of PDMS micropost including Young's modulus and spring constant will be described in details. Chapter four will describe the biological experiment of using PDMS micropost array for traction force study of VSMCs. The steady state responses of the cell in normal conditions and to external stimulus will be presented in detail. Chapter five and chapter six will describe the biological experiment using high aspect ratio PDMS micropost array for traction force study of VSMCs including transient state responses of the cell in normal conditions and to external stimulus. Finally, the conclusion of the thesis work will summarize the results in chapter seven.

2. VASCULAR SMOOTH MUSCLE CELLS

In this chapter, an overview of vascular smooth muscle cell including origin, structure, functionality, basic mechanism of cell's proliferation and migration will be described. A review of traction force generated by these cells will be presented.

2.1 VASCULAR SMOOTH MUSCLE CELL

The cardiovascular system is basically a circulation system in the human or animal body. It consists of a heart-similar to the water pump, a blood-similar to the water, and blood vessels-similar to water pipes. Blood vessels are divided into three types: arteries, veins, and capillaries. Their classification is similar to main or branch water pipe and forward or backward water pipe. During the blood circulation among this complex system, a diverse number of functions, including transporting blood, proteins, nutrients, oxygen, carbon dioxide, and other molecules, tissue regeneration and reorganization, developmental processes, thermoregulation, immune response, and wound healing are accomplished [56]. The vascular network covers the entire body to deliver the nutrition and energy. Therefore, it consists of both small and large vessels specifically designed to accommodate varying levels of blood flow and pressure, depending upon the location within the body. In addition, vascular tissue are made of a diverse population of cells, including endothelial cells, smooth muscle cells, fibroblasts, and other connective tissue cell types (**Figure 2.1**) [57]. The combination of these cell types makes up the vascular tissue and forms tight connections between each other, which generate functionality of both passive and active properties and transport across the vessel wall.

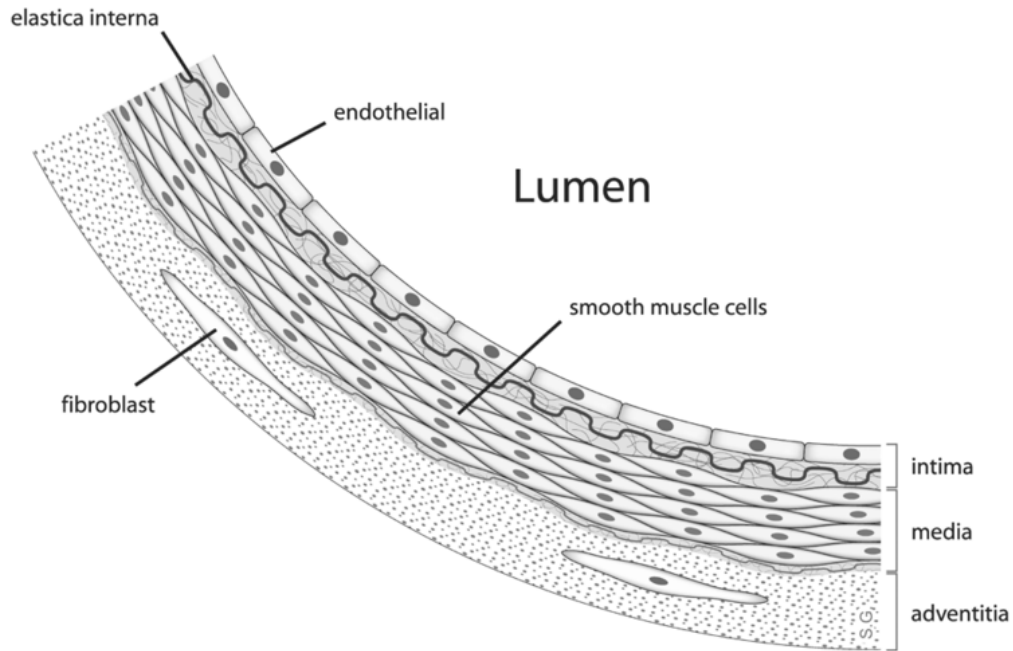


Figure 2.1 Different types of cell in blood vessel [57]

The vascular smooth muscle cells found within the vascular tissue are also involved in other activities critical to maintaining normal growth and function including providing an inner lining to the heart and blood vessels, providing secretion of bioactive molecules to affect local cellular environments, mediating angiogenesis and normal microvascular growth, transporting molecules from the blood to the interstitial fluid and interacting with adjacent smooth muscle cells during growth and external stimulus [54]. In addition, vascular smooth muscle cells play a critical role in normal tissue maintenance and growth. However, abnormal or uncontrolled vascular cell growth can be closely associated with diseases and processes such as angiogenesis, diabetic retinopathy, and other developmental conditions. The main purpose of the device development associated with this project is to provide new means to find biological clues, solutions and medical methods related to solve the malfunction of vascular smooth muscle cell.

2.2 PROLIFERATION AND MIGRATION OF VASCULAR SMOOTH MUSCLE CELL

Vascular injury and atherogenesis are associated with migration of smooth muscle cells [58, 59]. During atherogenesis, vascular smooth muscle (VSM) cells migrate to initiate formation of the intima distinct from the media or circulation [60]. Under such condition, VSMC's proliferation as well as migration from media to intima makes intima and media thicker. During vascular development, many cytokines play important role, such as platelet-derived growth factor (PDGF) which can control the reconstruction of vessel wall formation. It was demonstrated by the experiment on mice lacking PDGF or PDGF receptors failing to develop normal blood vessels [61]. It is important to note that the vascular smooth muscle cell's migration is a necessary process in vessel wall remodeling. Such conclusion had stimulated strong interest in cellular research of molecular mechanisms of vascular smooth muscle cell's migration contractility and mechanotransduction.

Cell's migration in vivo or in vitro begins with stimulation of cell surface receptors that convert the external signal to a series of coordinated remodeling events that alter the structure of the cytoskeleton. Many factors were able to promote or inhibit vascular smooth muscle cell's migration and proliferation. For example, small biogenic amines, peptide growth factors [59], cytokines, and extracellular matrix components [62] were strongly related to the cell's migration. Furthermore, physical factors including blood flow [63], shear stress, and matrix stiffness influenced VSM cell migration. Peptide growth factors were studied in some detail in the 1980s and early 1990s indicating that PDGF is a potent, efficient promoter for cell's migration. Later studies of PDGF receptor suggested that an important role of PDGF was to activate smooth

muscle cells to migrate and form blood vessels [64]. Other studies by Schwartz et al. [65] identified osteopontin as an important matrix component that promotes VSM migration. Osteopontin is a matrix glycoprotein containing an arginine-glycine-aspartic acid (RGD) motif. During atherogenesis or following vascular injury, osteopontin expression increases. There was a hypothesis that osteopontin enhances VSM migration via integrin signaling. It was demonstrated that integrin ligation to RGD was necessary for VSM adhesion to the external matrix. The promigratory agents mentioned above activated specific signal that trigger remodeling of the cytoskeleton network inside cell, changed the integrin adhesiveness of the cell to the matrix by adjusting proteins, and acting upon motor proteins. To migrate, VSM cells needed to detach the trailing edge by degrading focal contacts, and generated a force by myosin II in the body of the cell to propel the cell forward [54] and advance the leading edge.

Transient focal contacts between the cell membrane and extracellular matrix were necessary for migration to proceed after the initial stages of actin polymerization and focal contacts reduction at the leading edge which provided adhesion to the substrate and generated traction force for propulsion of the cell over or through the extracellular matrix [66, 67]. Degradation of mature focal contacts at the trailing edge was necessary for the cell to release from the matrix and move forward. The composition of focal contacts and mechanisms of initiation, maturation, and degradation were extensively studied in nonmuscle cells. The major components of focal contacts were described in migrating VSM cells including focal adhesion kinase (FAK) [68], vinculin [69], paxillin [70], tensin [71] and etc. Focal adhesion kinase was a critical regulator of cell migration that was upregulated following intimal hyperplasia. Formation

and degradation of focal contacts was intimately associated with signal transduction occurring during migration.

Integrin-linked kinase (ILK) is an important protein kinase that regulates cellular process such as differentiation, proliferation and cytoskeleton organization. It was demonstrated that ILK in VSMC linked to the cell contraction, spreading and adhesion. ILK was recently reported to modify several aspects of cytoskeletal and contractile protein function that could affect VSM cell migration. ILK interacts with the cytoplasmic tail of β integrins and serves as an adaptor protein. It binds several proteins linking integrins to the actin cytoskeleton, including affixin and paxillin [72, 73]. It also binds PINCH, an adaptor (particularly interesting new cysteine-histidine-rich protein), linking ILK to receptor tyrosine kinases and lipid kinases that promote VSM cell migration. The functions of ILK in VSM and their mechanism were not fully investigated, but ILK may alter cell motility by enhancing myosin light chain phosphorylation and activating myosin II motors. ILK can inactivate myosin phosphatase [74], and it can phosphorylate myosin light chains directly. Direct evidence of a role in VSM migration was provided by overexpressing dominant negative ILK, which blocks angiotensin II-stimulated migration.

Recently, several research groups have been studying migrations of vascular smooth muscle cell using 3 dimensional structures. Most studies of migration in 3 dimensions were based on 2 dimensional stiff substrates such as glass or porous polycarbonate membranes. Conditions for cell migration in vivo were very different. Cells interact with the matrix on all surfaces, not just on the basal surface. The shape of the cell and the types and kinetics of focal contacts may be fundamentally different compared to 2-D experimental condition. For example,

fibroblasts embedded in 3D matrices form focal contacts using a more limited set of integrins than cells in 2D matrices [75]. This might result from differences in matrix stiffness that alter mechanical signaling from the matrix [76].

Shape and structure of vascular smooth muscle cells are changing dynamically due to the response to variation of the chemical and physical environment. Such morphological changes during cell activities such as migration, proliferation, division and transport were found to have a regular behavior. It was proved that the cytoskeleton, the physical and biochemical interface were closely related to a large variety of cellular processes. Such processes were conducted by changing the mechanical properties of vascular smooth muscle cell through its cytoskeleton network. The network that consisted of actin filaments, microtubules, intermediated filaments and cytoplasmic proteins within the cytoskeleton was able to arrange and maintain the intracellular structure, build the connection between cell and its external environment, and generated appropriate forces to enable regular activity. The relationship of cytoskeleton to the cell morphology was usually accomplished by adjusting the elasticity or stiffness of the cell.

2.3 CELL'S TRACTION FORCE STUDY

Advances in imaging technology allowed measurement of cell shape, migration velocity, and traction forces at high spatial and temporal resolution [77]. Specific candidate proteins were visualized by expressing fluorescent fusion proteins that often caused minimal or no disruption of protein function. For example, dynamic changes in actin filament structure were monitored using speckle microscopy. Many techniques and devices were developed to measure the intracellular

traction forces of cells on continuum substrate. One example used a silicone substrate such as polydimethylsiloxane (PDMS) where cells cultured on the substrate caused it to deform by applying force to the substrate and thereby produced wrinkled pattern on it. The second technique used fluorescent beads-embedded polyacrylamide gels where the cultured cells generated traction forces that deformed the gel structure. The deformations were detected by the movement of the embedded beads. These techniques led to a significant improvement in our understanding of spatial and temporal traction response in cells. However, these techniques could not determine the location and direction of point forces, and the magnitude of the force was difficult to calculate [10, 34, 78-81].

These limitations were overcome by use of high density elastomeric micropost force sensor array that allowed questions concerning cell force transmission to its environment to be experimentally investigated [35, 46, 82-86]. Using the micropost technique, cells were attached and spread across the top of the regularly ordered microposts. Since each micropost is discrete, it detects the cell traction forces independently at the site where it contacts cell. Analysis required only a spring constant of micropost and a measured deflection from acquired images. This technique appeared to be among the most effective at the sub-cellular level. Micropost array technologies were used to analyze cells such as cardiac fibroblasts or myocytes, smooth muscle cells, and cell monolayer with significantly large contractile forces at the edge of the cell and cell such as tendon fibroblast [87] with weaker contractile force.

Two factors determine the accuracy and sensitivity of the micropost force sensor array. One is the estimation of Young's modulus of PDMS micropost and the other is the height to

diameter aspect ratio. Although several techniques have been used to calibrate the Young's modulus (E) of PDMS micropost in order to determine its spring constant [88, 89], their estimation of Young's modulus were not as good as expected. PDMS micropost with low aspect ratio is limited to the use of measuring large traction force. It has been impossible to use such microposts to measure small force as low as several Nano Newton or transient behavior of the cell.

In this project, high aspect ratio (up to 13) PDMS micropost arrays were developed. The Young's modulus and spring constant of these microposts were experimentally determined by calibrating them with atomic force microscope (AFM), and the fabricated arrays were used to measure and to map the cell traction forces of VSMCs. The steady and transient responses of the VSMC in normal conditions were studied. In a long time observation (steady response) of VSMC growing on micropost array with different spring constant, it was found that VSMC's tries to adapt to its physical environment since it tended to generate larger traction force when it attached to stiffer micropost. Several constant vibration periods were found from the VSMC's transient response when it grown on the PDMS micropost array with the micropost geometry of 5 μm wide and 25 μm high. This novel MEMS micropost array led to a new insight in the cellular mechanism of sensing and responding to mechanical forces in VSMC, and which will eventually be applied into the development of new therapies for blood pressure related diseases such as hypertension and atherosclerosis.

We have studied the vascular smooth muscle cell's mechanical behavior using the following set of experiments:

1. The traction force distribution of a single vascular smooth cell in normal conditions was studied. The principle of elasticity analysis was to grow vascular smooth muscle cell on top of the PDMS micropost array. The free ends of the microposts were pulled by the cells' surface. The deflections of the microposts represented the traction forces generated by the cell and applied to them. The calculated traction forces were proportional to the elasticity of the cell. Multi-locations of a single cell were measured at the same time using high density micropost array. Thus, the elasticity distribution of a single vascular smooth muscle cell growing on PDMS micropost array was obtained.

2. The response of the VSMC to a change in substrate elasticity due to modification of the stiffness of its physical environment was studied. The PDMS micropost arrays were prepared with different stiffness. The excellent elasticity of PDMS made it possible to change the Young's modulus of the material. The adjustment of the PDMS Young's modulus was accomplished by changing the base and curing agent ratio, curing temperature, and micropost dimensions. Furthermore, the spring constant was tuned by changing the micropost's dimensions.

3. The function of ILK was studied using PDMS micropost array. In this study, two types of vascular smooth muscle cells were used. The first is named CK₄ cell (control cell with ILK), the second is named ILK cell which were made by RNAi silencing with an ILK-shRNA construct. The transient response of CK₄ cell and ILK cell to the stimulus of Angiotensin II (ANGII) and Cytochalasin-D (CYTO) were monitored. The responses of two cell types were converted from the deflection changes of the corresponding microposts. By comparing the different reactions of

control group and the target group to the stimulus, the function of ILK to the cell's proliferation were determined.

4. The PDMS micropost arrays were fabricated with high aspect ratio to enable real-time monitoring of VSMC and investigation of elasticity and investigating the mechanical dynamics of VSMC's focal adhesions located on the top of individual micropost. The high aspect ratio PDMS micropost enabled the detection of very small forces and therefore enabled quantification of the interaction between microposts and the multi-location in a single cell. The oscillation of smooth muscle cell were found using PDMS micropost array. The purpose of the experiment was to obtain insight into the dynamic of cell mechanics and its underlying cytoskeletal mechanisms. The micropost array allows us to follow the dynamics of cell's elasticity and corresponding dynamics of the cytoskeleton activity under various conditions at multiple points with the cell.

3. PDMS MICROPOST ARRAY

This chapter will introduce and describe the design of the PDMS micropost array for traction force study of vascular smooth muscle cells (VSMC). Several design parameters of the micropost array such as micropost diameter, height and spacing will be determined and discussed. The relationship between micropost deflection and the force under different micropost geometry designs will be carefully studied using finite element analysis software (Coventorware™) prior to device fabrication. The theoretical analysis of mechanical properties of the PDMS micropost will be discussed in the end.

3.1 DESIGN OF PDMS MICROPOST ARRAY

The device is designed with array of high density 3-D microposts (100×100) made of flexible material polydimethylsiloxane (PDMS) with known physical and chemical properties. The microposts are regularly spread across the substrate with exact diameter, height and spacing. One end of the micropost is fixed on the substrate and the other is free to move. The 3-D flexible environment allows the study of the sub-cellular distribution of traction forces exerted by the cells growing on the micropost array. It is important to note that the spring constant of the micropost depends on its geometry and material used. Therefore, PDMS is used to create the micropost with appropriate mechanical properties and biocompatibility for cells to favorably grow. Initially, the microposts top surface are treated with oxygen plasma, and coated with extracellular matrix proteins (collagen or fibronectin) in order to enhance the surface properties and enable the cells to attach to them. This also promotes cell growth on micropost top surface.

Once the cells start growing, they begin to spread and exert forces on the micropost to pull or push the top of the micropost and make them bend. The post-deflections are measured using a confocal microscope and are translated into traction forces using beam bending theory.

In the linear regime, the micropost behaves similar to a spring such that the deflection is directly proportional to the force applied by the attached cells. Hence, the traction forces are quantified by determining the deflection of each micropost. A very attractive aspect of utilizing microposts array in cell study is that it is possible to make three dimensional analysis of the traction force in real time if the force measurement is combined with atomic force microscope (AFM).

3.2 STRUCTURAL AND MECHANICAL ANALYSIS

3.2.1 THEORETICAL MECHANICS

The micropost is treated as a cylindrical cantilever beam: one end is fixed to the substrate and the other end is free to move. In the linear regime, the micropost behaves similar to a spring such that the deflection of the micropost due to cell's movement (traction or expansion) is directly proportional to the force applied by the attached cells. Hence the traction forces are determined by measuring the deflection of each micropost using scanning electron microscope or confocal microscopy. The relationship between force, F , and free end displacement, x , for a cylindrical beam can be determined using the theory of cantilever beam bending (Euler-Bernoulli Beam Theory) [79, 86, 90]:

$$F = Kx = \frac{3\pi ED^4}{64L^3} x \quad (3.1)$$

where E is the Young's modulus of PDMS, D , L and x are the diameter, length, and deflection of the micropost, respectively. In the linear regime, the spring constant K is given by:

$$K = \frac{3\pi ED^4}{64L^3} \quad (3.2)$$

From equation 3.2, the spring constant of a single micropost is determined by the micropost geometry and the material properties. The exact diameter and height is obtained using scanning electron microscope (SEM), and the Young's modulus of PDMS is determined by calibrating the micropost using AFM. In this thesis, the same size microposts used in the cell experiments, are used to determine the Young's modulus (E).

3.2.2 MODELING AND SIMULATION OF PDMS MICROPOST

Finite element analysis (FEA) software Coventorware is employed to determine the micropost geometry, the deflection as a function of force applied on the top surface of the micropost, and hence provide an accurate prediction of their performance. **Figure 3.1** shows the 3-D view of a deflected micropost with mesh configuration. Since the final device is a cylindrical PDMS micropost with one end fixed at the PDMS substrate, the simulation can be conducted by modeling the mechanical behavior using a single micropost with a rigid end. In addition, the simulation of a micropost with a rectangular base (thickness and size of $500\mu\text{m}$ $250\mu\text{m}\times 250\mu\text{m}$, respectively), with comparable thickness to the fabricated device are simulated (see **Figure 3.2**). It shows relatively similar results when compared with simulation of only a rigid anchor. Both simulations use the micropost with diameter and height of $5\ \mu\text{m}$ and $25\ \mu\text{m}$, respectively. The

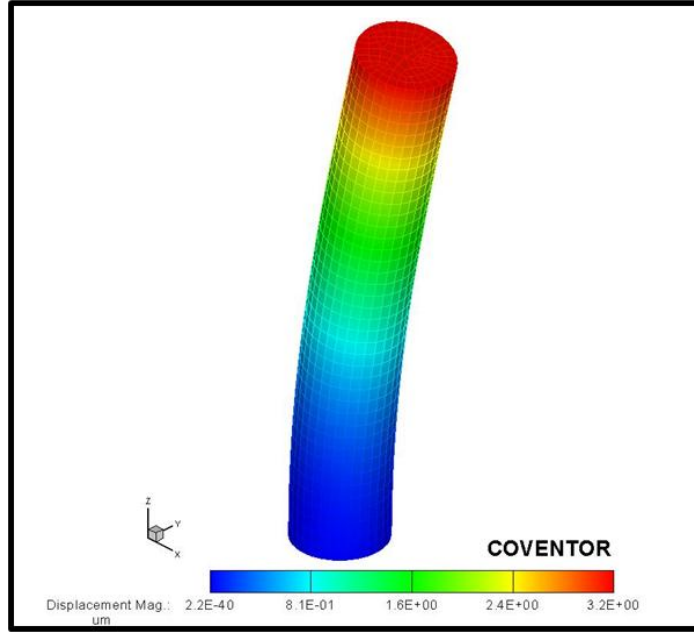


Figure 3.1. 3-D view of the micropost without PDMS base

deflection of a single micropost under a 15 nN traction force is 2.55 μm while the deflection of a single micropost with base under a 15 nN traction force is 2.58 μm . The simulation results of such two cases have 0.78% difference. One possible explanation of such relatively similar results in those two cases is that the size and the mass of the base are extensively larger than those of a single micropost. For example, the thickness of the base is more than 2 mm and the size of the base is $2 \times 2 \text{ cm}^2$ which leads to a volume at least 10^6 times larger than that of a single micropost. Although PDMS has very good elasticity (very flexible), the effect of indentation of PDMS substrate due to the deflection of the micropost is negligible during the cell experiment and the micropost is simulated as one end fixed at the substrate and the other end is free to move. Furthermore, the thin, flat PDMS substrate sticks to the bottom of Petri dish very well. The following simulation is performed using simplified such solid model without PDMS base.

The second task is to verify the validation of the simulation results. In general, the simulation error should be reduced if higher mesh density is applied to the same solid model.

The simulation error is defined by the following equation:

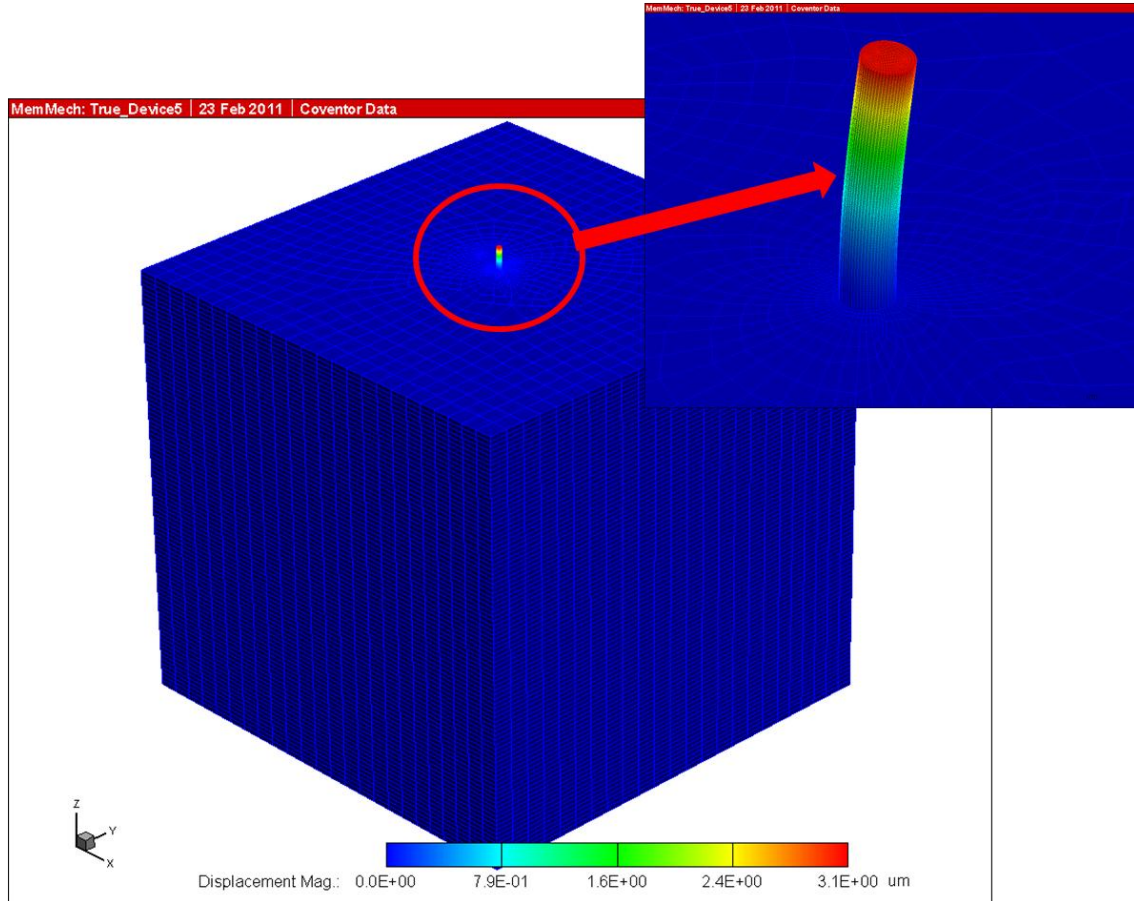


Figure 3.2. 3-D view of the micropost with PDMS base

$$Error(\%) = \frac{(FEA_{a \times b} - FEA_{45 \times 230})}{FEA_{45 \times 230}} \times 100\% \quad (3.3)$$

where $FEA_{45 \times 230}$ is the simulation result under the mesh density of 45×230 , $FEA_{a \times b}$ is the simulation result under any other mesh density. The mesh density is changed from 10×50 to 60×300 . The simulation results under these mesh density configurations are shown in

Table 3.1 Relationship between mesh configuration the simulation error

	Mesh Size	Error
1	10×50	0.02986
2	12×60	0.020543
3	16×80	0.010692
4	25×120	0.003636
5	45×230	0
6	60×300	-0.0007
7	70×360	-0.00203

Table 3.1. It should be noted that as the mesh density increased, the simulation error is decreased which indicates that the simulation results is able to converge when mesh size is reduced. However, the simulation time increased significantly when the mesh size is decreased. Therefore,

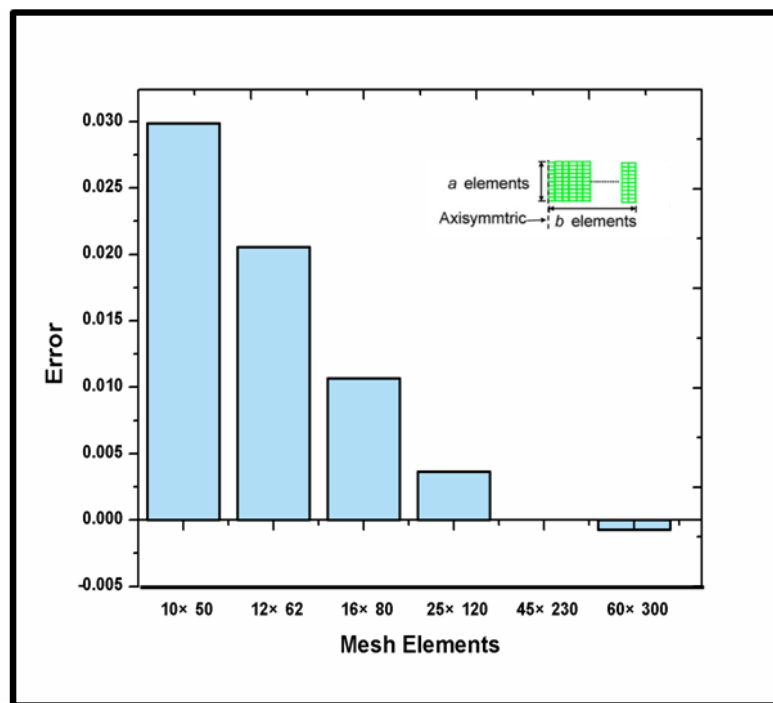


Figure 3.3. The relationship between simulation error and mesh size

there is a trade-off between simulation accuracy and consideration of simulation time. An optimized mesh configuration of 45×230 is used for all models. The convergent simulation results are also plotted in **Figure 3.3**.

3.2.3 MECHANICAL AND STRUCTURAL MODELING

Three models are studied to determine the micropost geometry that lead to a suitable

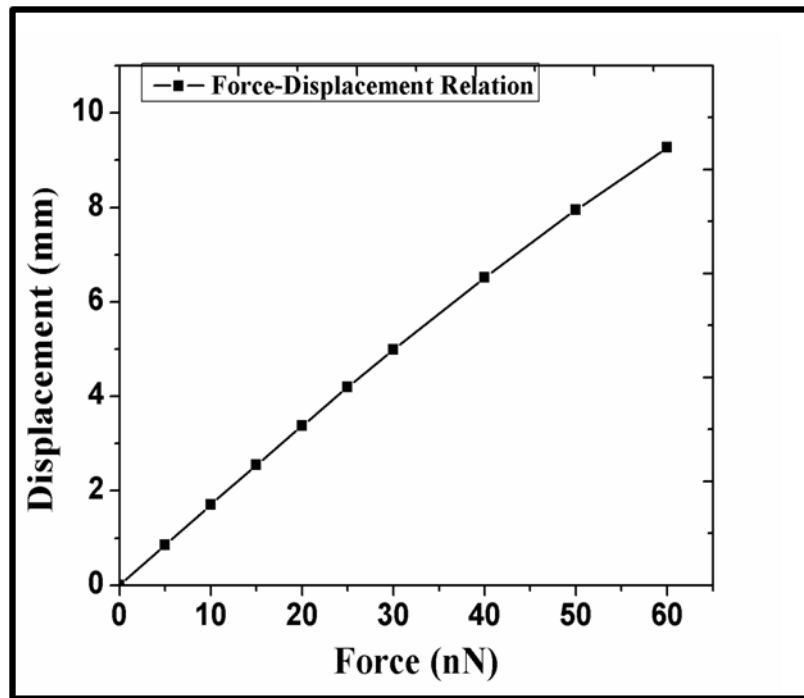


Figure 3.4. The micropost deflection and the lateral force applied on the top of the micropost (Diameter and height of the micropost is fixed at $5 \mu\text{m}$ and $25 \mu\text{m}$, respectively)

spring constant for both growing cell on their top and observing sufficient bending. Due to micropost's regular shape, the 'Manhattan Bricks' has been used as the mesh type. In the first simulation model, the force-deflection relationship is investigated. The micropost diameters and heights are fixed at $5 \mu\text{m}$ and $25 \mu\text{m}$, respectively. The Young's modulus of the PDMS is set to

1.38 MPa. The bottom of the micropost is set to ‘fix all’ and a shear force parallel to the original position of micropost top surface (XY plane) is applied to the center of micropost top surface. The magnitude of this force is changed between 0 to 60 nN which is equivalent to the force generated by VSMC found in published literature [53, 54, 62]. The deflections corresponding to different levels of traction forces are computed by Coventorware and shown in **Figure 3.4**. For example, a 15 nN force is able to cause a noticeable deflection to the micropost’s free end by 2.55 μm . It should be noted that the micropost was deflected linearly when the traction force locating between 0 - 40 nN.

In the second simulation model, the height-deflection relationship was determined. The height of the micropost is varied between 0-25 μm , and the diameter and applied force parallel to

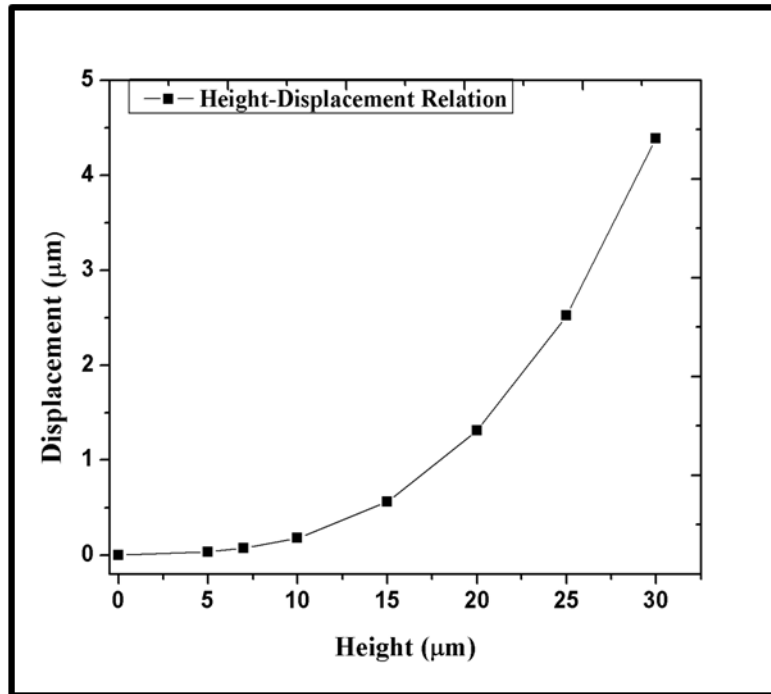


Figure 3.5. The relationship between micropost displacement and its diameter (Diameter and height of the micropost is fixed at 5 μm and 25 μm , respectively)

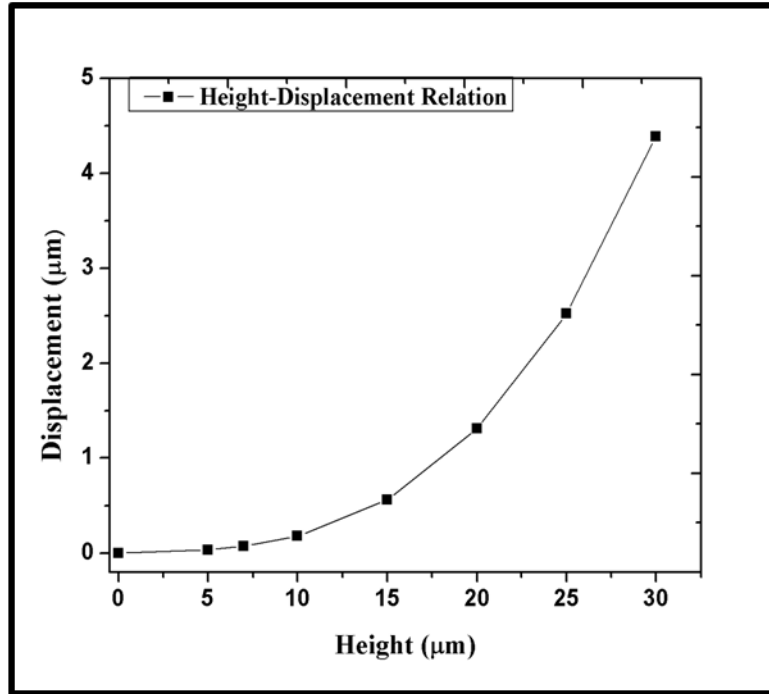


Figure 3.6. The relationship between micropost displacement and its height (Diameter and height of the micropost is fixed at 5 μm and 25 μm, respectively)

the micropost top plane are fixed to 5 μm, and 15 nN, respectively and the simulation results are shown in **Figure 3.5**. A deflection of 2.52 μm is achieved for a micropost with a height of 25 μm. It can be seen that the relationship between micropost deflection and its height is cubic. This is consistent with the theoretical property which is represented by Euler-Bernoulli Beam equation (see **Eq. 3.1**).

In the third model, diameter-deflection relationship of the micropost is determined by varying micropost diameter from 3 to 15 μm and fixing micropost height and applied force parallel to the micropost top surface to 25 μm and 15 nN, respectively. The simulation result is shown in **Figure 3.6**. It can be seen that the relationship between micropost deflection and its height is a power of four. This is also consistent with the theoretical property which is

represented by Euler-Bernoulli Beam equation (see **Eq. 3.1**). It should also be noted that the micropost diameter has more effects on changing/tuning the spring constant than the micropost height does. Based on the simulation results, a mask is designed and fabricated with the following dimensions: the micropost diameters are 3, 5, 7 and 10 μm , the edge to edge spacing was 5, 7 and 10 μm . The proposed height of the fabricated PDMS micropost is ranged from 15 to 30 μm .

3.3 CONCLUSION

In this chapter, the mechanical properties of cylindrical PDMS micropost are studied by finite element analysis software Coventorware. The solid model is simplified to a cylindrical micropost without PDMS base. The validations of this simplifying assumption as well as the simulation methodology are proved. The simulation error is effectively reduced by shrinking the mesh size.

At the meantime, the appropriate mesh size (mesh density) is chosen to obtain accurate simulation results. The simulation results show that the spring constant of the micropost decreased when the height of the micropost is increased or the diameter of the micropost is decreased. This conclusion is consistent with the Euler-Bernoulli Beam equation. The proposed micropost geometry is determined based on the simulation results.

4. FABRICATION AND CALIBRATION OF PDMS MICROPOST

The PDMS micropost force sensor arrays are fabricated using standard photolithography, etching and replica-molding techniques. The fabrication of high aspect ratio (up to 13) PDMS microposts will be discussed. In addition, the successful measurements of accurate Young's modulus of the PDMS micropost will be described in details and will be compared to other published works.

In this chapter, the process of fabricating high quality micropost arrays with different geometries will be described in detail. The optimization of each fabrication step will also be discussed. The fabrication is simplified to reduce the fabrication time. The microposts with the same geometry as those used in biology experiment are calibrated using atomic force microscope. The statistical analysis is used to determine the accurate Young's modulus of PDMS micropost. More importantly, the factors which closely related to determine the Young's modulus of PDMS are extracted during the fabrication and calibration. This step is very critical to adjust the mechanical property of PDMS micropost during the fabrication which gives the device great flexibility to tune its spring constant for different biological applications.

4.1 FABRICATION OF HIGH ASPECT RATIO PDMS MICROPOST ARRAY

The micropost arrays are fabricated using standard photolithography and replica-molding techniques in the following sequence: 1) the 4'' silicon wafers are thoroughly cleaned using pirhana solution, 2) a photoresist layer (Shipley 1813 and 1827) is patterned on the wafer

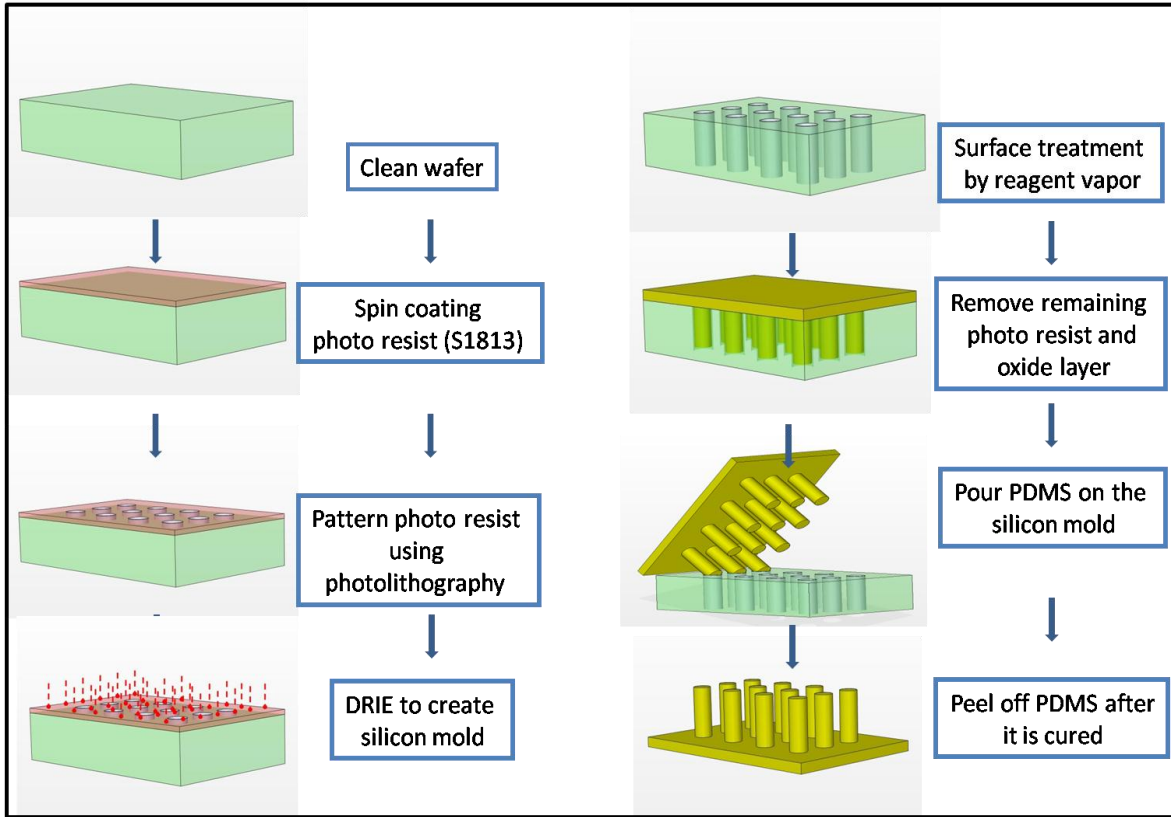


Figure 4.1. Procedures of fabricating PDMS micropost array

(**Figure 4.1**) to form openings at location corresponding to the microposts. Silicon micromold is formed by etching micro-holes with high aspect ratio using a Deep Reactive Ion Etching System (Alcatel DRIE AMS-100) and Bosch process (See **Figure 4.1**); 3) the remaining photoresist is removed from wafer. Then the wafer is cleaned again with pirhana solution and the natural oxide layer is removed using hydrofluoric acid (HF); 4) the wafer is diced into 2cm×2cm square which contains 4 arrays and is placed in a petri dish; and PDMS, prepared by mixing the resin (Sylgard 184 Silicon Elastomer Kit, Dow Corning) with curing agent (10:1), is poured on the micromold. The PDMS-wafer mold is placed inside a vacuum oven at 65°C for 24 hours (**Figure 4.1**). 5) After the PDMS is cured, it is peeled off manually creating the micropost arrays. Each of the

peeled off samples is cut into 4 arrays and they are ready for cell culturing experiment. The microposts are fabricated with diameter, height and spacing ranged between 3-10 μm , 5-70 μm , and 5-10 μm , respectively. The following sections will provide detailed description of the fabrication processes.

4.1.1 PHOTORESIST PATTERNING

A positive photoresist with a thickness of 1.1 μm and 3.5 μm (Shipley 1813 or 1827) is used as a mask for etching silicon. The thin photoresist is used when etching depth is less than 10 μm . Thick photoresist Shipley 1827 is used when etching depth is larger than 10 μm . The photoresist is patterned to arrays of open round holes with diameter ranging from 3 μm to 10 μm . Initially, the photoresist is spin coated on the silicon wafer and soft baked on a hotplate at 90°C for 2 minutes. The photoresist is pattern with photolithography. The wafer is then hard baked on the hot plate for another 1 minute at 95°C in order to remove the remaining solvent and harden the photoresist for the deep reactive ion etching. It is important to note that for a hole with diameter of 3 μm or less, an oven is used for soft baking at 95°C for 15 minutes and for hard baking at 95°C for 20 minutes. The use of oven instead of hot plate is crucial to eliminate the photoresist cracks caused using hot plate. In this case, the yield is improved from 75% to 99%.

4.1.2 DEEP REACTIVE ION ETCHING (DRIE)

The silicon mold is prepared by etching deep holes using deep reactive ion etching system. The deep reactive-ion etching (DRIE) enables a highly anisotropic etching process used to create deep holes with vertical side walls and with aspect ratio of 30:1 or more. DRIE is based

on a combination of chemical and physical etching which allows anisotropic (uni-directional) material removal [91]. The etching process is carried out in chemically reactive plasma containing positively and negatively charged ions generated from the gas that is pumped into the

Table 4.1 Comparison of Bosch and Cryo processes

Parameters	Bosch process	Cryo process
Sidewall protection	Fluorocarbon polymer	SiO _x F _y
Sidewall roughness	Noticeable near wafer surface	Smooth
Protection cycle	Yes	No
Mask selectivity	75:1 for resist 200: 1 for oxide	>100:1 for resist up to 1000:1 for oxide
Resist	Soft bake only. Not sensitive to t	Not thicker than 1.5µm or age of resist
Special requirement	Fast pumping Low flow oxygen : Fast mass flow controllers	Cryogenically cooled stage Heated chamber and pump line Short mixed gas line

reaction chamber and accelerated and ionized by electrons. A mask on top of the substrate is used to protect certain areas from etching, exposing only the areas to be etched. The ions are accelerated into the etching region, where they attack the substrate surface and react with it. DRIE primarily employs ion-assisted processes, where a heavy ion bombardment break the chemical bonds and the radicals chemically react with exposed surface atoms and produces a volatile byproduct. The DRIE has unique advantages such as high aspect ratio, extremely large etching depth and very high etching rate (4-20 µm/min). The DRIE operation uses Cryo or Bosch processes. Both are able to deep etch silicon with high aspect ratio. Cryo is a single step process done at cryogenic temperatures (less than -100 °C) while Bosch is a cycling two-step

process altering between depositions and etching steps performed at 10-20 °C. Although the Bosch process is more popular, each of them has its own advantages depending on the product's process requirements. **Table 4.1** shows the different features of cryo process and botch process. The most significant feature of cryo process is that it does not have independent sidewall

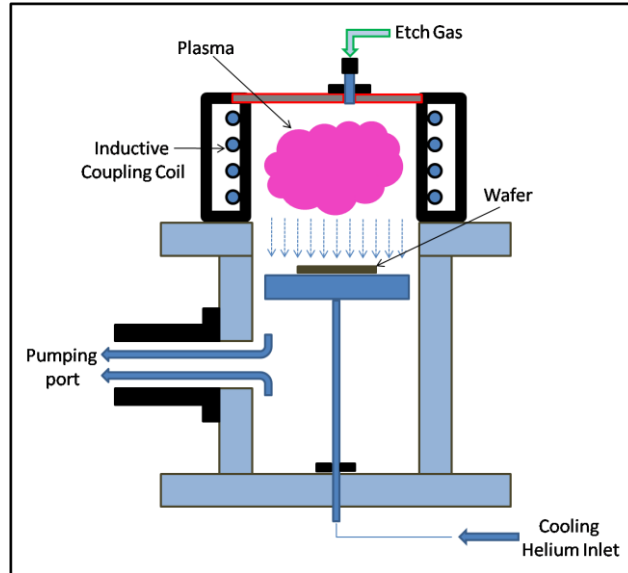


Figure 4.2. Schematic of DRIE system

protection cycle and its mask selectivity is much higher than Bosch process. On the other hand, Bosch process has independent sidewall protection cycle which makes the overall process much easier to be controlled. In this project, the Bosch process using Alcatel AMS 100 Deep Reactive Ion Etch System is used to create high aspect ratio micromold.

4.1.3 DRIE PROCESS AND HIGH ASPECT RATIO SILICON MICROMOLD

The Bosch process, also known as pulsed or time-multiplexed etching alternates repeatedly between two modes (etching and deposition) to achieve nearly vertical structures. The

first step is a standard, nearly isotropic etching. In this case, the plasma contains some ions, which are accelerated by the strong electro-magnetic field and attack the wafer from a nearly vertical direction (For silicon, this often uses sulfur hexafluoride [SF_6]). The second step is the deposition of a chemically inert passivation layer. C_4F_8 source gas is used to yield a polymer similar to Teflon which will attach to the sidewall as well as the bottom of the etched silicon. Each phase lasts for several seconds. The passivation layer protects the side walls from further chemical attack and prevents further etching. During the etching phase, the directional ions that bombard the substrate attack the passivation layer at the bottom of the trench and sputter it off and hence exposing the substrate to the chemical etchant.

These etch/deposit steps are repeated many times resulting in a large number of very small isotropic etch steps taking place only at the bottom of the etched holes. To etch through a

Table 4.2. The condition of bosch process

Parameters	Conditions
SF ₆ Flow Rate	700SCCM
C ₄ F ₈ Flow Rate	180SCCM
O ₂ Flow Rate	0 SCCM
Etching Cycle	7.5 Seconds
Deposition Cycle	2 Seconds
Source Power	1800W
Substrate Holder Power	80W

0.5 mm silicon wafer, for example, 400 etch/deposit steps are needed. In order to create several microns wide and several tens of microns deep micromold array, the cycle time, flow rate, etching temperature and forward power needs to be optimized.

The Bosch process recipe to fabricate the micropost array mold is shown in **Table 4.2**. The etching of silicon by SF_6 lasts 7.5 seconds per cycle and the polymer deposition by C_4F_8 lasts 2 seconds per cycle. Before etching process starts, the main chamber is evacuated to the basic pressure which is lower than 3.0×10^{-6} mbar. The processing stage which holds the silicon wafer is cooled by the helium gas. The processing temperature on the silicon wafer is 20°C . The etching rate is $1.2 \mu\text{m}$ per cycle. The distance between the plasma source and the wafer stage is

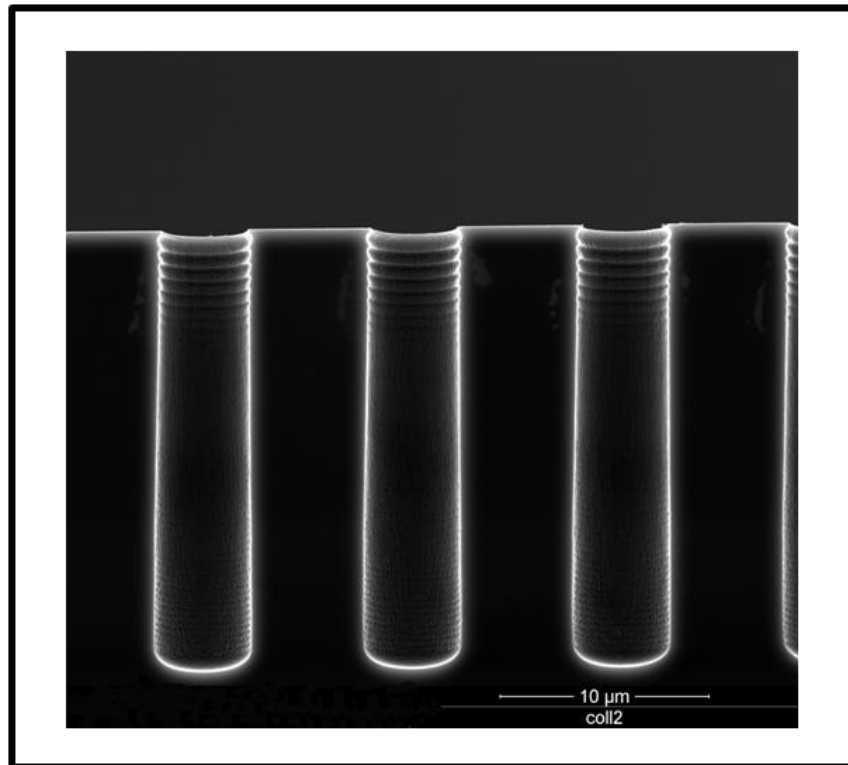


Figure 4.3. Profile of micromold after DRIE process

set to 199 mm. **Figure 4.3** shows the micrograph of the cross section view of the etched silicon wafer using scanning electron microscope (SEM). The micromold in **Figure 4.3** is 5 μm wide and 25 μm deep. The undulate profile on the side wall can be easily seen. The sidewall is very sharp and straight which means the anisotropic etching is realized by using the optimized etching recipe. **Figure 4.4** shows the micrograph of micromolds with two sizes on the same wafer. The micromold on the left has a diameter of 5 μm and the one the right has a diameter of 3 μm .

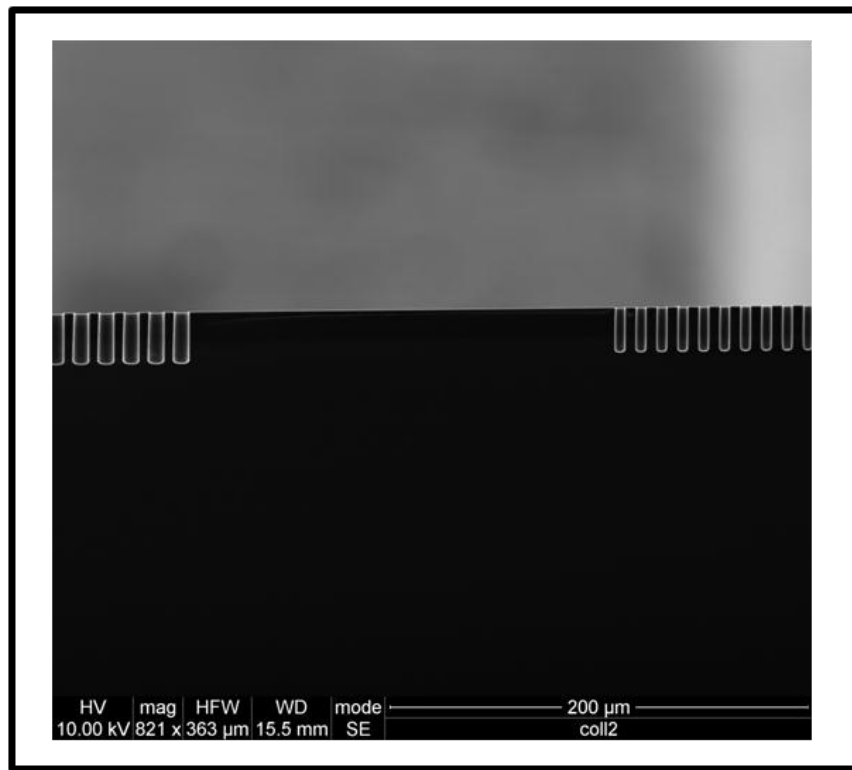


Figure 4.4. Profile of micromolds with different size after DRIE process

4.1.4 PDMS PREPARATION AND MICROMOLD SURFACE TREATMENT

The wafer is then diced to $2 \times 2 \text{ cm}^2$ piece and each contains four arrays of microholes with different diameter and spacing. The diced micromold is then put into a 35 mm culture dish.

A certain amount of resin (Sylgard 184 Silicon Elastomer Kit, Dow Corning) mixed with curing agent is prepared with 10:1 ratio by electronic scale. They are mixed very well by manually stirring. The mixture is then poured on top of the micromold. The mixture amount is determined by the substrate thickness. In this case, the thickness of the PDMS substrate is limited to less than 1mm due to the limited focus depth of the confocal microscope

The petri dish is then put into a vacuum oven to de-gas for 10 minute at room temperature. The evacuation is performed in room temperature to slow down the curing speed. This step is very important to make clean and transparent device without air bubble. Then, the

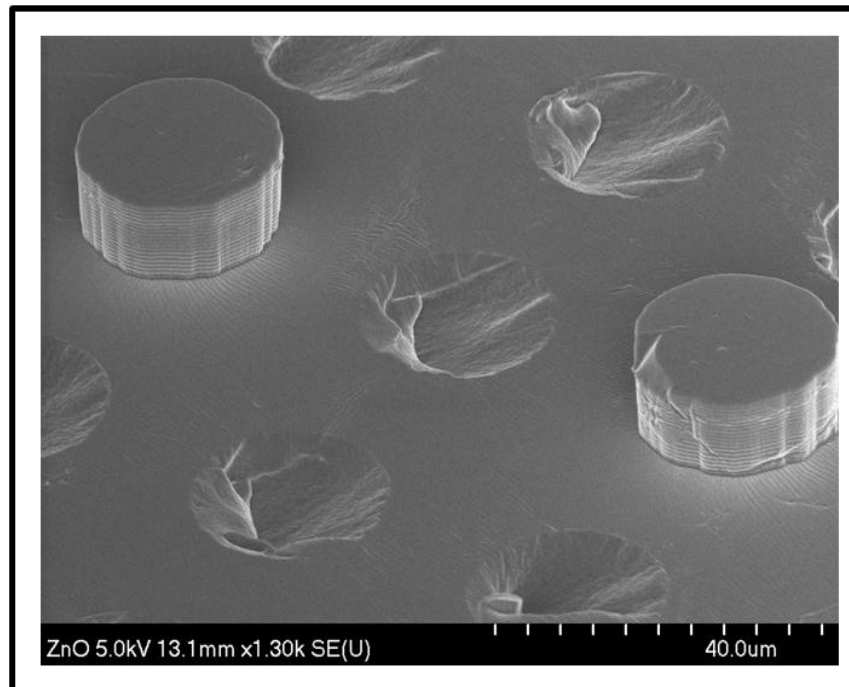


Figure 4.5. Initial fabricated micropost array with most of the posts stuck in the micromold

PDMS mixture is curing in oven for 24 hours at 65°C. Finally, the PDMS micropost array is peeled off carefully from the silicon micromold to complete the device fabrication.

The quality of initial fabricated micropost array is bad (see **Figure 4.5**). Most of the microposts are not intact after peeled off the micropost and they are stuck inside the mold. The first possible reason for the posts to stick inside the micropost could be the roughness of the sidewalls of the etched silicon micromold. As mentioned before, the Bosch process contains etching cycle and deposition cycle which makes undulated patterns on the side wall of the micromold. When PDMS cured and peeled off from such micromold, the undulated surface increases the friction between the sidewall and the PDMS significantly. Such large friction will break the micropost when moving which will cause most of the cured microposts to stick inside the mold. One solution can be achieved by modifying the deep reactive ion etching recipe to create smoother sidewalls. Therefore, the optimization of the process recipe will help smooth the side walls of the micromold.

The second possible reason for the microposts to stick inside the micropost is the large surface tension between PDMS and the silicon micromold. The PDMS mixture before curing has hydrophilic property which will cause it to stick very well to the silicon micromold surface. During the PDMS curing process, large amounts of reactive hydroxygroups (-OH) acts as bonding agent which makes the PDMS attaches to the silicon surroundings very well. Such firm attachment will block the cured microposts from peeling off the mold. The possible solution for such problem is: Deposit a very thin layer of nonadhesive material on the micromold before pouring the PDMS mixture on it or treat the micromold surface with some chemical which reacts with hydroxygroups (-OH) before they react with silicon. Such process makes the uncured PDMS 'unsticky' to the micromold sidewall. In this project, we have explored and used special chemical vapor to treat the micromold in order to ease the peel of the PDMS from the micromold.

The special chemical has two important features: It is volatile, and it is reactive to hydroxygroups (-OH) effectively. Hexamethyldisilazane is an ideal candidate for such process. A small amount of hexamethyldisilazane is used during the fabrication process. Several droplets of hexamethyldisilazane are placed in the petri-dish which was put in the vacuum desiccators. The micromolds are then put into the same desiccators and the evaporated hexamethyldisilazane is coated on the surface of the silicon micromold. PDMS mixture is then poured on top of silicon mold and cured for 2 hours. The following processes are exactly the same as described before. The quality of the final device is improved significantly. The micropost's yield in a single array is increased from less than 5% to 95%-100%. **Figure 4.6** shows two micrographs of one fabricated high quality PDMS microposts with diameter and height of 3 μm and 25 μm , respectively, using scanning electron microscope.

The high quality PDMS micropost arrays with different diameters and heights are successfully fabricated using the optimized processing steps. The height to diameter aspect ratio is from 0.7 to 13. The most flexible micropost has a diameter and a height of 3 μm and 38 μm , respectively. **Figure 4.7** shows the micrograph of micropost with diameter and height of 7 μm and 5 μm , respectively, and diameter and height of 3 μm and 30 μm , respectively. **Figure 4.8** shows top view micrograph of such two micropost arrays. It should be noted that the microposts has good circular shape and the spacing between them are regular. It demonstrates that the fabricated micropost arrays have very high quality and even the micropost with highest aspect ratio can stand vertically without any shape or position change.

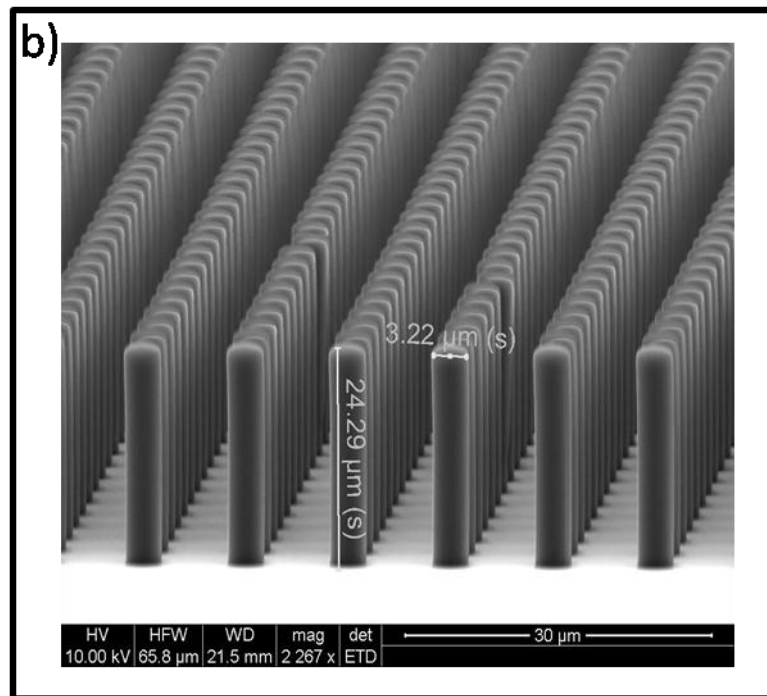
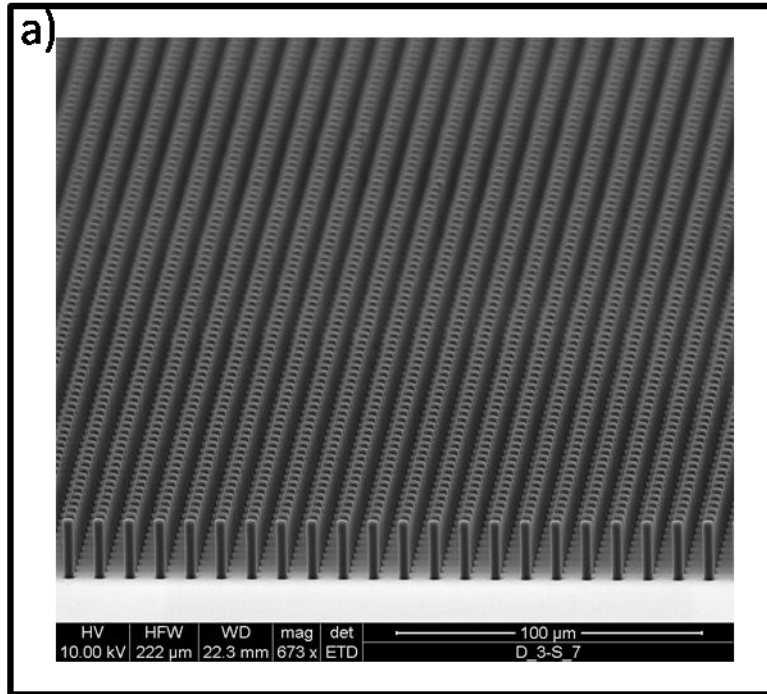


Figure 4.6. SEM micrograph of PDMS micropost array with 7 μm of diameter and 25 μm of height
 a) over view of the array and b) micropost in details

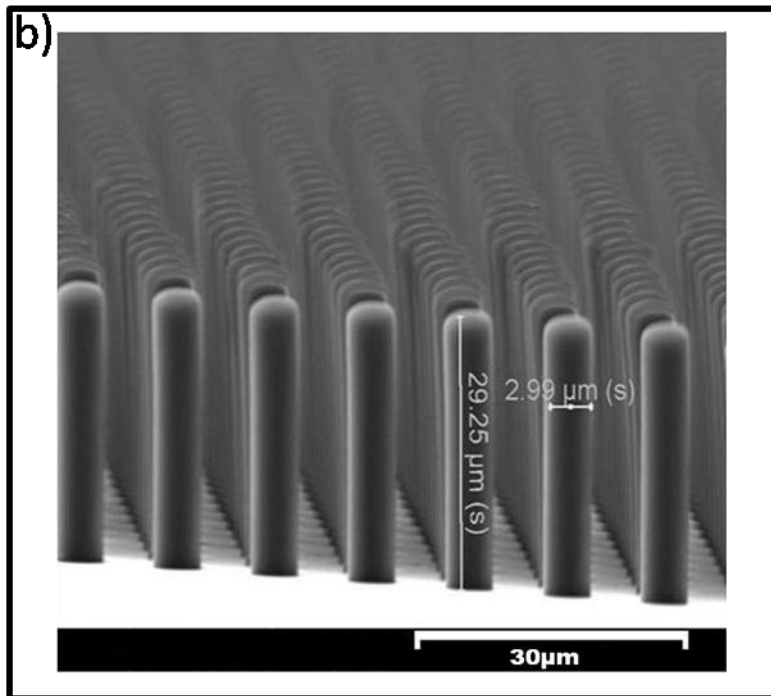
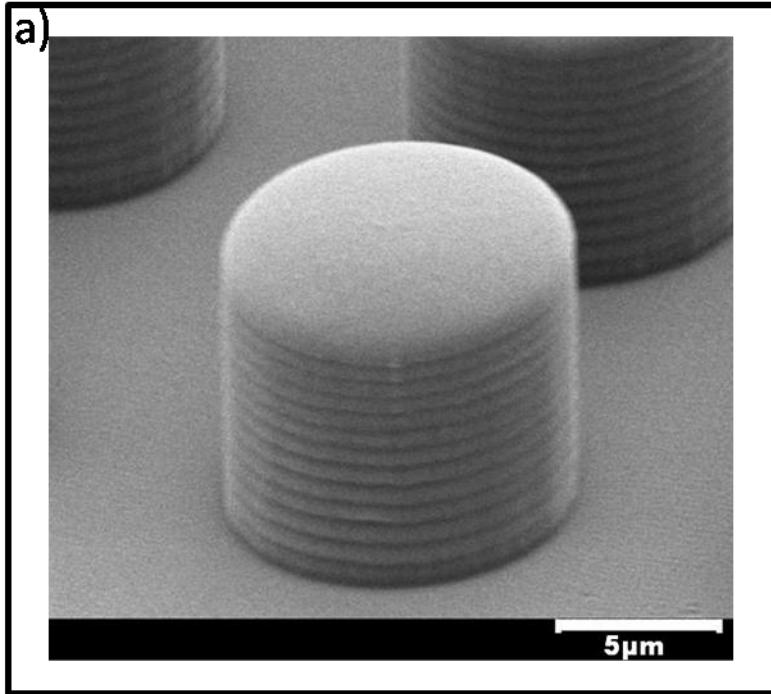


Figure 4.7. SEM micrograph of PDMS micropost array with a) 7 μm of diameter, 5 μm of height and 7 μm spacing; b) 3 μm of diameter 30 μm of height and 5 μm of spacing

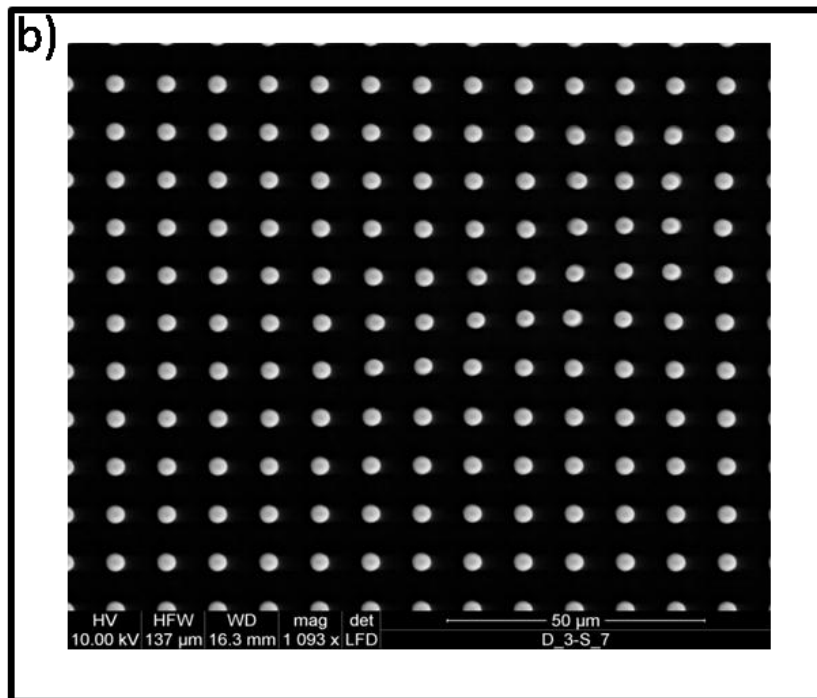
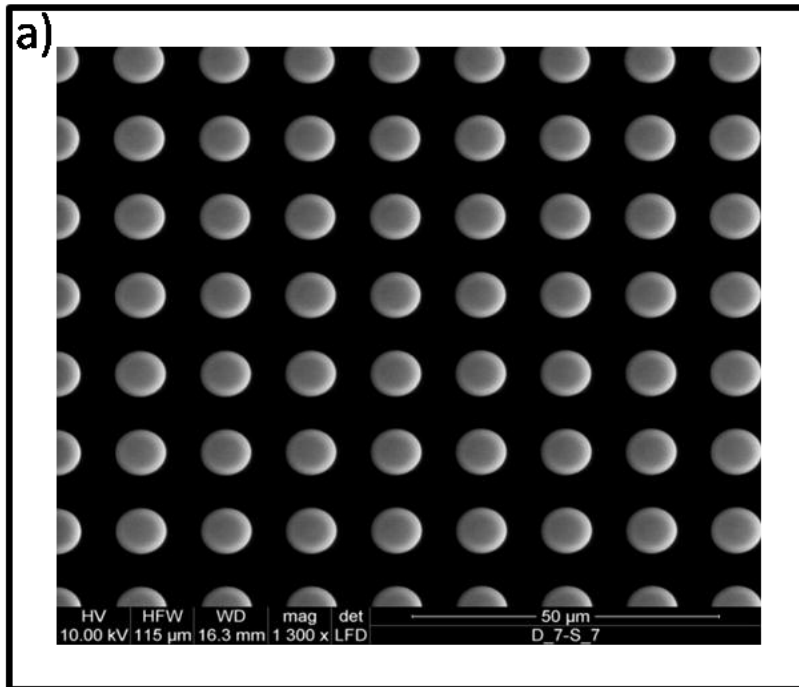


Figure 4.8. SEM top view of PDMS micropost array with a) 7 μm of diameter, and 7 μm spacing; b) 3 μm of diameter 10 μm of spacing

4.2 CALIBRATION OF PDMS MICROPOST

The estimation of the traction force at each micropost requires the accurate measurements of its spring constant and deflection. Microposts are made using polydimethylsiloxane (PDMS), because it is bio-compatible and its mechanical properties can be tuned in physiologically relevant ranges. The Young's modulus (E) of PDMS microposts depends on the curing temperature, the mixing ratio of silicone base to the curing agent, and the mixing of PDMS curing agent with solvent such as Hexane [92]. The previously reported Young's modulus ranges from 0.3 to 3 MPa [93-96] where E was determined by several techniques: One group determined it by using large dimension micropost with a diameter and height of 500 μm and 3.75 mm, respectively. They then used these values to calculate the traction forces of cells cultured on top of a small dimension micropost array [79]. A second group calibrated a glass micropipette by measuring the weight of small crystal of p-nitrophenol and then used it to calibrate micropost via piezoelectric manipulator [94]. These microposts were fabricated with relatively low aspect ratio up to 4 [92-95]. This might be due to fabrication difficulty. Some other research [88] using PDMS micropost array as force sensor did not do device calibration but use the Young's modulus from reported literature [93-95]. In general, the current calibration approaches for the PDMS micropost is not accurate enough to measure force in nano Newton or even pico Newton level.

In this work, we have calibrated the PDMS micropost using the atomic force microscope. The microposts with similar sizes to the calibrated ones are used in the biological study. The accuracy of the calibration has been significantly improved due to the high sensitivity of AFM

experiment. At the meantime, the factors which have strong impact on controlling the Young's modulus of the PDMS micropost have been carefully studied using statistical methods.

4.2.1 ATOMIC MICROSCOPE (AFM)

Atomic force microscopy (AFM) is a very high-resolution type of scanning probe microscopy, with demonstrated resolution on the order of fractions of a nanometer, more than 1000 times better than the optical diffraction limit. By using known spring constant microcantilever beam, AFM can accurately apply force in nN to pN range.

The AFM consists of a cantilever with a sharp tip (probe) at its end that is used to scan the specimen surface. The cantilever is typically silicon or silicon nitride with a tip radius of curvature on the order of nanometers. Along with force, additional quantities may simultaneously be measured through the use of specialized types of probe. Typically, the deflection is measured using a laser spot reflected from the top surface of the cantilever into an array of photodiodes. The AFM cantilever is connected to the base which is controlled by the piezoresistive controller. The base is able to move along 3 dimensions with very high accuracy. Since the applied force and the displacement can be accurately measured by the AFM experiment, the Young's modulus of the PDMS micropost can be obtained easily.

4.2.2 CALIBRATION EXPERIMENT

A. PREPARATION OF SAMPLE FOR CALIBRATION

Prior to performing the calibration, a single linear array of microposts is cut from the in X direction) to cut through (towards Y direction) micropost array from post's top to the substrate

bottom. The cuts are repeatable with specific interval in Z direction. The interval is programmable so a reproducible row of microposts is cut from the array and used as the sample for the following calibration. The use of single linear array of microposts facilitated locating and

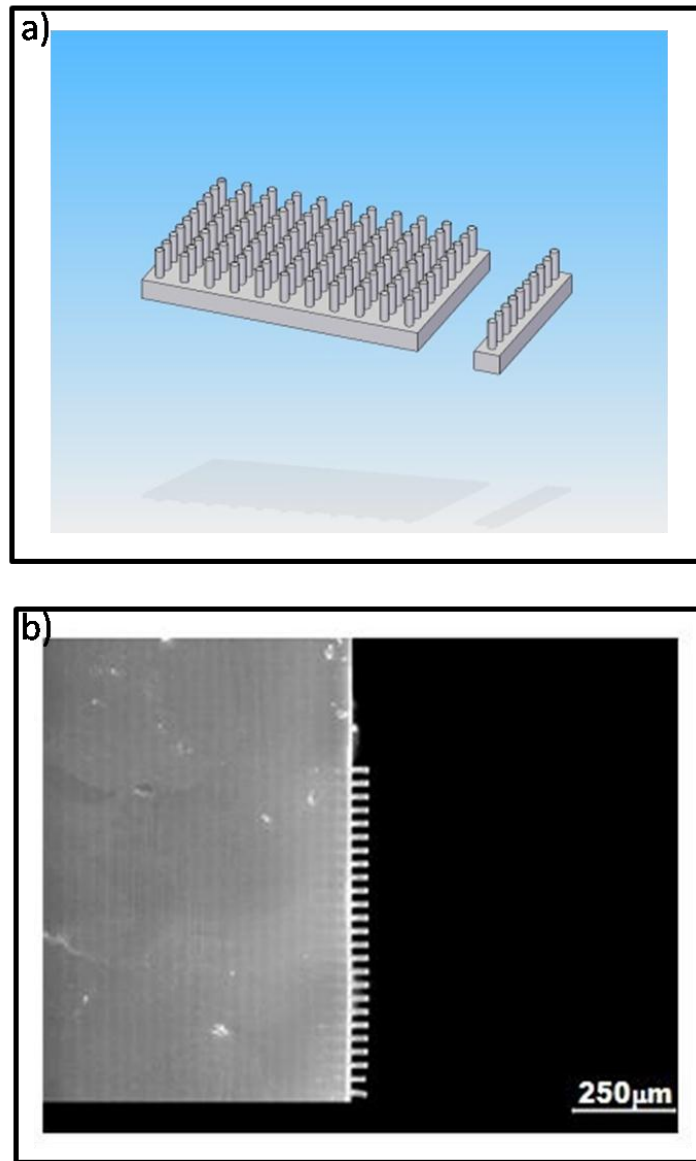


Figure 4.9. a) A row of microposts is cut from a micropost array for calibration; b) the SEM micrograph of a row of micropost with PDMS substrate

viewing single micropost, and preventing nearby microposts from touching it during calibration as shown in **Figure 4.9a**. The exact interval is determined by the spacing between the micrograph of the real sample is shown in **Figure 4.9b**. This preparation will result in more accurate measurement of force-displacement.

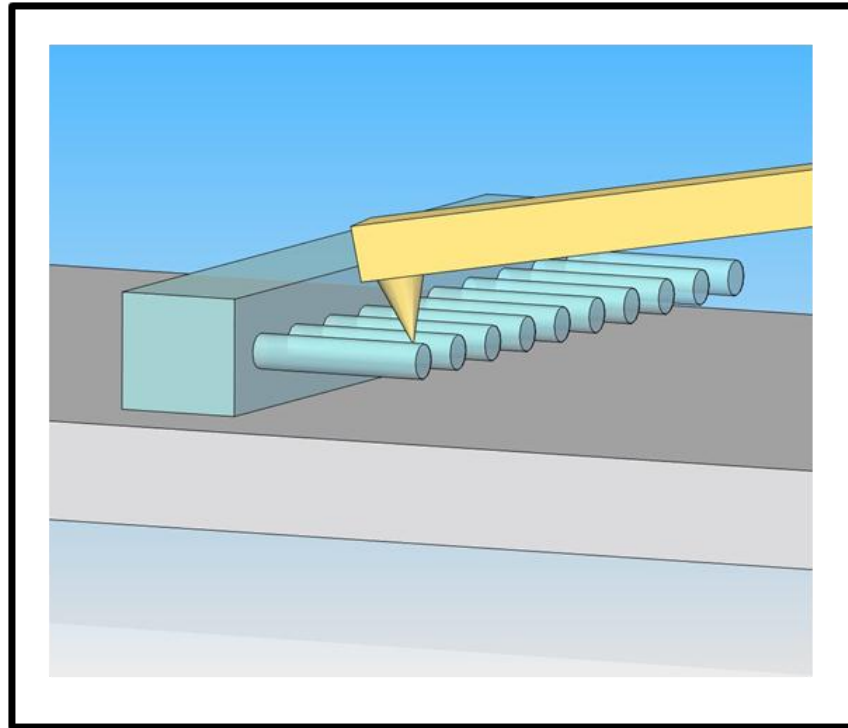


Figure 4.10. AFM tip touches the micropost free end during the calibration

B. CALIBRATION SYSTEM SETUP

The single linear array is placed on the testing stage horizontally. The AFM cantilever touches the free end of the micropost and applies a known value force (See **Figure 4.10**). To ease the analysis, we assumed that the microposts have uniform material properties such that the

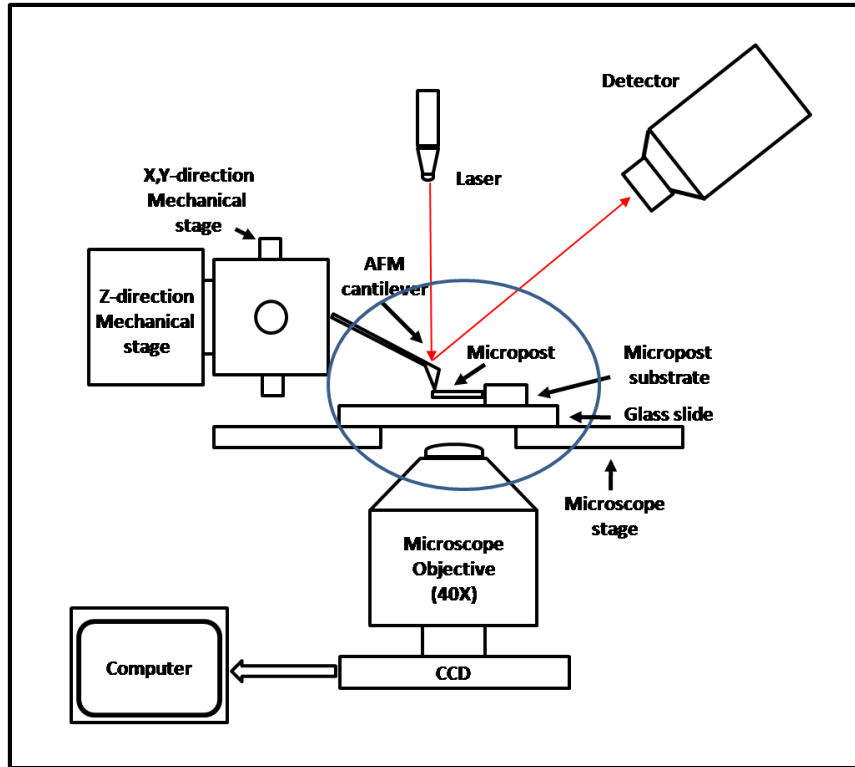


Figure 4.11. Calibration system setup schematic

deflection is equivalent to the corresponding traction force divided by the spring constant. **Figure 4.11** shows the schematic of the calibration system setup. The calibrated sample is fixed on a glass slide. The AFM cantilever tip is connected to the base which can move in x, y and z direction accurately. It touches the free end of the PDMS micropost and applies a small amount of force to the test object. A laser beam is focused on the back of the cantilever top which is coated by a gold layer. The reflected laser beam is captured by the photodetector. The deflection of the AFM tip changes the position where the laser beam is received by the photodetector. Therefore, the deflection of the AFM can be obtained. The experiment is observed using optical microscope and recorded in real time.

C. LOCATING MICROPOST FREE END WITH AFM TIP

The first step in calibrating the microposts is to place the AFM tip at the micropost's end in order to obtain accurate Young's modulus of the PDMS micropost. To locate the AFM tip at the exact end of the micropost, the following steps are implemented. First, the AFM tip is intentionally made to touch a random position on the micropost surface (which is easy to accomplish). Then the displacement of the base passed in Z direction was recorded by computer automatically. After that, the base was moved by 1 μm in x direction towards the micropost's free end and we repeated the same experiment until AFM tip no longer makes contact with the micropost. Therefore, the tip continues moving in Z direction until it reaches the glass substrate.

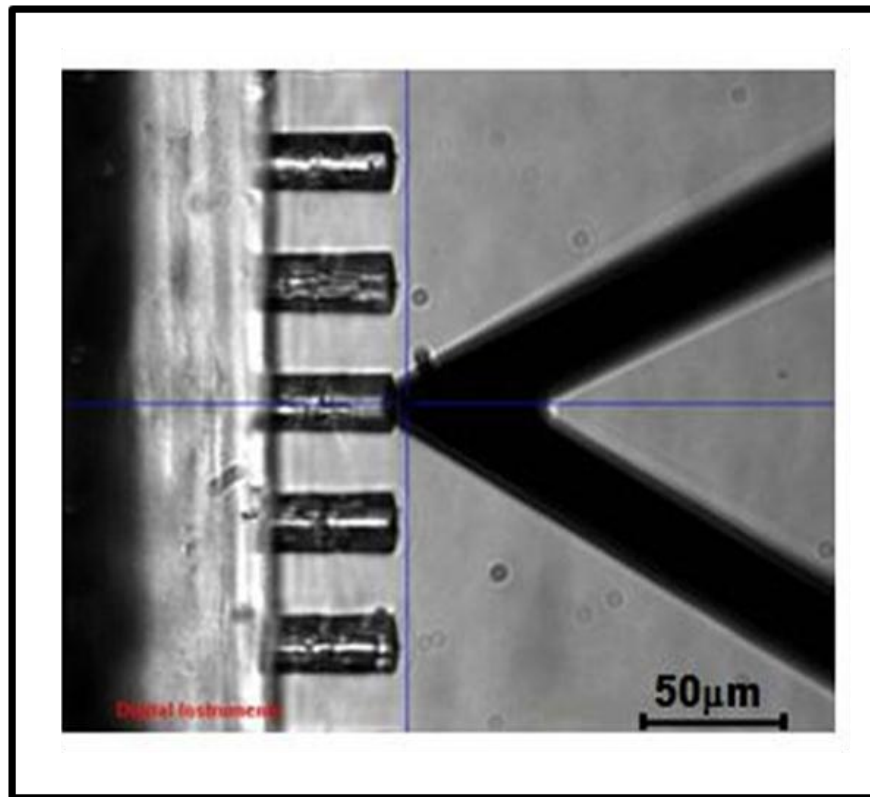


Figure 4.12. AFM tip with micropost during calibration

In this case, the Z-movement of the base will be much longer than the previous one. The offset in X direction from the previous attempt guarantees that the AFM reached the closest position to the free end of the micropost. **Figure 4.12** shows the image of AFM tip and the microposts sample captured during the calibration experiment. **Figure 4.13** shows one force-deflection relationship obtained from Matlab program which is used to process AFM calibration data. The straight line shows the linear relationship between applied forces and micropost deflection. The slope of the straight line represents the micropost spring constant and it is fixed throughout the measurement. The same experiment is repeated many times to remove the noise or system error.

D. CALIBRATION RESULTS ANALYSIS AND ITS SIGNIFICANCE

The calibration of micropost is performed as follows: First, the sensitivity of AFM cantilever beam (K_a) was measured by applying force (0-60 nN) using the AFM against a glass substrate. The deflection of the cantilever beam (d) is equal to the Z-travel of its base (z). Second, the indentation of PDMS micropost is measured by applying similar force range on PDMS substrate using AFM. The Z-travel of its base (z) includes the deflection of the cantilever beam (d) and the indentation of the PDMS micropost (σ) (**Figure 4.14a**). Third, the deflection of the micropost is determined in two steps: by applying force using AFM on its free end, and by subtracting the PDMS indentation and the deflection of AFM cantilever beam from Z-travel of the cantilever beam's base (z) (**Figure 4.14b**). The deflection is given by $x = z - d - \sigma$. After the pure deflection and the applied force of the micropost have been obtained, the Young's modulus is calculated by using the measured deflection, force and micropost geometry in the Euler-Bernoulli Beam Theory.

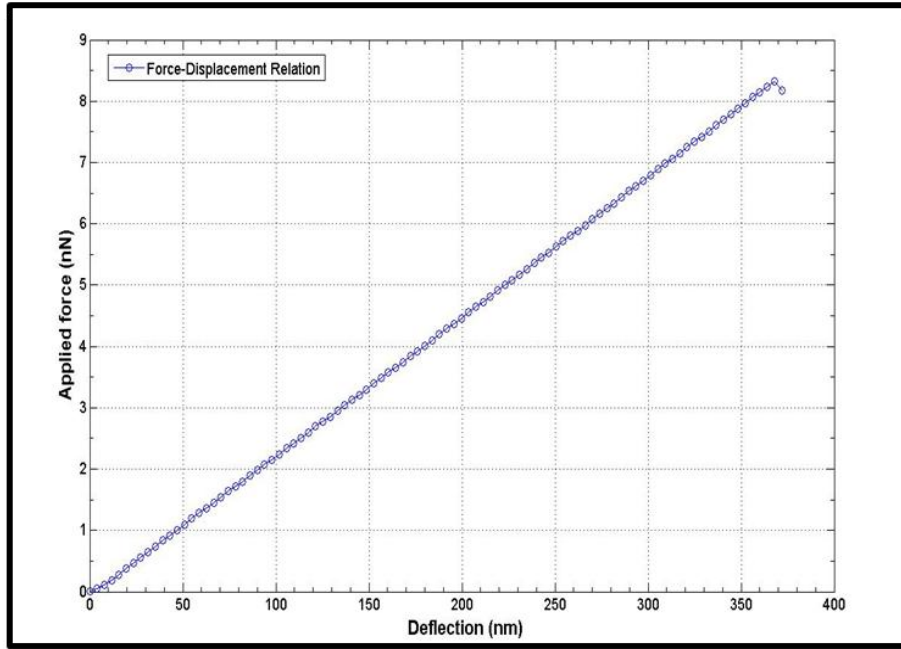


Figure 4.13. Deflection and force relation in calibration

The same calibration methods have been completed by using AFM cantilever with and without tip. The cantilever with a sharp tip is difficult to locate at the center of the micropost free

Table 4.3 Young's Modulus of large post measured with AFM Cantilever beams with a tetrahedron tip and with no tip. Both cantilevers are made of the same material.

Samples	Diameter (μm)	Height (μm)	Spring Constant (nN/nm)	Young's Modulus (KPa)
Cantilever with tip	13	33.5	0.128	1150
Cantilever without tip	13	33.5	0.131	1170

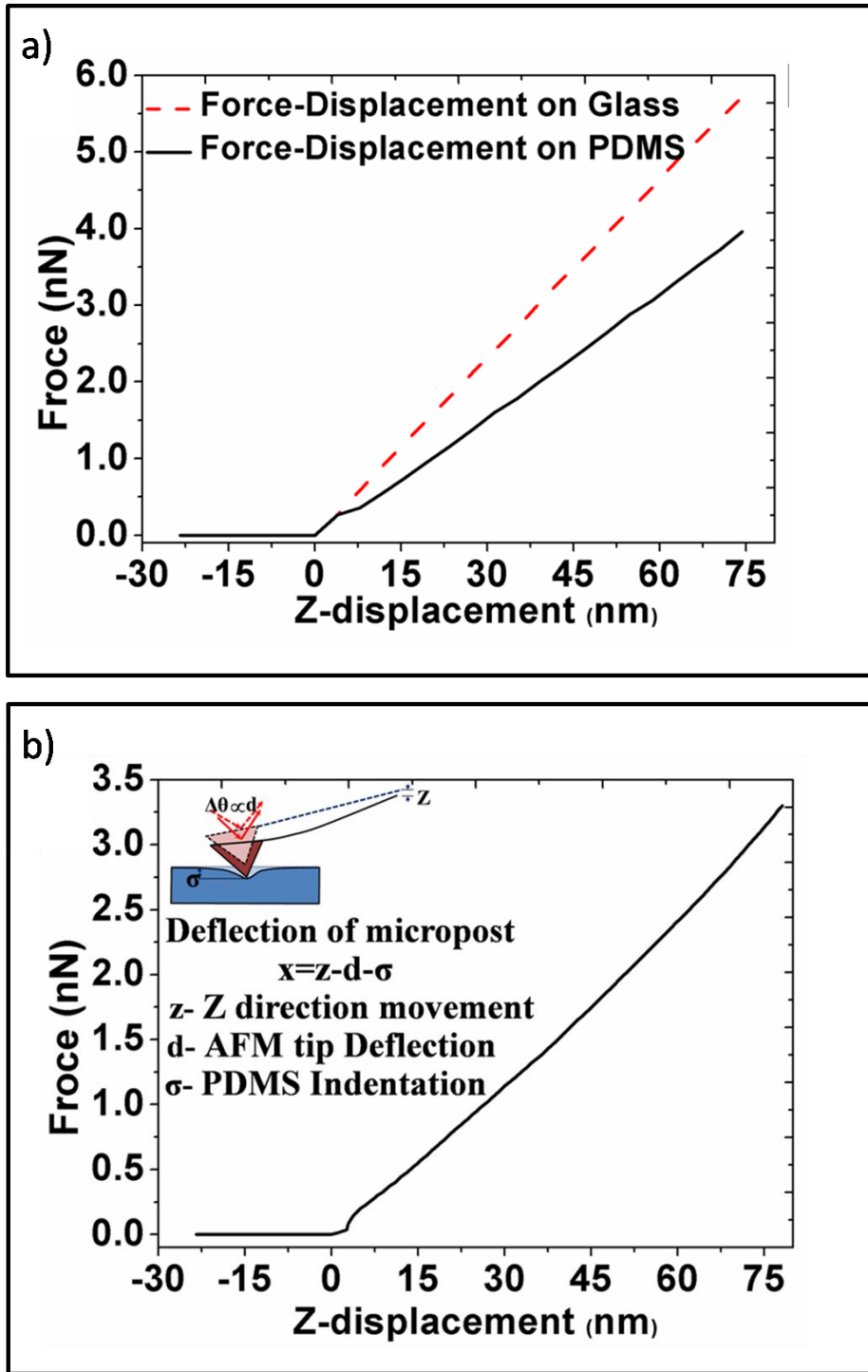


Figure 4.14. Force-displacement characteristics of the AFM cantilever beam applying forces on a) glass and PDMS substrates. b) a micropost (D: 24 μm , H: 41 μm) free end.

end because the tip's diameter is usually in nanometer range. It is much smaller than the diameter of the micropost which is in micron range. On the other hand, the AFM cantilever without tip has the size comparable to the width of the micropost. However, locating the micropost using AFM without cantilever is much easier. **Table 4.3** shows the calibration results which obtained from the calibration using AFM with and without tip. The calibration indicates that the cantilever without tip does not affect the calibration accuracy. In order to simply locate micropost center, the rest of the calibration is carried on by using AFM cantilever without the tip.

The measurement of Young's moduli are divided into 4 sets of data based on micropost size and curing temperature: 1) small dimension microposts that are cured at room temperature, 2) small dimension micropost that are cured at 65°C, 3) large dimension micropost that are cured at room temperature, and 4) large dimension microposts that are cured at 65 °C (See **Table 4.4** to **Table 4.7**). It is important to note that the posts are fabricated with exactly the same fabrication procedure and the exact dimensions measured using scanning electron microscope (SEM).

The small size micropost is defined as those posts' diameter is less than 10 μm and height is less than 30 μm . The large size micropost is defined as those posts' diameter is between 10 to 30 μm and height is between 30 to 45 μm . The Young's modulus of the first group of samples (7 small posts) are cured at room temperature are measured. The measured Young's Modulus is 0.936 ± 0.037 MPa. The measurement error is 5% which verified the validation of the calibration. The second group of samples (see **Table 4.5**) is defined as small size microposts which were cured at 65°C for 24 hours. The measured Young's modulus is 1.378 ± 0.162 MPa. Similarly, the measurement error is less than 2% which verified the validation of the calibration. The average

Young's modulus in this group is much larger than that in the first group. The 30.08% difference indicates that the curing temperature has strong effect on to the stiffness of the PDMS micropost.

The third group of samples (see **Table 4.6**) is defined as large size microposts which were cured at room temperature (23°C) for 24 hours. The measured Young's modulus is 0.543 ± 0.032 MPa. Similarly, the measurement error is less than 6% which verified the validation of the calibration. The average Young's modulus in this group is much smaller than that in the first and second group. The differences between group 1 and 3 as well as 2 and 3 are 41.99 % and 71.2 %, respectively. Those comparisons indicate that the Young's modulus of the PDMS is not only determined by the curing speed but also determined by the size of the micromold.

Table 4.4 Young's Modulus of small post cured at room temperature for 24 hours

No	Samples	Diameter (μm)	Height (μm)	Spring Constant (nN/nm)	Young's Modulus (KPa)	Curing Temperature (°C)
1	Small scale	6	13	0.0797	917	23
2	Small scale	7.3	24	0.02812	930	23
3	Small scale	7.5	25	0.02689	973	23
4	Small scale	7.6	27	0.02344	940	23
5	Small scale	7.8	25	0.02642	911	23
6	Small scale	9	13.9	0.328	911	23
7	Small scale	9.2	13.6	0.408	973	23

Although the Young's modulus should be independent of size in theory, the results indicate that curing of large post is different from that of smaller ones. This might be due to the partial curing of the large posts in comparison to small ones.

Table 4.6 Young's Modulus of large post cured at room temperature for 24 hours

Sample	Diameter (μm)	Height (μm)	Spring Constant (nN/nm)	Young's Modulus (KPa)	Curing Temp. (°C)
1	14.7	35.5	0.0803	528	23
2	18.5	30	0.346	542	23
3	13.7	38.1	0.0505	548	23
4	23.2	40.7	0.3636	575	23
5	23.2	41.7	0.3194	543	23
6	23.2	42.7	0.2963	544	23
7	24	41	0.3663	517	23
8	24	420	0.3380	513	23
9	242	396	0.4411	543	23
10	242	406	0.4121	546	23
11	247	410	0.4464	562	23
12	235	424	0.3012	511	23
13	262	370	0.7833	571	23
14	262	400	0.5949	548	23

Table 4.5 Young's Modulus of small post cured at 65°C for 24 hours

No	Samples	Diameter (μm)	Height (μm)	Spring Constant (nN/nm)	Young's Modulus (KPa)	Curing Temperature (°C)
1	Small scale	3.3	10	0.0305	1540	65
2	Small scale	5.5	15	0.0489	1230	65
3	Small scale	5.5	15.8	0.0459	1340	65
4	Small scale	9.1	10.6	1.1043	1280	65
5	Small scale	9.2	10.2	1.3659	1390	65
6	Small scale	9.31	10.8	1.3258	1490	65
7	Small scale	10	10.6	1.5292	1220	65

The last group of samples (see **Table 4.7**) is defined as the large size micropost which is cured at 65°C for 24 hours. The measured Young's modulus is 1.090 ± 0.090 MPa. Similarly, the measurement error is less than 10% which verified the validation of the calibration. The average Young's modulus in this group is much smaller than that in the second group. The difference of calibrated Young's between these two groups is 20.09 %. This result verifies our assumption that the Young's modulus of the micropost has a strong relation with the size of the micromold. Therefore, a calibration method which uses a large size micropost to implement calibration and

Table 4.7. Young's Modulus of large post cured at 65°C for 24 hours

Sample	Diameter (μm)	Height (μm)	Spring Constant (nN/nm)	Young's Modulus (KPa)	Curing Temperature (°C)
1	13.0	33.5	0.131	1170	65
2	26.7	40.0	1.3744	1180	65
3	23.2	42.9	0.6051	1110	65
4	17.8	36.0	0.3466	1090	65
5	17.8	36.0	0.3411	1080	65
6	20.0	36.0	0.5138	1020	65
7	20.0	40.0	0.3708	1010	65
8	16.6	30.8	0.3883	1010	65
9	18.7	30.8	0.7299	1190	65
10	18.1	31.9	0.5291	1090	65
11	16.3	33.4	0.2956	1050	65
12	16.3	30.1	0.4295	1120	65
13	16.3	33.1	0.3118	1080	65
14	18.1	31.9	0.5351	1110	65
15	18.1	25.9	1.0743	1180	65

then assume that the Young's modulus is similar to that of small micropost application is inaccurate. The difference of Young's temperature will increase the Young's modulus of PDMS micropost and the size of the modulus between group 3 and 4 is 50.18 %. These results indicate that the high curing micropost will also

Table 4.8 Average Young's modulus (E) of PDMS micropost as a function of size and curing temperature

Post Size	Diameter (μm)	Height (μm)	No. of sample	Avg. E (MPa)	Curing Temp. (°C)
Small	6.0 - 9.2	13.0 – 27.0	7	0.936±0.037	23
Small	3.3 - 9.3	10.0 - 15.8	6	1.378±0.162	65
Large	18.5 - 26.2	30.0 – 42.7	13	0.543±0.032	23
Large	16.1 - 26.7	30.1 - 42.9	14	1.090± 0.090	65

affect the Young's modulus. The summary of the average Young's modulus of these four groups of samples is shown in **Table 4.8** and the comparison results is shown in **Table 4.9**.

In this study, the microposts used in the biological study have a small size and they are cured and 65°C. Therefore, the Young's modulus of the material is 1.38 MPa. The spring constant of the micropost with different geometry is shown in **Table 4-10**. The spring constant of the micropost can be tuned from 487.7 nN/μm to 0.257 nN/μm if the diameter of the micropost

Table 4.9. Summary of the comparison and the corresponding p-value

Young's Modulus Comparison	P-Value
Small (23 °C) V.S. Small (65 °C)	3.42×10^{-5}
Small (65 °C) V.S. Large (65 °C)	1.12×10^{-3}
Small (23 °C) V.S. Large (23 °C)	4.23×10^{-11}
Large (23 °C) V.S. Large (65 °C)	5.48×10^{-17}

Table 4.10. Spring constant of the micropost with different geometry

Diameter (μm)	Height (μm)	Spring constant (nN/nm)
3	10	0.016452619
3	15	0.00487485
3	20	0.002056577
3	25	0.001052968
3	30	0.000609356
3	35	0.000383735
3	40	0.000257072
5	10	0.126949219
5	15	0.037614583
5	20	0.015868652
5	25	0.00812475
5	30	0.004701823
5	35	0.002960915
5	40	0.001983582
7	10	0.487688119
7	15	0.144500183
7	20	0.060961015
7	25	0.03121204
7	30	0.018062523
7	35	0.01137465
7	40	0.007620127
10	10	2.0311875
10	15	0.601833333
10	20	0.253898438
10	25	0.129996
10	30	0.075229167
10	35	0.047374636
10	40	0.031737305

changes from 3 μm to 10 μm and the height of the micropost changes from 10 to 40 μm [97].

4.3 CONCLUSION

PDMS micropost force sensor arrays are fabricated using standard microlithography, microetching and replica-molding techniques. The process of fabricating high aspect ratio PDMS micropost array are optimized and simplified. The highest aspect ratio of fabricated micropost is 13. The accurate Young's modulus of the PDMS micropost is obtained and calibrated properly using AFM. The low value Young's modulus of PDMS is not only found in large scale microposts but also in microposts cured at room temperature. The micropost calibration demonstrates that the microposts cured at higher temperature are stiffer than posts that are cured at room temperature. It also proved that large scale PDMS and small scale PDMS microposts have different Young's moduli even if they are made of the same PDMS mixture by identical fabrication methods. It should be noted that although the Young Modulus is independent of size, the PDMS microposts with different sizes had a different E values. This indicates that the curing speed of large micropost is slower than small ones. The p-values of the measured data sets were much less than 0.001 which verifies that there is significant variation between compared data sets. Finally, the microposts with small dimensions that are cured at 65 °C, which have a Young Modulus of 1.38 MPa, are used in all biological experiments. Those microposts have wide range of spring constants which is good to different biological applications.

5. STUDIES OF VASCULAR SMOOTH MUSCLE CELL TRACTION FORCE ON MICROPOST ARRAY

Vascular smooth muscle cell (VSMC) exerts forces ranging from ~10 nN to 200 nN in resting state. This force range is measured using the high aspect ratio micropost arrays. The VSMC adaptation to its physical environment is studied. When a cell is plated on a micropost array, it grows and attaches to its top surface and deflects it by applying traction force. The micropost's deflection is measured by comparing the position of the top and the bottom ends of the bent microposts. This is achieved by extracting the outline of the same micropost from top and bottom images which are captured by confocal microscope during the biological experiment. The corresponding traction forces are calculated by applying the micropost's spring constant to the force-displacement equation. The statistical techniques are used to obtain more accurate results.

The changes of physical environment surrounding VSMC are accomplished by changing the geometry of the micropost array, and in the chemical environment by adding angiotensin II or cytochalasin D to the cell bathing solution during the biological experiment. The reaction of the VSMC to these changes of physical and chemical environment is evaluated. Integrin-linked kinase (ILK) is a serine/threonine protein kinase implicated in signaling pathways involved in VSMCs proliferation and migration. Micropost array is also used to analyze the effect of ILK molecule on the mechanical forces exerted by VSMCs. Two types of cells are plated on different micropost arrays with same dimensions and similar mechanical properties. One is a control-

unmodified VSMC (control group) and the other is VSMC in which ILK has been genetically knocked down (experimental group). For an experiment, these two types of cells were grown on micropost arrays, angiotensin II or Cytochalasin D are added to VSMC media and the responses of the cells are quantified and compared by using the micropost array.

5.1 PREPARATION OF BIOLOGICAL STUDY

5.1.1 CONFOCAL MICROSCOPE AND EXPERIMENT SETUP

Confocal microscopy is used to increase optical resolution and contrast of a micrograph by using point illumination and a spatial pinhole to eliminate out-of-focus light in specimens that are thicker than the focal plane. It enables the reconstruction of three-dimensional structures from the obtained images. The confocal microscope scans the micropost array at different levels along the Z-axis in programmable steps. For example, if a micropost array with 25 μm height is used, a 25-step scans are used to extract the top and the bottom image with a 1 μm ramp steps.

Schematics of the experimental setup are shown in **Figure 5.1**. VSMCs are cultured on top of the micropost arrays in a petri dish with 1-1.5 mL cell culturing media and incubated for 2 days before image acquisition. The micropost array is mounted and observed by an Olympus Fluoview1000 confocal microscope with 60X water objective. A series of wide-field optical images are created by scanning the micropost array. All captured optical images are recorded in real time. The outline of each micropost is extracted from the captured images. The center position of the micropost top vs. bottom from these images is compared to obtain the deflection.

5.1.2 DEVICE PREPARATION AND CELL CULTURING EXPERIMENT

Isolated vascular smooth muscle cells (VSMCs) extracted from a male Sprague-Dawley rats (250-350 g) are cultured on top of the micropost arrays. The cell culturing experiment follows a standard protocol:

- Add the Dulbecco's Phosphate-Buffered Saline buffer (DPBS) or balanced salt solution 2 to 3 mL to the culture dish growing VSMCs and wash 2-3 times.
- Add appropriate amount of trypsin (0.5 mL) and incubate at 37 °C in a 5% CO₂ incubator for 5 minutes, mixing and gently shaking intermittently.
- Resuspend cells in appropriate medium and wash and repeat 2-3 times.

The PDMS micropost arrays are fixed at the bottom of a glass culture dish and are exposed to the UV light for 30 minutes for sterilization. Prepared cells are resuspended on top of the micropost array and incubated at 37 °C in a 5% CO₂ incubator for cell growing. After 2 days, the cells are ready for the biological experiment.

Initially, most of the cells did not grow on top of the micropost array. Instead, they grew on the substrate between microposts. This might be due to the large spacing between microposts and the PDMS is not adhesive enough to cells. Some research groups have coated the micropost array with a biologically compatible protein to make micropost's top surface sticky to vascular cells [92-95]. We have solved this problem by reducing the space between microposts and by modifying the PDMS property to make it sticky to the cells.

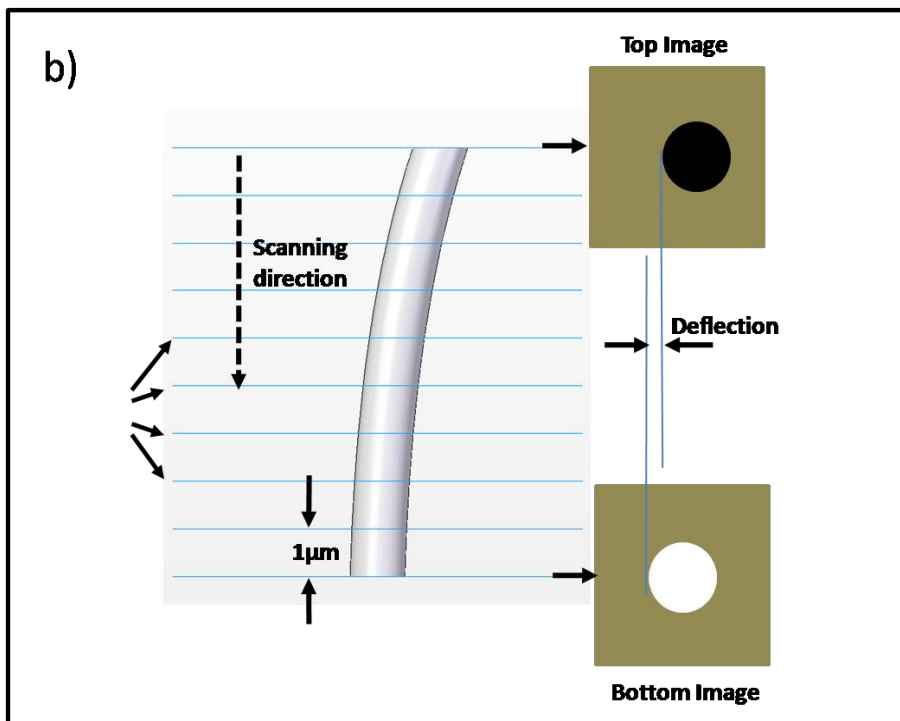
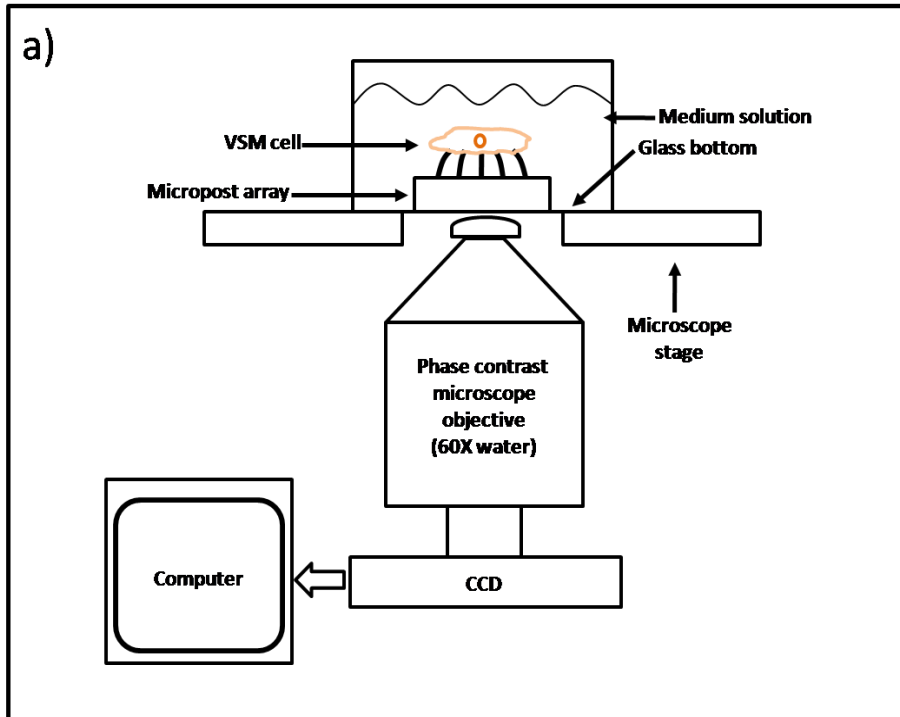


Figure 5.1. a) Schematic of cell experiment setup; b) extracting top and bottom images

A solution to increase the cell adhesion to the micropost top was to change the property of PDMS by treating the top surface of the micropost with oxygen plasma using RIE. Oxygen plasma changes the property of cured PDMS from hydrophobic to hydrophilic which persists for a couple of hours. The hydrophilic property makes cell adhere more easily to PDMS. In order to change this property in the selected area, a voltage bias is applied during the reactive ion etching process. The ionized oxygen becomes anisotropic and only the top of the micropost array is reacted with the plasma altering its adhesive property to the cell.

The advantage of using oxygen plasma is the simplicity and short duration of the process (less than 1 minute), low power which will not destroy the micropost with high aspect ratio, and, the oxygen plasma just changes the PDMS surface property temporarily which will not influence the calibrated stiffness or spring constant.

5.1.3 IMAGE PROCESSING

A phase contrast microscope installed on the AFM is used to continuously collect the images of the microposts that are covered by cell from their top to bottom. The bottom base of the micropost is treated as zero reference height. The images captured at zero height and at the top surface of the micropost, are extracted and named as ‘bottom’ and ‘top’ images, respectively. The image processing using Matlab is done to detect and measure the micropost’s deflection.

A. GENERAL DESCRIPTION OF THE IMAGE PROCESS

The captured images are processed to extract the micropost outline and then to determine the center position of each micropost covered by VSMC. The tool used to implement image processing is Matlab using its image processing tool functions. The original recorded images are in gray scale (intensity image). The image is converted to a matrix where every element is named

a pixel and has a value corresponding to the pixel intensity value. In a gray scale image, an integer between 0 and 255 is assigned to a pixel to represent its brightness. The value 0 corresponds to black and 255 to white. In our case, the gray scale image which is converted to a matrix is processed using different methods (functions) to differentiate microposts from its background. **Figure 5.2** shows the flow diagram to implement such image processing.

B. IMAGE PROCESSING OF THE ‘BOTTOM’ IMAGE

After reading the image to Matlab, the gray level of the image is adjusted to enhance the image quality. The first method used is called “stretching the gray scale” which is a technique that stretches the gray scale values of the input image to occupy the entire range of 8 bit binary

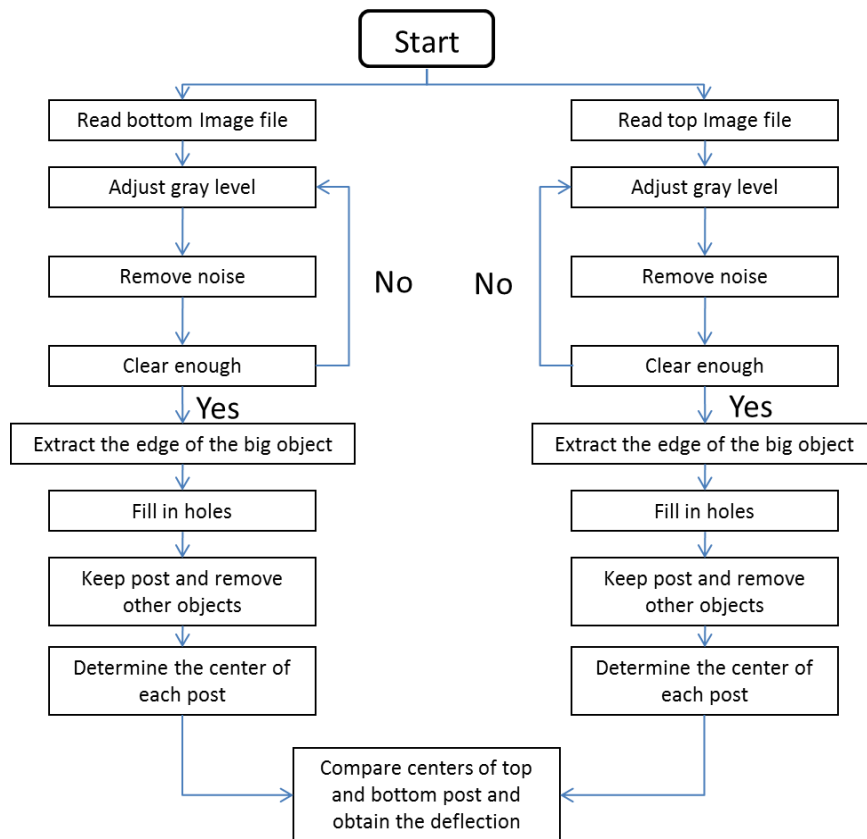


Figure 5.2. Flow diagram of image processing

value ranging from 0 to 255. The algorithm of the first method is:

1. Measure the minimum and maximum gray value of the input image.
2. Map each pixel in the input image onto 0 to 255 using the following equation:

$$Y = \Delta (X - G_{min});$$

$$\Delta = 255 / (G_{max} - G_{min})$$

where X is the gray level of the pixel in the input image, Y is the gray level of the pixel in the output image, G_{min} is the minimum gray level of the input image, G_{max} is the maximum gray level of the input image. The second method used to enhance the image quality is histogram equalization [97]. Histogram measures the number of pixels which have a particular intensity in an image. The purpose of this method is to make the histogram of the output image match a uniform distribution as close as possible. The gray level of the pixel in the image is able to be redistributed evenly within 0-255 using histogram equalization algorithm. The algorithm of histogram is listed below:

1. Read an image file.
2. Measure the H_i – the histogram of the input image.
3. Calculate C_i – the cumulative distribution function of the input image using H_i .
4. Make the target C_t .
5. Mapping C_i on C_t .
6. Transform the input image pixel intensities using the mapped C_t .

The original captured image at the bottom of the micropost array with diameter, height and spacing of 7 μm , 25 μm and 7 μm , respectively, and the corresponding image after enhancement process using the methods mentioned above are shown in **Figure 5.3a** and **3b**, respectively.

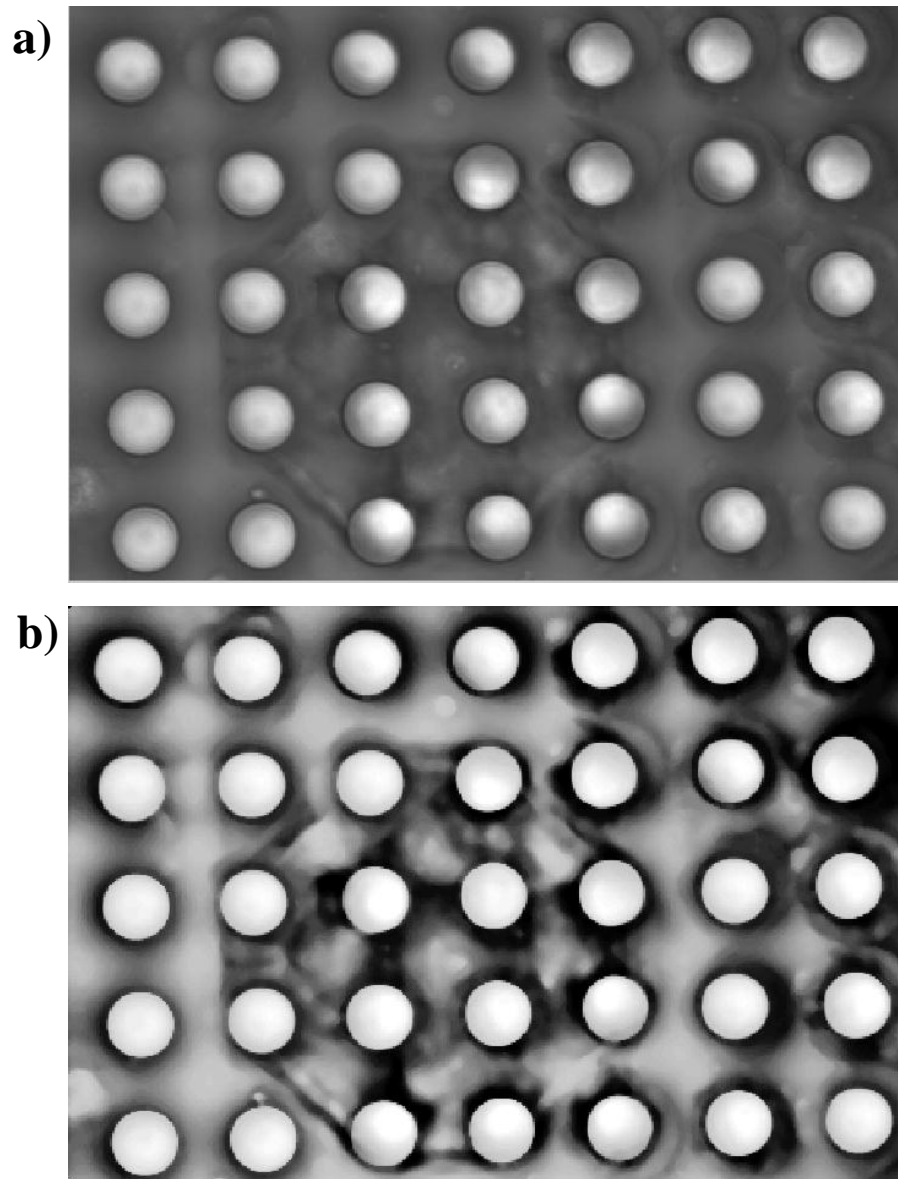


Figure 5.3. a) Image before processing, b) image after processing

It should be noted that the processed image possesses better contrast and the outline of the micropost is much sharper than the original one. The outlines of each micropost are extracted using 'edge' function in Matlab with the methodology of 'sobel' and 'log'. The Sobel method

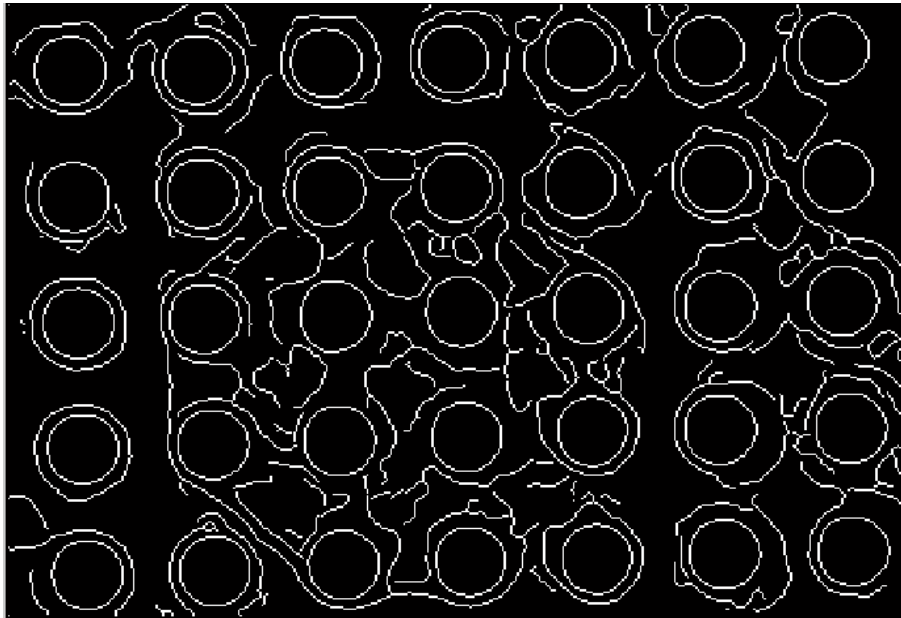


Figure 5.4. The extracted outline of the micropost

finds edges using the Sobel approximation to the derivative. It returns edges at those points where the image gradient is a maximum. While the 'Log' method which is also named as the Laplacian of Gaussian method finds edges by looking for zero crossings after filtering image with a Laplacian of Gaussian filter. The final outlines are the union of the outlines extracted by those two methods. **Figure 5.4** shows the microposts' outlines which is extracted using Matlab. It should be noted that the image after edge extraction process is changed from unit 8 format to

binary format. Since the contrast between micropost and the background is large. The outlines of micropost extracted by Matlab are enclosed circles. Such enclosed patterns will easily become ‘while holes’ if specific Matlab image processing function is used. However, besides the

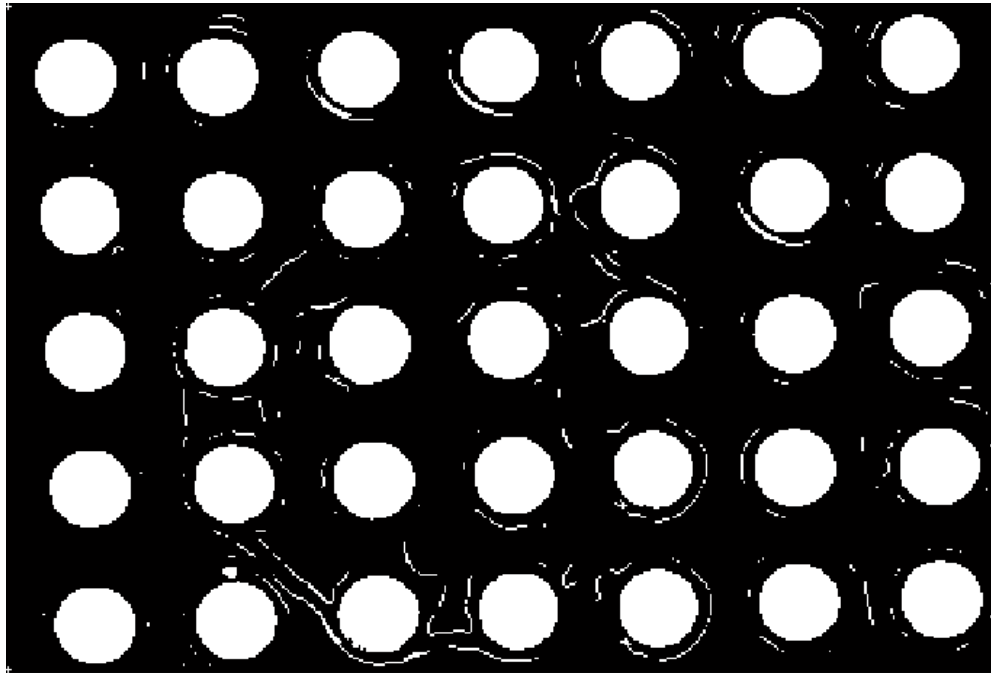


Figure 5.5.Images after filling the outlines of the microposts with white color

extracted outlines of the microposts, the profiles of other objects such as particles, shadows of micropost and other background noise have also been extracted. Therefore, the next image processing step is to use Matlab function, for example, ‘imfill’ and many others to ‘fill’ the close ‘holes’ (the enclosed outlines) by white color. **Figure 5.5** is the image after ‘filling holes’ process. Then the binary image is scanned and the detected objects with white color are labeled as object 1, object 2 automatically using function ‘bwlabel’ in Matlab. Obviously, those objects

include microposts as well as other small things such as small particles or background noise. Those background objects are filtered by using a thresholding technique based upon the pixel numbers in them. If the pixel number is small, the object is obviously not micropost and is moved away. Finally, the remaining objects are relabeled and microposts are counted at this time.

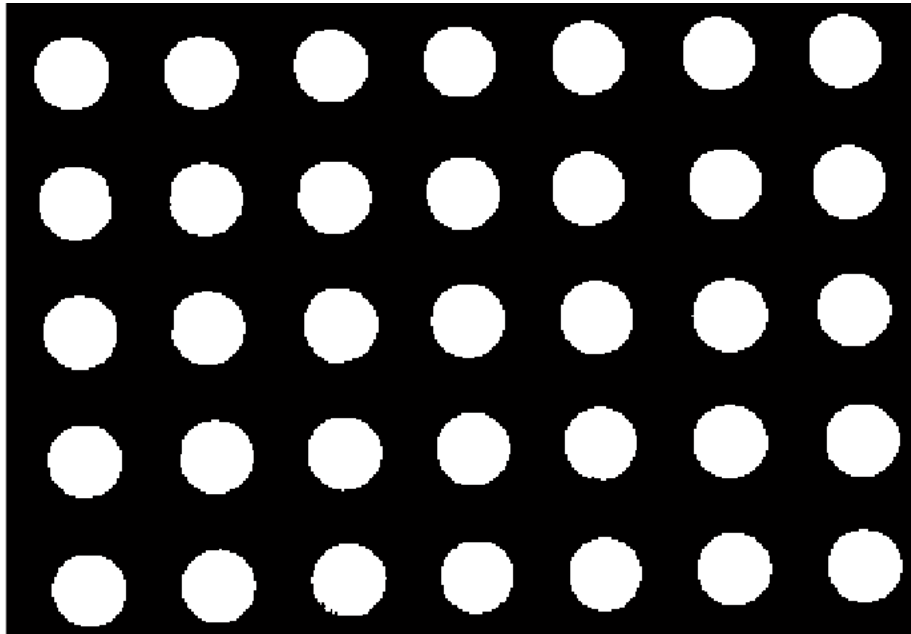


Figure 5.6. The micropost mask after image processing

C. IMAGE PROCESSING OF 'TOP IMAGE'

The image processing of 'top' image is different from the 'bottom' image. **Figure 5.7** shows the top image captured. Obviously, the top image is more difficult to process because the outlines of the microposts are usually merged with the outlines of the cell. Therefore, we cannot use the function 'edge' in Matlab to get the mask of the micropost on top image easily.

The microposts which are not covered by VSMC in the top image can be extracted using the same method mentioned in previous section. After determining the boundary of such micropost, the average gray levels in the pixels are calculated. Obviously, the micropost's gray

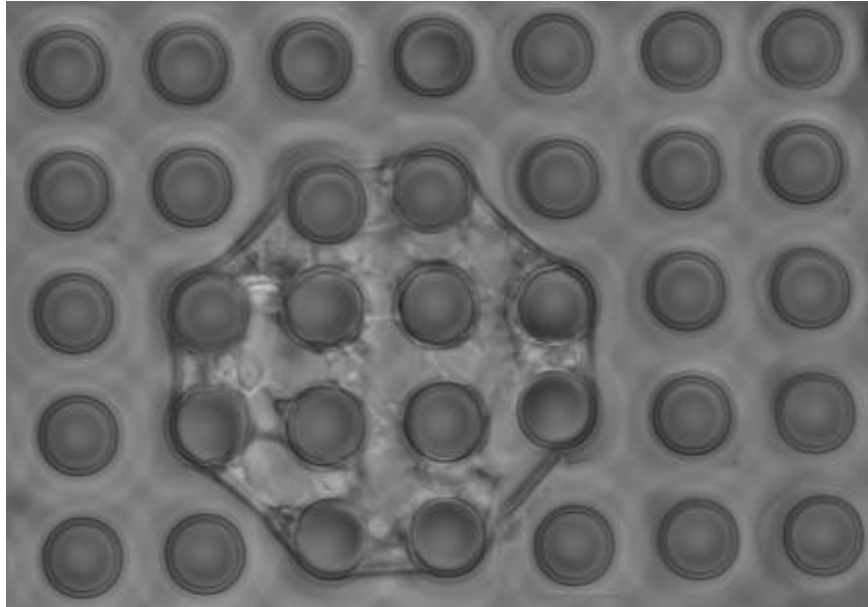


Figure 5.7. The ‘top’ image of a micropost with cell growing on top

levels and the outline of the cell are different. Then, the micropost region covered by the VSMC is determined using another Matlab function called ‘roicolor’. Those regions including the pixels which have the gray level close to the value calculated earlier are counted and converted to black color. The rest area of the image is converted to white color. The processed binary image is plotted to act as the ‘mask’ of the micropost. **Figure 5.8** is the processed image. The area within the red circle contains the microposts covered by the VSMC. It should be noted that the microposts are deflected away from their original position. The next step is to remove the small objects and noise from the image. The processing steps for filtering noise are similar to those

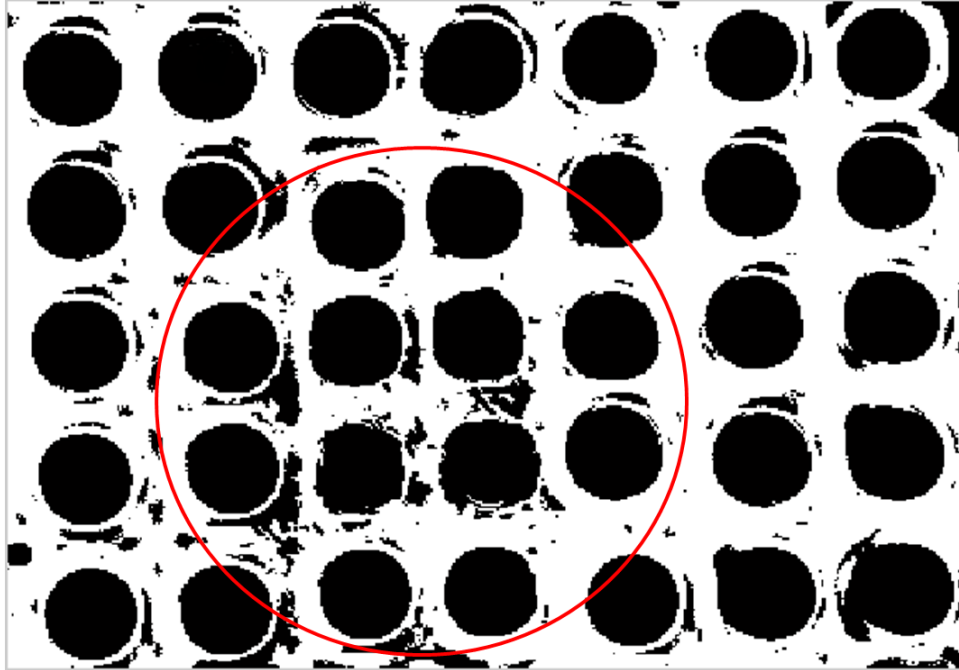


Figure 5.8. The ‘top’ image of a micropost after first image processing

used in bottom image processing. **Figure 5.9** is the image which obtained after noise reduction processing using Matlab.

There is a big difference between the extracted masks in **Figure 5.6** and **Figure 5.9**. The extracted outline of micropost in **Figure 5.6** is very smooth. The shape of the micropost is known to be smooth while the extracted outline in **Figure 5.9** is very coarse and the size of the extracted micropost is not uniform. Since the size of the micropost on both end should be the same. We have used the following method to make the compensation of the top to improve the quality of image processing:

1. The objects in **Figure 5.9** are labeled using ‘BWLablel’ function in Matlab.

2. The average size of the micropost is decided by the image processing of the ‘bottom’ image. The average size is used to create a reference circle.

3. Determine the geography center’s coordination (x, y), which are in pixel unit, for each labeled white object in **Figure 5.9** using function ‘regionprops’. The same coordination is also used as the center of the reference circle.

4. Calculate the overlapped area of reference circle and the labeled white object.

5. Give the center’s coordination for each labeled object an offset, for example, set the center coordinate from (x, y) to (x+1, y+1) and repeat step 4 and calculate the new overlapped

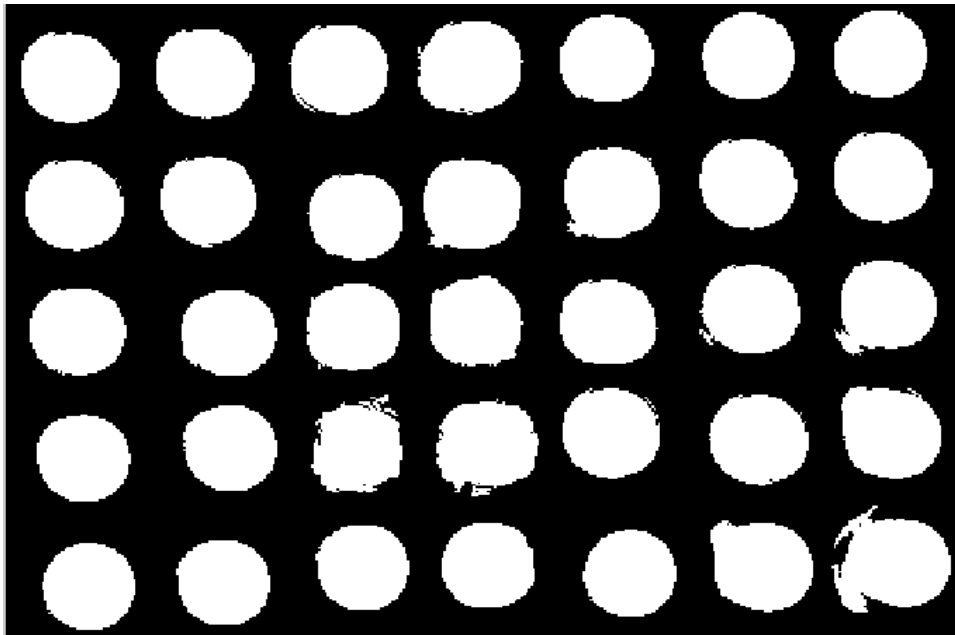


Figure 5.9. The ‘top’ micropost mask after processing

area.

6. The center's coordination which gives the largest overlapped area is treated as the center position of the micropost on the top image. The white objects in **Figure 5.9** are also replaced by the reference circle.

Figure 5.10 is the final micropost mask for the top image after image processing. The difference of the center position of the same micropost in the top and bottom image is calculated. Such difference is converted to the deflection of the micropost and used to calculate the applied traction force by VSMC.

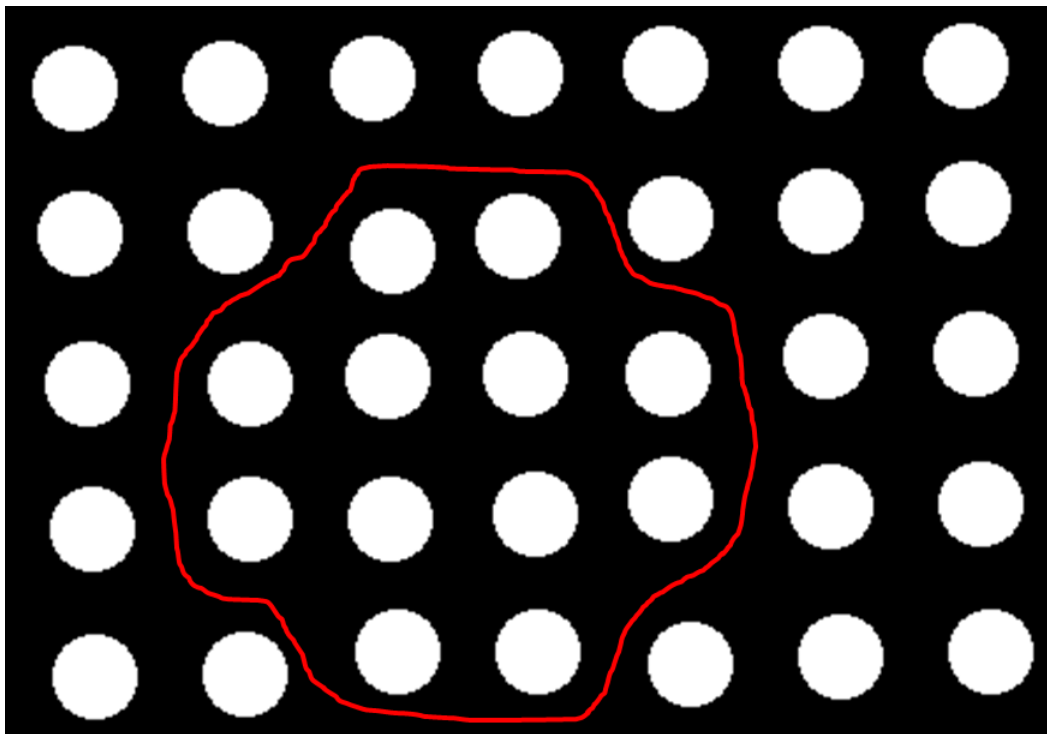


Figure 5.10. The mask of microposts in top image after filtering noise

Figure 5.11a shows the whole optical image of one VSMC cultured on a micropost array with diameter, height and spacing of 7 μm , 25 μm and 3 μm , respectively. **Figure 5.11b** and **c** show the extracted ‘bottom’ and ‘top’ images. These two images are obtained using a self written pattern recognition image processing software, called ‘masks’ (**Figure 5.11e** and **f**). The center coordinates of each micropost in top and bottom masks are determined. Since the bottom of the micropost is fixed and is used as a reference, its top is shifted by the cell traction force (**Figure 5.11a** and **d**). The largest measured deflection is 2.7 μm which corresponds to a force of 36.4 nN generated by the cell. **Figure 5.11d** shows the traction force distribution of single VSM cell growing on the micropost array.

5.2 STEADY REACTION OF VSMC USING MICROPOST ARRAY

5.2.1 VALIDATION OF THE MICROPOST FORCE SENSOR

VSMCs are grown on top of micropost arrays (100×100) with two different geometries. One has diameter, height and spacing of 5 μm , 25 μm and 7 μm , and the other has diameter, height and spacing of 3 μm , 25 μm and 5 μm , respectively. **Figure 5.12** shows the SEM micrographs of VSMCs grown on these two types of arrays. The SEM micrograph shows microposts are covered by VSMC and are squeezed to the center and some of them touch each other. This is likely due to the fixation and dehydration processes that are performed using the critical point dryer which is necessary for high vacuum environment. High quality and high aspect ratio PDMS micropost array are used in this study. After applying calibrated Young’s Modulus (E) and the geometry of PDMS micropost (height and diameter) to the beam bending theory, the spring constant of the micropost is calculated. For example, the spring constant of the

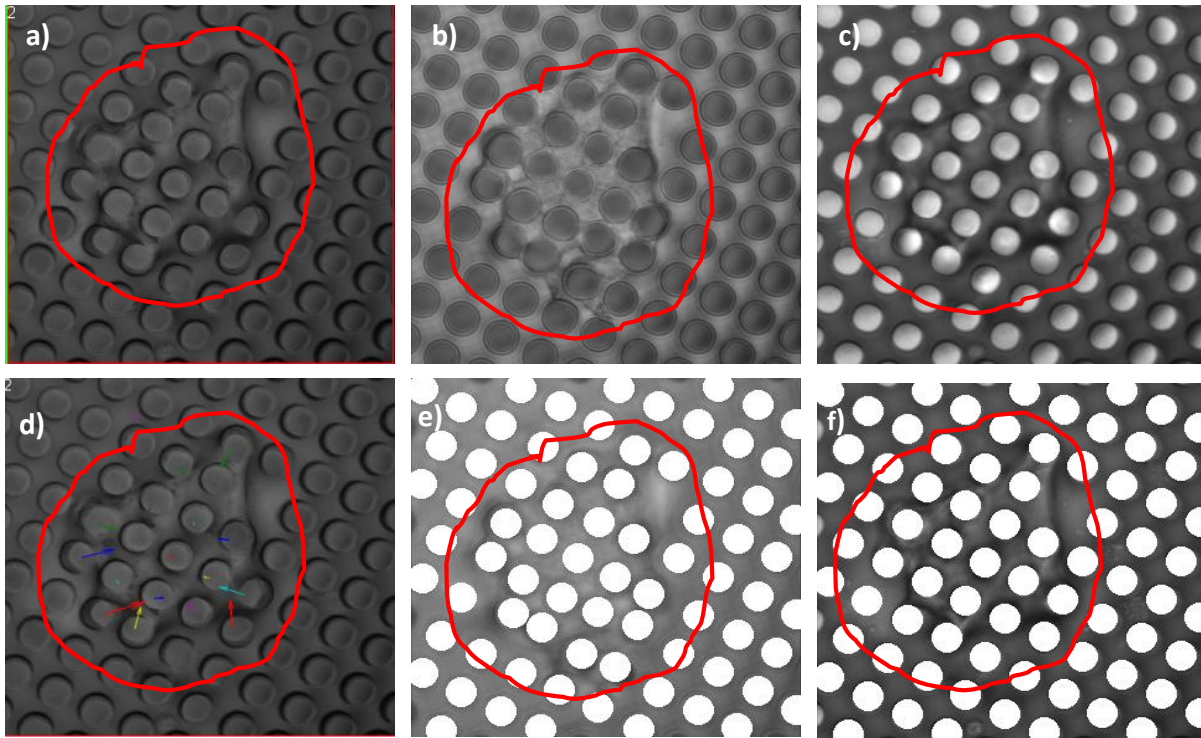


Figure 5.11. a) phase contrast image of one cell cultured micropost array with diameter, height and spacing of 7 μm , 25 μm and 3 μm ; b) and c) shows the extracted 'bottom' and 'top' images; d) traction force distribution map; e) and f) 'masks' of bottom and top images

micropost with diameter and height of 5 μm and 25 μm , respectively, is 8.12 nN/ μm and that of the micropost with diameter and height of 3 μm and 25 μm , respectively is 1.05 nN/ μm . A single pixel of the white field optical image taken by Olympus Fluoview1000 represents a square with area of 400 nm \times 400 nm. Therefore, the minimum detectable traction force for those microposts is 1.622 nN and 0.21 nN, respectively. The largest detectable traction force is limited by the spacing between adjacent microposts. It is 97.08 nN for micropost array with diameter, height and spacing of 5 μm , 25 μm and 7 μm , respectively, and is 8.73 nN for micropost array with diameter, height and spacing of 3 μm , 25 μm and 5 μm , respectively. We assume that the force sensor array consists of vertically

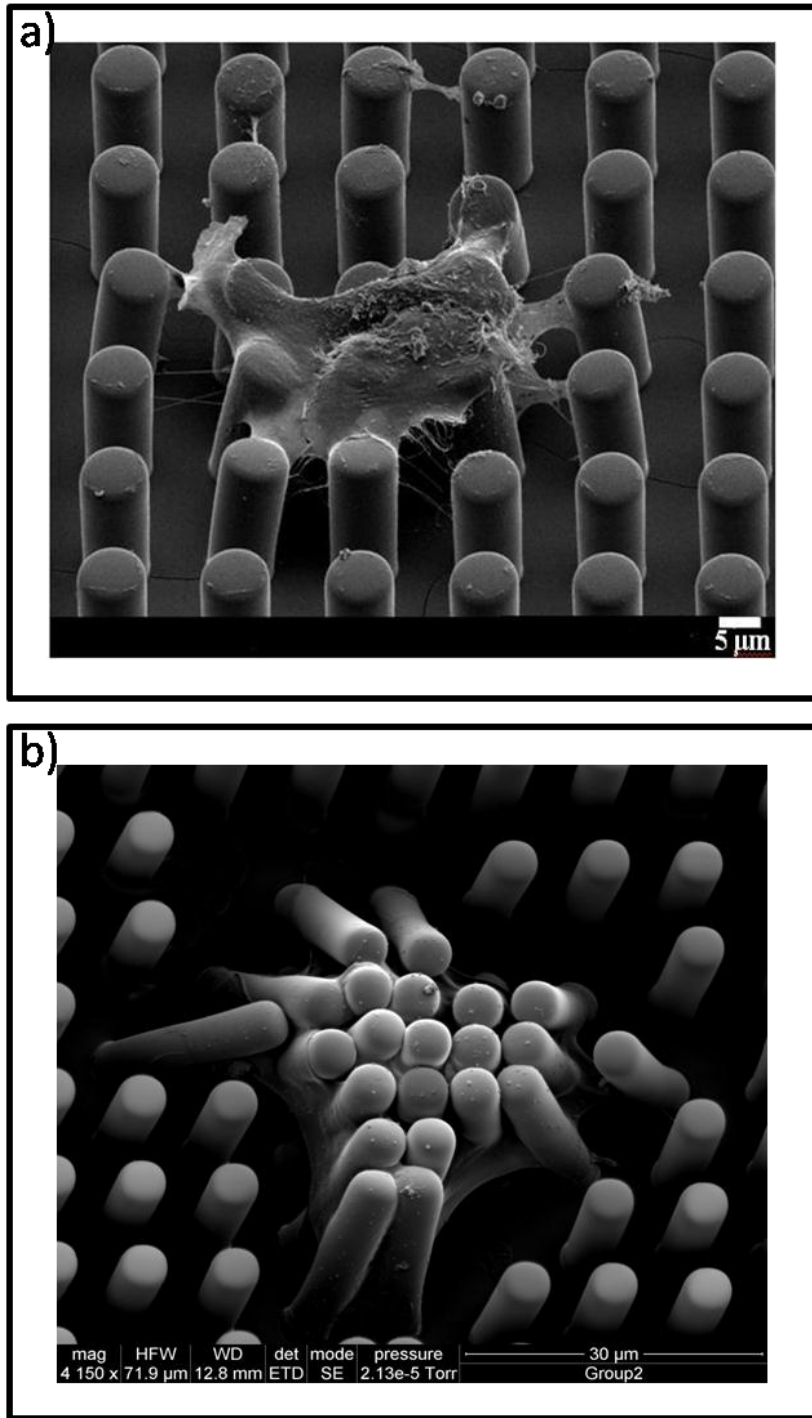


Figure 5.12. Single VSMC grown on micropost array with two different geometries: (a) diameter, height and spacing of 7 μm, 15 μm and 7 μm, respectively (b) diameter, height and spacing of 3 μm, 25 μm and 5 μm, respectively

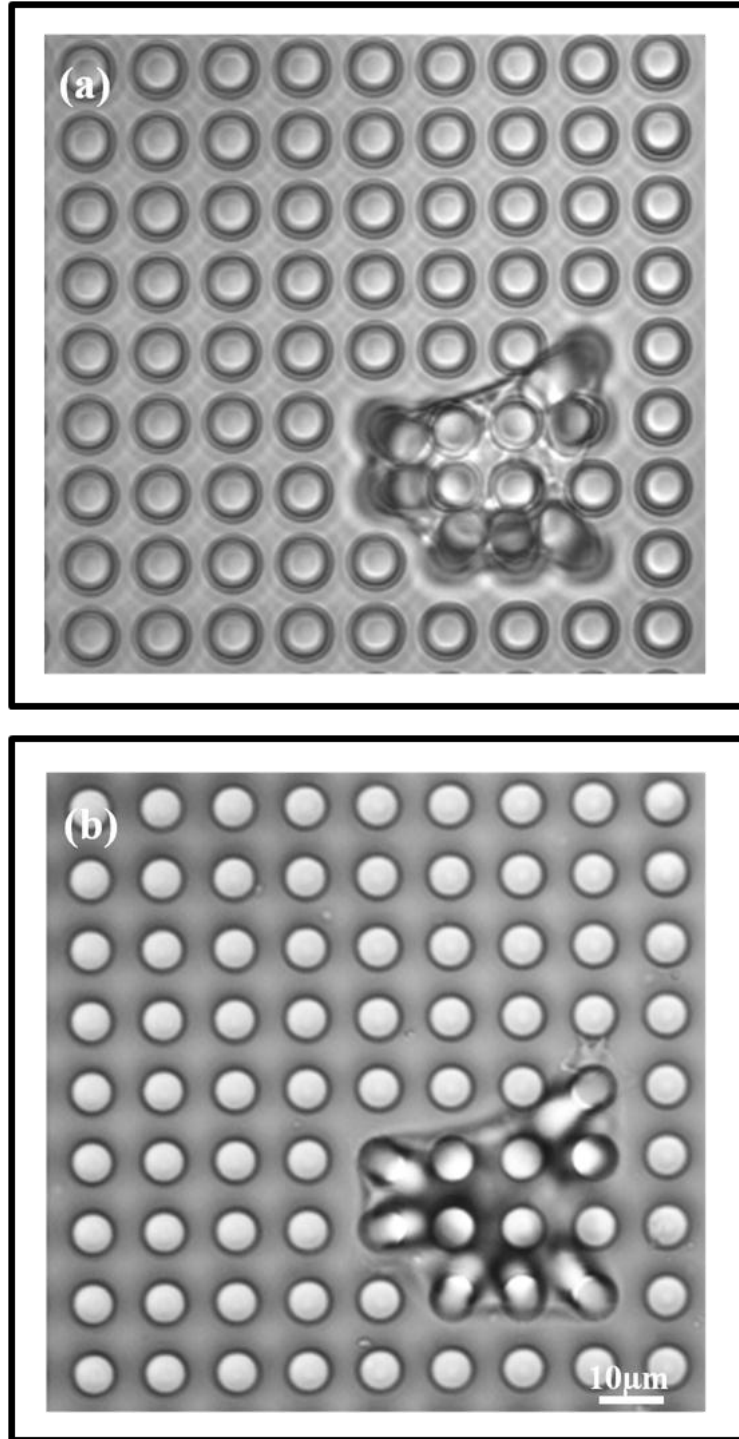


Figure 5.13. Wide-field optical images of single VSMC grown on micropost array with diameter, height and spacing of 5 μm , 25 μm and 7 μm , respectively: (a) recorded at top of the micropost array (b) recorded at bottom of the micropost array, respectively.

standing PDMS microposts which means that those microposts with no cell grown on are able to keep their shape unchanged when emerging in the medium solution and all through the cell experiment. In order to verify that the microposts without cells are kept intact during the experiment, the top and bottom positions of the same microposts in optical images are compared initially. It is found that there is no position change of such microposts without cell in these images. It verifies our assumption that the microposts with such geometry are ‘strong’ enough to vertically be stable in the solution. **Figure 5.13** shows the micropost array with diameter, height and spacing of 5 μm , 25 μm and 7 μm , respectively, used in cell experiment. By calculating the center position of each micropost in both bottom and top images, the average deflection of microposts with no cell is 0.348 pixel which is less than the minimum detectable displacement. Therefore, the deflection of micropost with no cell on top can be neglected and the assumption that the micropost can stand vertically in media is correct. On the other hand, the microposts covered by cell have the average deflection of 8.81 pixels which is much larger than that of the microposts without cell. In general, this experiment demonstrates that use micropost array to measure the traction force of VSMCs is effective and accurate.

5.2.2 STEADY STATE RESPONSE OF VSMC TO MICROPOST ARRAY WITH DIFFERENT STIFFNESS

A. STUDY OF VSMCS

Normal VSMCs have been studied using the micropost arrays with geometries mentioned above. **Figure 5.5** shows the white field optical images of single VSMC grown on these

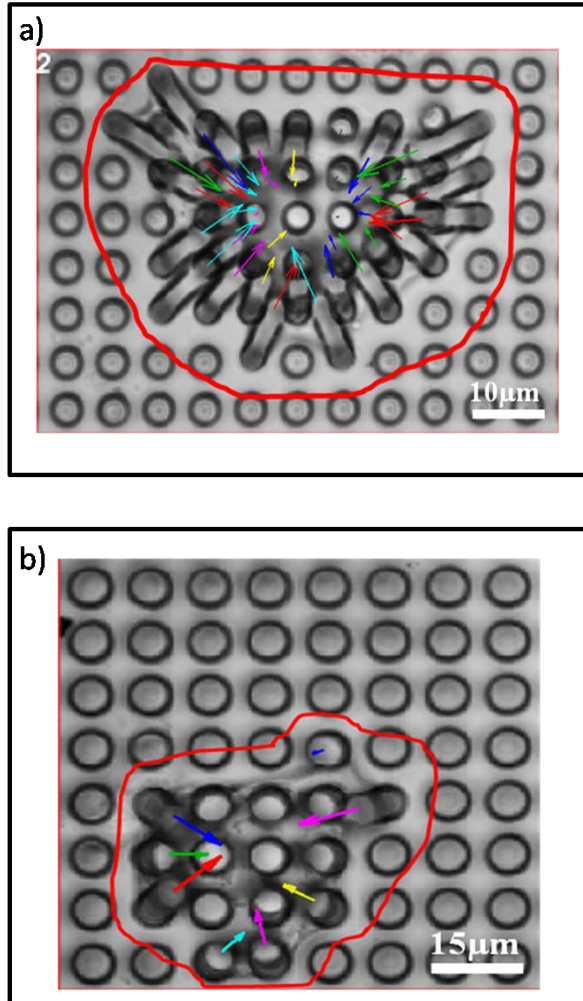


Figure 5.14. White field optical images of single CK₄ cell grown on micropost array with a) 3 μm in diameter, 25 μm in height and b) 5 μm in diameter, 25 μm in height, respectively. The arrow's length in figure 7a is magnified 8 times to make it long enough to be seen.

micropost arrays and the corresponding force distributions maps. The VSMCs can grow and spread on top of PDMS micropost array well. The arrows in the figure point toward direction of deflection physical center at all posts covered by the cell. The analysis of traction forces also

shows that the forces are small around the center region of the cell compared to the forces near the cell edge. The average deflection of the micropost in **Figure 5.14 (a)** is 22.18 pixels which equals to 8.87 μm and is 9.77 pixels which correspond to 4.31 μm in **Figure 5.14(b)**. It indicates that the micropost array with higher aspect ratio (8) can generate much more deflection than that

Table 5-1. Average deflection of the micropost and corresponding traction force generated by cells on micropost arrays with different geometries

Micropost geometry			Spring constant (nN/nm)	Average displacement @ edge (μm)	Average displacement @center (μm)	Average force at edge (nN)	Average force at center (nN)
Height (μm)	Diameter (μm)	Spacing (μm)					
20	3	10	0.00138	9.72	3.63	13.41	5.01
30	5	5	0.00315	5.4	2.22	17.03	7.01
20	5	5	0.01065	2.8	0.78	29.82	8.31
30	7	3	0.01212	2.78	1.136	33.69	10.47
40	10	7	0.02130	3.65	1.95	77.78	41.48
20	7	10	0.04091	4.96	1.18	202.7	48.27
30	10	3	0.05048	4.31	1.03	217.7	51.94

with lower aspect ratio (5). Therefore, micropost array with diameter, height and spacing of 3 μm , 25 μm and 5 μm , respectively, can be used to measure a smaller traction forces generated from other types of cells. However, the average traction force of the VSMCs generated on the two micropost array was 9.31 nN (diameter and height of 3 μm and 25 μm) and 31.71 nN (diameter and height of 5 μm and 25 μm). The same experiment is repeated 6 times to verify the universality. **Table 5.1** shows the experiments results of average deflection of the micropost and corresponding traction force generated by cell. It is found that the average traction force generate by VSMC growing on micropost array 1 and 2 is 8.00 nN and 51.14 nN, respectively. They demonstrated that VSMCs tends to exert larger traction force when they grow on stiffer

micropost array. Such behavior from the normal VSMCs (CK₄ cells) in the remainder of the thesis are tested using microposts with different geometries. After image processing, the deflections and the corresponding traction forces are summarized in **Table 5.2**. It can be seen, as the spring constant of the micropost increases, the traction force applied by CK₄ cell also increases. The traction force applied on micropost as a function of the spring constant is also plotted in **Figure 5.15**. The microposts on the ‘edge’ are defined as those microposts covered by the cell at its boundary. The microposts in the ‘center’ are defined as those microposts covered by the cell within its boundary. From the above analysis, it could be concluded that CK₄ cell has the ability to adapt to its physical environment by changing the level of its traction force.

Table 5.2 Traction force from the labeled posts as a function of observation time

Post	Before experiment (nN)	ANGII 3min (nN)	ANGII 6min (nN)	ANGII 20min (nN)
1	63.4	69.39	79.27	71.55
2	61.8	65.39	77.27	70.55
3	51.09	58.35	66.63	55.26

After analyzing the behavior of CK₄ cell in normal conditions, Angiotensin II, a hormone, that causes blood vessels to vasoconstrict was diluted to 10⁻⁵ M/ml solution by DPBS and added to CK₄ cells. The effect of angiogenesis II on cells was analyzed by observing the bending variation of microposts covered by the VSMCs. This process was recorded by camera with 10 frames/min scanning rate for 45 minutes after the injection of ANGII to the culture dish. After that, Cytochalasin D, which depolymerizes the actin cytoskeleton, was diluted to 10⁻⁷ M/ml by DPBS and injected to the culture dish. The effect of Cytochalasin D on VSMCs can be analyzed by observing the change of deflection of microposts. The same optical images were continuously recorded for 30 minutes after injection of Cytochalasin D. The image of the cell after adding

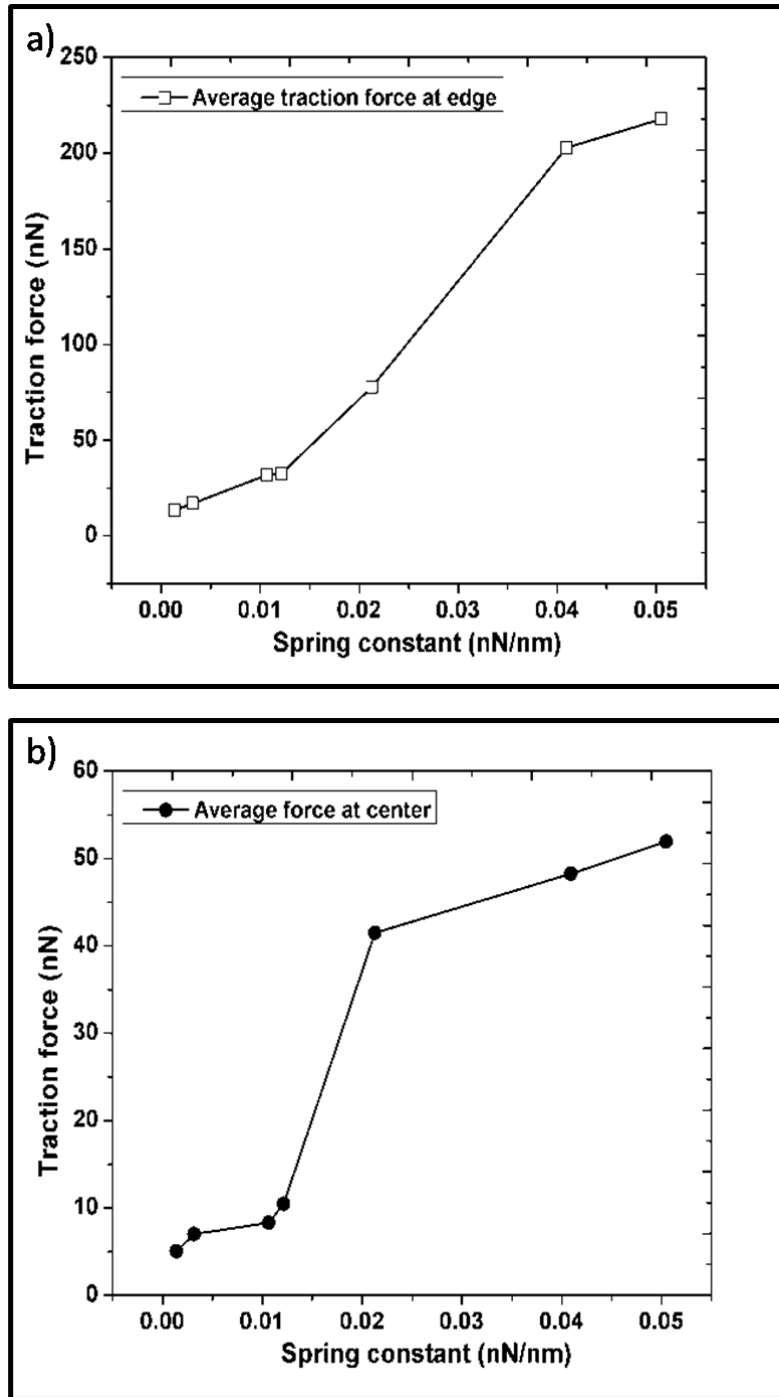


Figure 5.15. Traction as a function of the spring constant of the micropost a) @ the edge of the cell and b) @ the center of the cell.

ANG II and CYTO were obtained and compared by recording and analyzing the micropost deflections. The above experiment was implemented using micropost array with diameter, height and spacing of 5 μm , 25 μm and 7 μm , respectively.

The dynamic change and traction force distribution map of a single CK₄ cell after adding ANG II and subsequently CYTO, are shown in **Figure 5.16 a-e**. The optical image recorded prior to adding ANGII to the CK₄ cell (**Figure 5.16a**) shows that CK₄ cell generates steady state traction force on the micropost array. The images recorded 3 minutes, 6 minutes and 20 minutes after adding ANGII are shown in **Figure 5.16b–d**, and 40 minutes after adding CYTO is shown in **Figure 5.16e**. Micropost labeled by 1 (in **Figure 5.16a**) shows the deflection equivalent to the traction force of 63.4 nN (before adding ANGII). This force has increased to 69.4 nN (3 min after adding ANGII) and to 79.3 nN (6 min after adding ANGII). The traction force has decreased to 71.6 nN (20 min after adding ANGII). The results show that ANGII leads to a contractile response in the CK₄ cell. The cell contracted for 6 minutes. Then, the contractile effect subsides and the cell tends to recover its original morphology. A pronounced cell relaxation occurs 15 minutes after adding the CYTO to CK₄ cell and it persisted for more than 30 minutes.

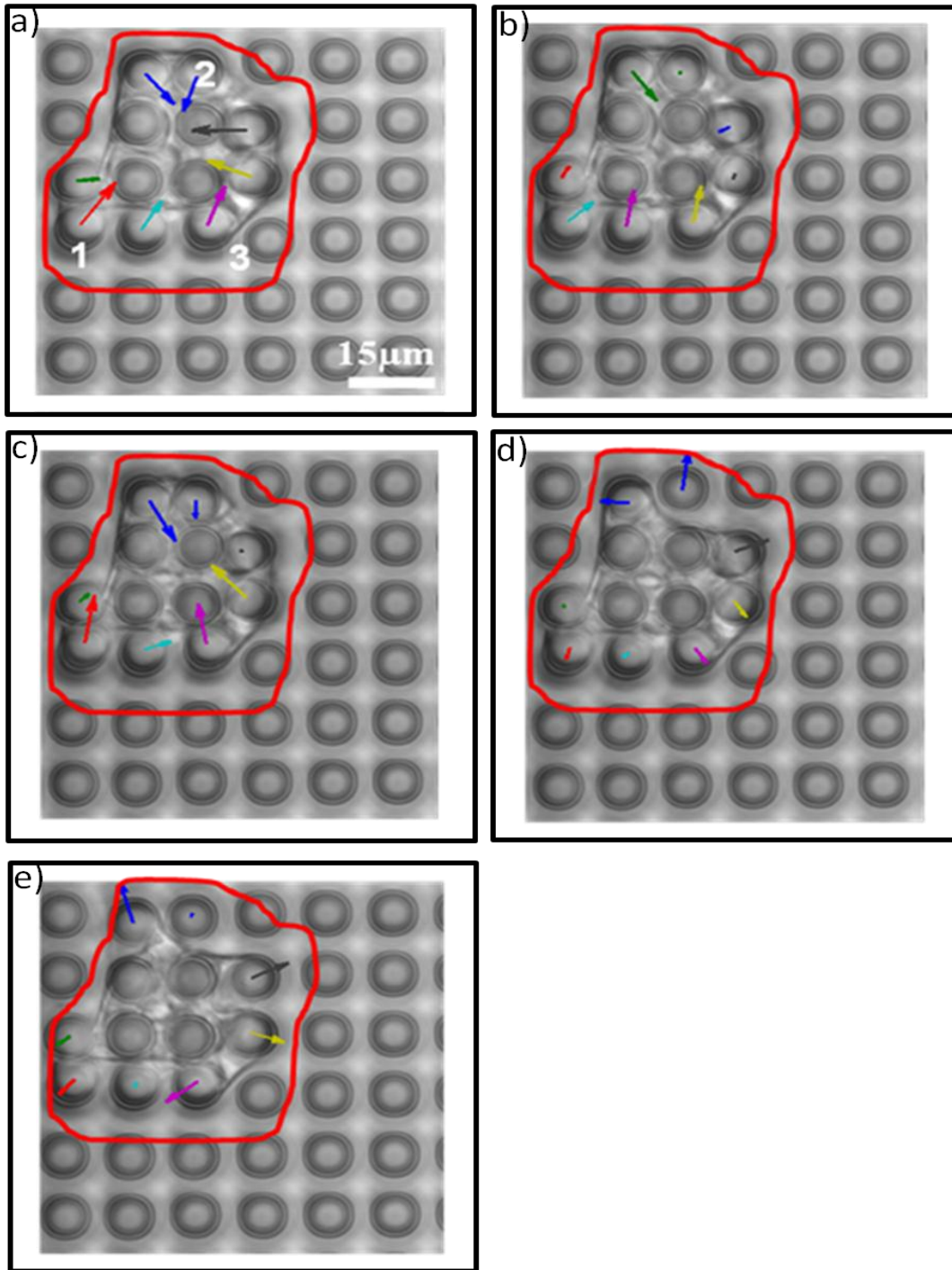


Figure 5.16. White field optical images of single CK4 cell: a) before adding ANGII and b) 3 minutes after adding ANGII c) 6 minutes after adding ANGII and d) 20 minutes after adding ANGII and e) 30 minutes after adding CYTO

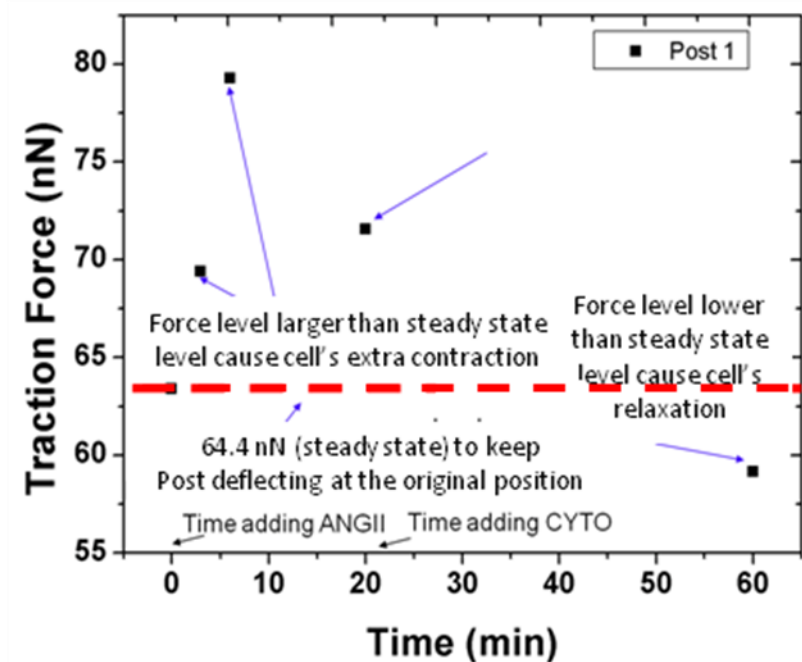


Figure 5. 17. The traction force of CK4 cell applied on post 1 (Figure 5.16.a) as a function of observation time

Figure 5-17 shows the traction force of CK₄ cell applied on micropost 1 as a function of observation time. The force applied to the micropost right before adding ANGII (63.4 nN) is named the control, steady state level. The contraction occurred when the traction force applied at that time is larger than the balanced level and relaxation occurred when the force level is lower than the steady state level. The exact experiment has been repeated by eight VSMCs. The similar dynamic change has been found. **Table 5.2** s shows the changes of traction forces of 3 microposts labeled in **Figure 5.16a**.

B. STUDY OF ILK CELL

The effects of Integrin-linked kinase (ILK), a serine/ threonine protein kinase implicated in signaling pathways involved in VSMCs proliferation and migration are analyzed by measuring

the traction forces exerted by VSMCs on the microposts. The VSMC without ILK was studied extensively using the PDMS micropost array. The experiments performed on CK₄ cells act as a control group. The exact same experiment is also performed on ILK cells to find if there is different reaction from ILK cell to the same external stimulus. The same geometry micropost array is used in the experiment. The diameter, height and spacing of the microposts are 3 or 5 μm , 25 μm and 5 or 7 μm , respectively.

Figure 5.18 shows the ILK cell growing on the micropost array with the geometries mentioned above. The average deflections of the microposts at the edge of the ILK cell are 3.18 μm and 3.38 μm for micropost with diameter, and height of 3 μm , 25 μm , and 5 μm , 25 μm , respectively, (See **Figure 5.18**). The corresponding average traction forces are 3.34 nN and 27.48 nN, respectively. It should be noted that the arrows' length in **Figure 5.16a** and **Figure 5.18a** has been magnified 8 times to make the arrows long enough to be seen. The same experiment is repeated 6 times to verify the repeatability. **Table 5.3** shows the results of average deflection of the microposts and the corresponding traction force generated by CK4 and ILK cells. The results demonstrate that CK4 cells and ILK cells tend to exert larger traction force when they grow on stiffer micropost array.

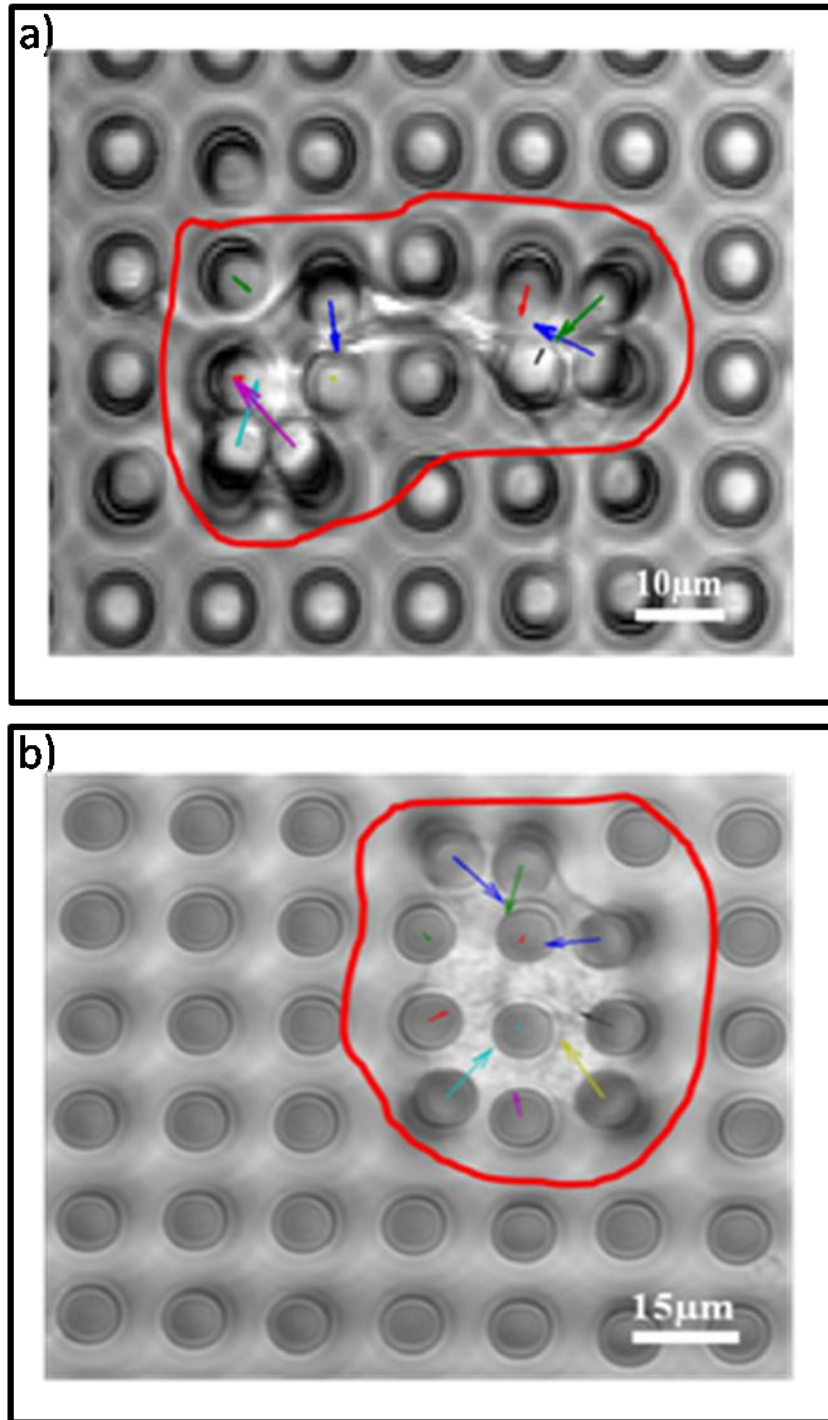


Figure 5.18. Wide-field optical images of single ILK cell growing on micropost array with a) 3 μm in diameter, 25 μm in height and b) 5 μm in diameter, 25 μm in height, respectively. The arrow's length in figure 7a is magnified 8 times to make it long enough to be seen

However, the traction forces generated by CK₄ are more than 80% larger than that generated by ILK cells when the same size of micropost array is used. It is partially demonstrates that the ILK molecule controls the amount of the traction force generated.

Table 5.3 Average deflection of the micropost and corresponding traction force generated by cells on micropost array

VSM Cells	Post diameter and height 3 μm , 25 μm				Post diameter and height 5 μm , 25 μm			
	D (μm)		F (nN)		D (μm)		F (nN)	
	C	I	C	I	C	I	C	I
1	7.00	3.18	7.35	3.34	4.31	3.38	34.95	27.48
2	7.03	4.27	7.38	4.48	4.72	3.71	38.28	30.09
3	7.56	4.45	7.94	4.67	6.12	3.76	49.64	30.49
4	7.61	4.86	7.99	5.10	6.70	3.83	54.34	31.06
5	7.62	5.03	8.00	5.28	7.94	4.24	64.4	34.39
6	8.87	5.24	9.31	5.50	8.04	4.58	65.2	37.14

D is the deflection of the micropost, F is the traction force applied on micropost. C represents the CK₄ cell and I represents ILK cell

Similarly, the dynamic change and traction force distribution map of a single ILK cell after adding ANG II and CYTO are shown in **Figure 5.19**. The optical image recorded right before adding ANGII (**Figure 5.19a**) shows that ILK cell generates a steady state traction force on the micropost array. The images recorded 3 minutes, 6 minutes and 20 minutes after adding ANGII (**Figure 5.19b to 5.19d**), and 40 minutes after adding CYTO (**Figure 5.19e**). Micropost labeled by 1 (in **Figure 5.19a**) shows the deflection equivalent to a traction force of 15.32 nN (before adding ANGII). This force has decreased to 12.37 nN (3 minutes after adding ANGII), to

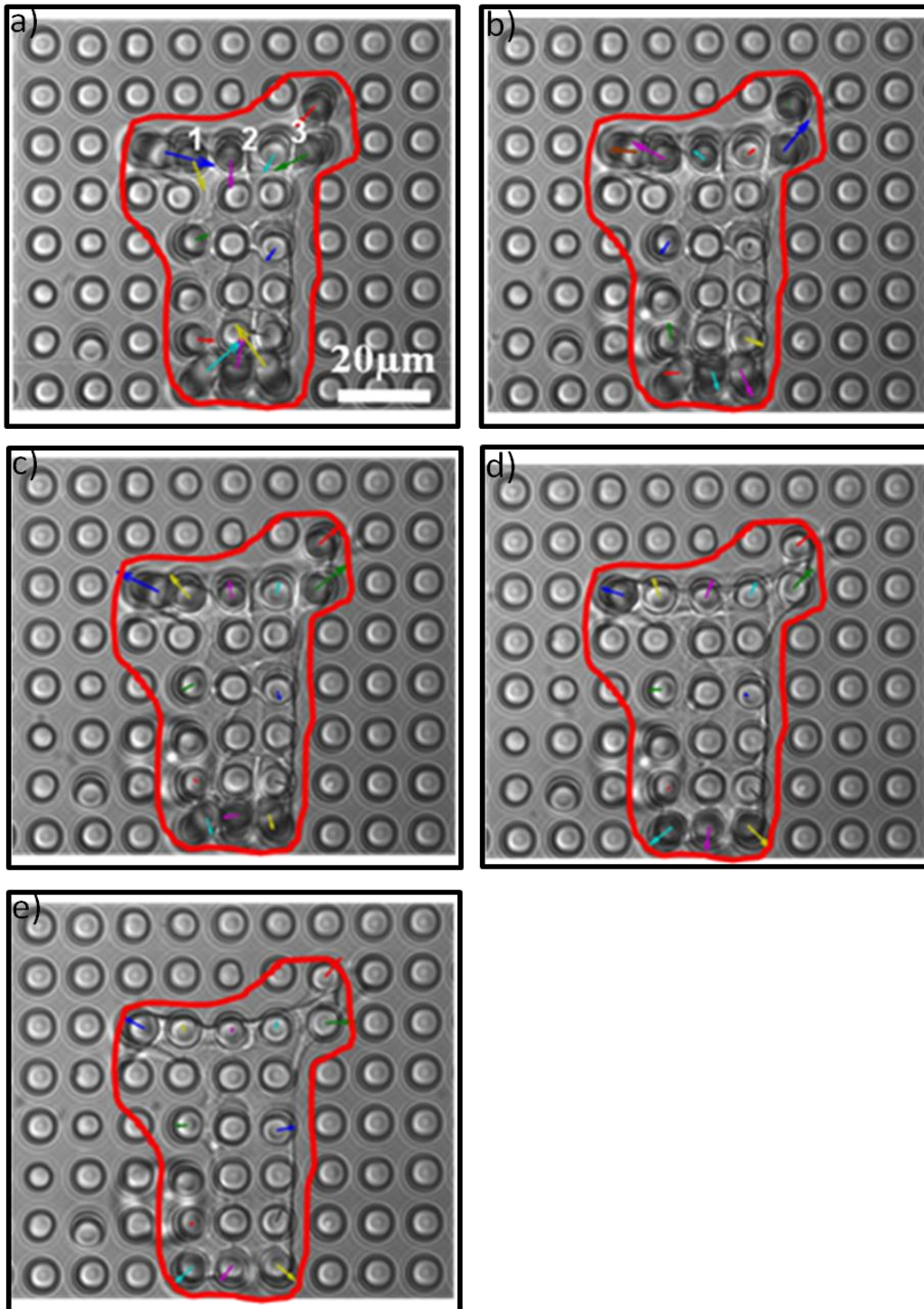


Figure 5.19. Wide-field optical images of single ILK cell: : a) before adding ANGII and b) 3 minutes after adding ANGII c) 6 minutes after adding ANGII and d) 20 minutes after adding ANGII and e) 30 minutes after adding CYTO

10.86 nN (6 minutes after adding ANGII), and 9.28 nN (20 min after adding ANGII). The results show that ANGII does not lead to contraction in ILK cell. Instead, the cell exhibits a relaxation during the experiment. The relaxation is pronounced at 15 minutes after adding the CYTO to CK₄ cell and it can last around 30 minutes.

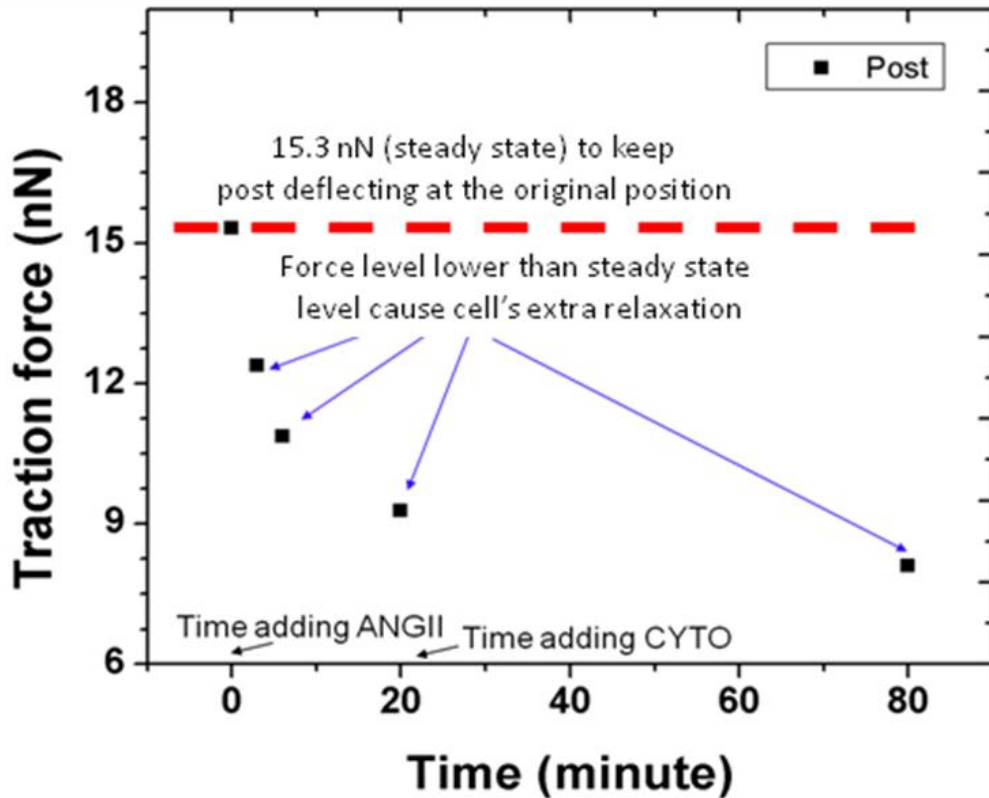


Figure 5.20. The traction force of ILK cell applied on post 1 (Figure 5.19.a) as a function of observation time

Figure 5.20 shows the traction force of ILK cell applied on micropost 1 as a function of observation time. **Figure 5.20** shows the traction force of ILK cell applied on micropost 1 as a function of observation time. The force applied to the micropost right before adding ANGII (12.39 nN) is named the balanced level. Relaxation occurred all the time since the force levels are lower than the balanced level. **Table 5.4** shows the changes of traction forces of 3 microposts

labeled in **Figure 5.19a**. The experiment was repeated on 6 ILK cells. The results show similar dynamic mechanism. It should be noted that there was no excessive contraction found all through the dynamic study of ILK cells. The strong relationship between ILK and the contraction function of VSMC can be predicted.

Table 5.4 Traction force from the labeled posts as a function of observation time for ILK cell

Post	Before experiment (nN)	ANGII 3min (nN)	ANGII 6min (nN)	ANGII 20min (nN)	CYTO 40min (nN)
1	15.32	12.39	10.86	9.28	8.1
2	11.37	10.58	9.27	8.5	7.32
3	6.70	5.97	5.37	4.85	4.08

5.3 CONCLUSION

The preparations of culturing and growing VSMCs on PDMS micropost array were optimized. The oxygen plasma is used to treat the top surface of the micropost and made it adhesive which enabled cells to grow on it easily. Due to the high aspect ratio of the micropost used, the smallest spring constant of is $1.05\text{nN}/\mu\text{m}$ and the corresponding minimum detectable traction force is 0.21nN . Different methodologies are used to extract the outline of micropost from top and bottom images. Matlab and its image processing function are used to fill outlines of the microposts with white and determine their center position. The CK4 cells and ILK cells have

been successfully grown on microposts array with two different geometries. It is found that both cells tend to exert large traction force when growing on stiffer micropost array. This phenomenon is found in both CK4 cell and ILK cell. By comparing these two types of VSMCs using the micropost arrays with the same size, it is observed that CK4 cells generate larger average traction force than ILK cells when both of them grow in normal media solution. It is also found that ILK cells lose the ability of excessive contraction in response to angiotensin II which is found in CK4 cells during the dynamic study. This demonstrates that ILK is important for the ability of the VSMC to contract in response to angiotensin II and it has a significant role in controlling cell's traction force.

6. TRANSIENT RESPONSE STUDY OF VSMC USING MICRIPOST ARRAY

In this chapter, the transient response of VSMCs in normal situation and to external stimulus such as Angiotensin II and Cytochalasin D will be observed and studied with higher temporal resolution. Due to the high sensitivity of the micropost as a force sensor, the force changes of the cell exerted in real time can be recorded by high speed measurement of micropost deflection. The results demonstrate an oscillating pattern which will provide an additional tool to prove that specific mechanism different from ILK molecule controls the mechanical behavior of the VSMC cell. In addition, the dynamic responses from a single smooth muscle cell at different locations will be compared. The results demonstrated that the transient behaviors of VSMC at different locations are not independent. The strong relationship of transient behaviors between adjacent locations in a single VSMC is found.

The confocal microscope is used to focus on the top plane of the microposts. The scanning rate is increased to record more information during a short period of time. The transient responses of the VSMC are converted to the position changes of the micropost top end. In order to capture the position changes in relatively short time, high aspect ratio micropost array is used. Such micropost offers high sensitivity which guarantees measurements of very small forces in hundreds of pico Newton range.

6.1 EXPERIMENT PREPARATION AND DESIGN

The PDMS micropost array used in cell's dynamic response study should have appropriate flexibility. It should have very high force measurement sensitivity which makes it

good to capture the tiny changes from the cell in a short period. At the same time, the micropost should keep the force measurement within the linear range to guarantee the measurement accuracy. Based on those requirements, we have used microposts with the diameter, height and spacing of 3 μm , 25 μm and 5 μm , respectively.

The preparation of the VSMC is described in chapter 5. Oxygen plasma is used to treat the micropost's top surface. The device is exposed to UV light for 30 minutes for sterilization. VSMC is then placed on the top of the micropost array and kept growing for 2 days before scanning it by confocal microscope. The cell is then placed on the testing stage. The confocal microscope with 60X water objective is used to observe the changes of the deflection. The micropost used in the experiment matches the following three requirements:

1. The micropost should be covered by part of the vascular smooth muscles cell. The cell should not touch the sidewall of the micropost or grow on the substrate but grow on the top of the micropost.
2. Although the deflection of the micropost should be noticeable, it should be within the linear bending region of the micropost. Otherwise, the micropost cannot recover to its original position or cannot bend towards other directions properly when external stimulus or micro-oscillation occurs.
3. Each micropost should not be touched by adjacent microposts. Otherwise, the deflection change is influenced by the movement of other micropost. If the micropost itself is not independent, it cannot be used to test the independent property of VSMC.

Figure 6.1 shows the optical micrograph of one VSMC grown on the micropost array with the diameter, height and spacing of 3 μm , 25 μm and 5 μm , respectively. The micropost labeled as ‘1’ match the requirements mentioned above. Its top surface was magnified and the deflection changes are recorded and analyzed to extract the characteristics of the dynamic response of VSMC.

Table 6.1 Experiment description of cell's transient response study

Experiment	Specification	Objective
Observe microposts – CK ₄ interface, capture image continuously	<ul style="list-style-type: none"> • Last 30 minutes • Sampling frequency: 96 and 48 seconds/frame 	Find transient response of CK ₄
Observe microposts – CK ₄ interface, capture image continuously after adding ANGII	<ul style="list-style-type: none"> • Add ANGII (10⁻⁵ mol/l) • Last 20 minutes • Sampling frequency: 96 and 48 seconds/frame 	Find transient response of CK ₄
Observe microposts – CK ₄ interface, capture image continuously after adding CYTO	<ul style="list-style-type: none"> • Add CYTO (10⁻⁷ mol/l) • Last 20 minutes • Sampling frequency: 96 and 48 seconds/frame 	Find transient response of CK ₄

Table 6.1 shows the experiments designed to study the transient response of VSMC. In the first section of the experiment, the micropost ‘1’ will be magnified and observed at its top continuously for 30 minutes. The micropost will be scanned every 8 seconds. Its center position will be measured and calculated with the interval of every 6 images and every 12 images, respectively. That means the micropost’s position change will be sampled every 48 seconds and every 96 seconds, respectively. The dynamic changes during this period will be analyzed and discussed. In the second section of the experiment, Angiotensin II is added to the cell with the

density of 10^{-5} mol/ml. Similarly, the micropost '1' will be magnified and observed at its top continuously for 20 minutes. It will be scanned every 8 seconds. Its center position will be measured and calculated with the interval of every 6 images and every 12 images, respectively. That means the micropost's position change will be sampled every 48 seconds and every 96 seconds, respectively. The dynamic change of the micropost during this period will be analyzed and discussed. In the third section, Cytochalasin will be added to the cell with the density of 10^{-7} mol/ml. The micropost '1' will be magnified and observed at its top continuously for 20 minutes. It will be scanned every 8 seconds. The center position will be measured and calculated with the interval of every 6 images and every 12 images. That means the micropost's position change will be sampled every 48 seconds and every 96 seconds. The dynamic change during this period will be analyzed and discussed. Finally, the difference of transient response from VSMC will be

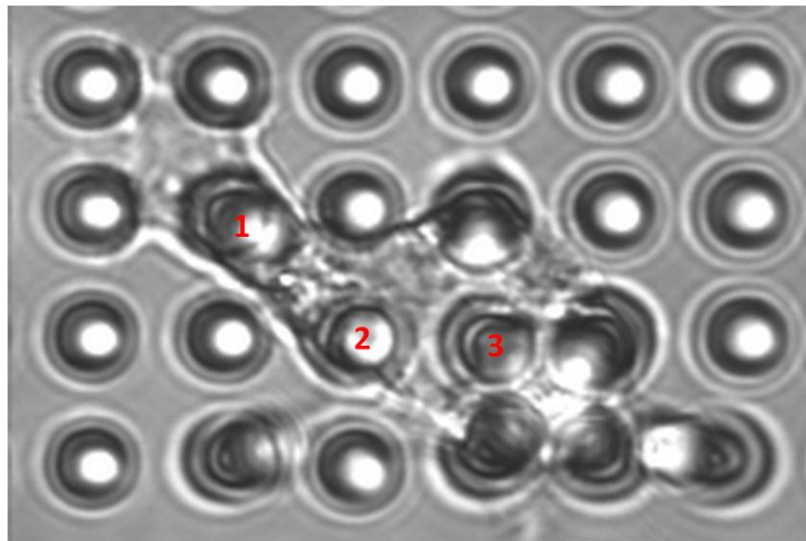


Figure 6.1 Optical micrograph of a VSMC grown on micropost array compared between normal conditions and under external stimulus.

6.2 TRANSIENT RESPONSE OF VASCULAR SMOOTH MUSCLE CELL IN NORMAL CONDITION

In order to simplify the analysis, the position change of the micropost is divided into two sections: first is along the X-axis and the other is along the Y-axis. Initially, its position is marked as (0, 0) and the position changes is tracked for 30 minutes. **Figure 6.2** shows the position change along X-axis for 30 minutes with sampling interval of 96 seconds. It should be noted that a regular vibration period is found. The vibration period is around 900 seconds. The

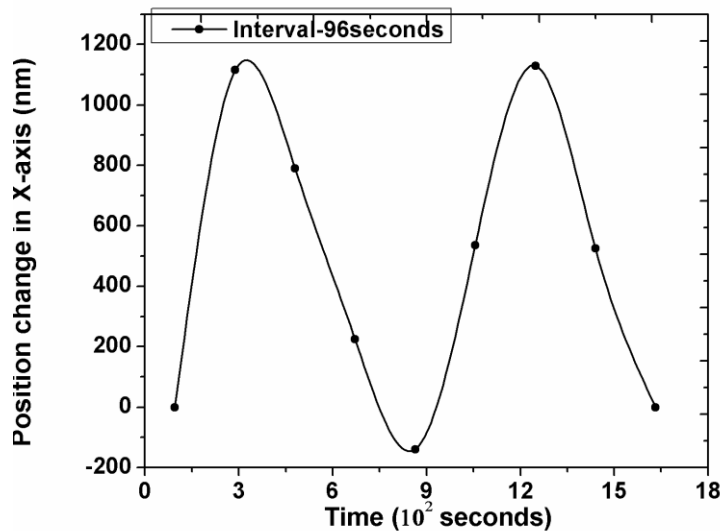


Figure 6.2 Transient response with sampling interval of 96 seconds

vibration amplitude ranges from 140 nm to 1150 nm. Since the micropost spring constant is $1.051 \text{ nN}/\mu\text{m}$, the change of traction force along X-axis is from 140 pN to 1.209 nN.

We have reduced the sampling interval from 96 seconds to 48 seconds and plotted the transient response of the cell in **Figure 6.3**. The amplitude of the transient response along X-axis is changed to the range of (-450 nm to 1400 nm). It clearly shows the plot profile is changed as

the sampling interval is reduced. This change is due to the reduced sampling interval (from 96 seconds to 48 seconds). It enabled the detection of oscillation in VSMC with higher frequency. The curve profile in **Figure 6.3** is the superposition of the 900-second component and an oscillation with a higher frequency. **Figure 6.4** shows the comparison of plots with 48 seconds

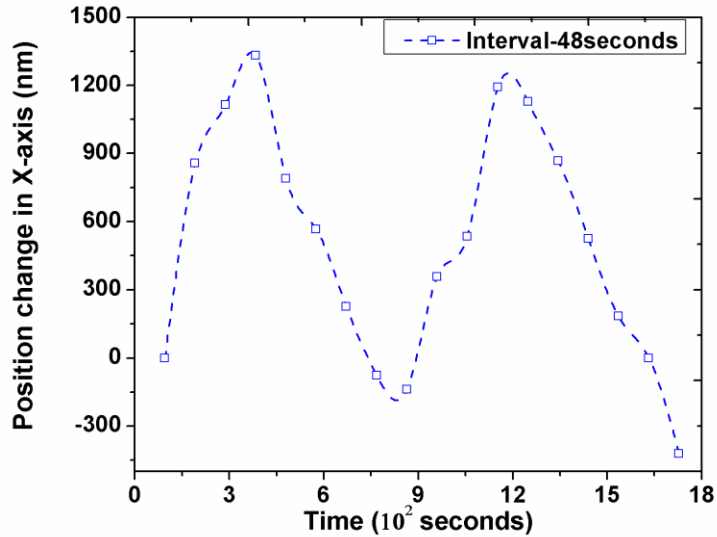


Figure 6.3 Transient response with sampling interval of 48 seconds

and 96 seconds interval, respectively.

The frequency of the fast oscillation in VSMC is extracted by analyzing the difference between **Figure 6.3** and **Figure 6.2**. It is plotted in **Figure 6.5**. The period of fast vibration is around 500 seconds. The vibration amplitude ranges from only 100 nm to more than 300 nm which is much smaller than that of the slow oscillation

The analysis clearly shows that vascular smooth muscle cell exhibits an oscillation in the

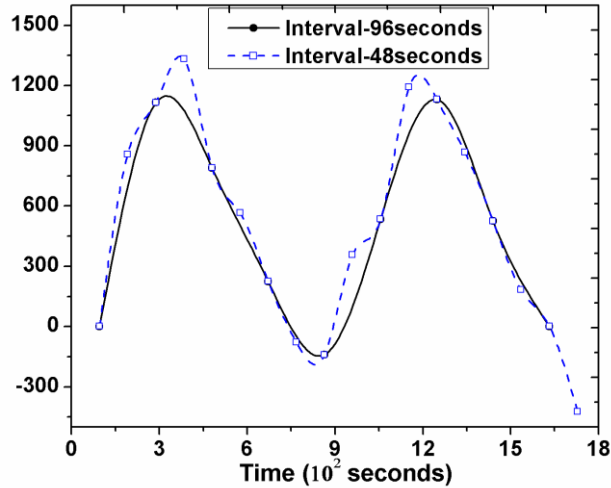


Figure 6.4. Transient response with sampling interval of 48 and 96

amplitude. The oscillation periods are usually less than 10 minutes. The force changes during such transient vibration ranges within several hundred pico Newton to several nano Newton.

The similar trend has also been found in the analysis of transient response along the Y-axis. **Figure 6.6** shows the position change of post 1 in Y-axis with sampling interval of 45 secs and 96 seconds, respectively. The first oscillation period can be extract from **Figure 6.6**. The

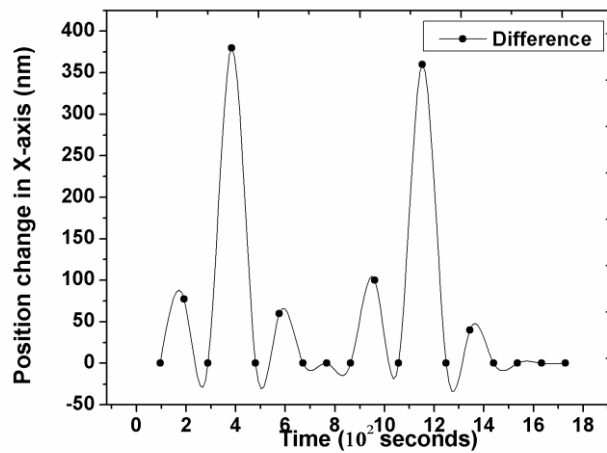


Figure 6.5. Transient response with different period

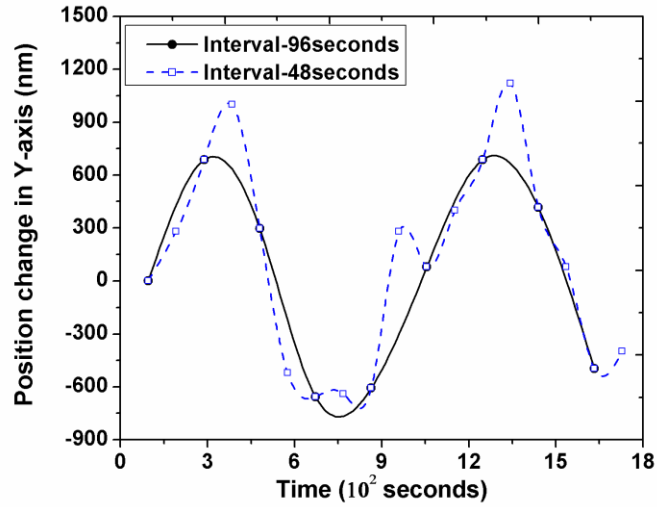


Figure 6.6 transient responses with different sampling interval

period is 950 seconds which is similar to that along the X-axis. The difference of the two plots indicates that the oscillation consists of different period components. It can be extract by comparing the two plots with different sampling interval. **Figure 6.7** shows the transient oscillation of the vascular smooth muscle along the Y-axis. The oscillation has the period of 450 seconds which is also similar to that along the X-axis.

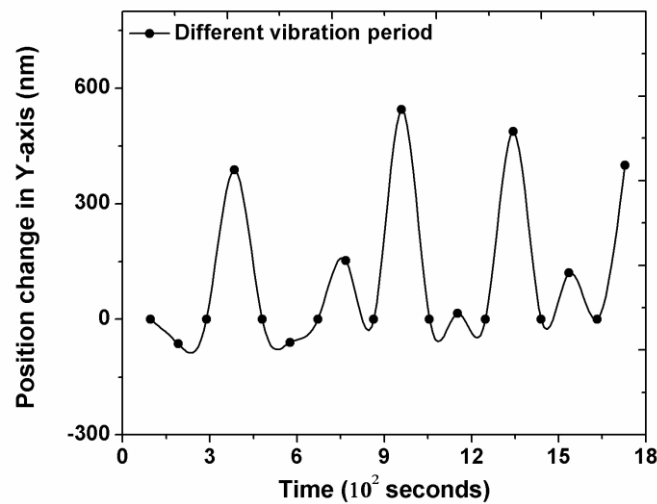


Figure 6.7 Transient response with different vibration period

6.3 TRANSIENT RESPONSE OF VASCULAR SMOOTH MUSCLE CELL UNDER STIMULUS OF ANGIOTENSIN II

After observing the VSMC in normal condition for 30 minutes, ANGIOTENSIN II (10^{-5} mol/ml) is added to the cell as external stimulus. The micropost '1' is scanned by the confocal microscope and the images are continuously recorded every 8 seconds for 20 minutes. Similarly, they are sampled every 6 and 12 images to extract the information of transient response of VSMC. The

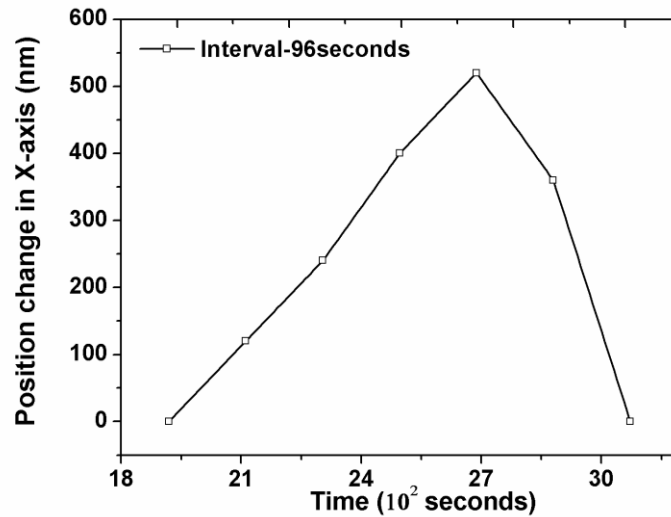


Figure 6.8 Transient response with 96 seconds sampling interval

displacement change of the micropost is first divided to the section along X-axis and Y-axis. **Figure 6.8** and **Figure 6.9** show the displacement change along X-axis with 48 seconds and 96 seconds sampling intervals respectively, within 20 minutes after adding ANGIOTENSIN II to the VSMC. The plot in **Figure 6.10** shows only one period which lasts 20 minutes. It demonstrates that adding ANGIOTENSIN II may make the longest period of natural transient response even longer. However, the plot with 48 seconds sampling interval shows a different oscillating period which is around

450 seconds to 500 seconds. This oscillation frequency is similar to that under normal conditions.

Figure 6.11 shows the extracted vibrating period with higher frequency.

The similar analysis has been performed for the displacement along the Y-axis. **Figure**

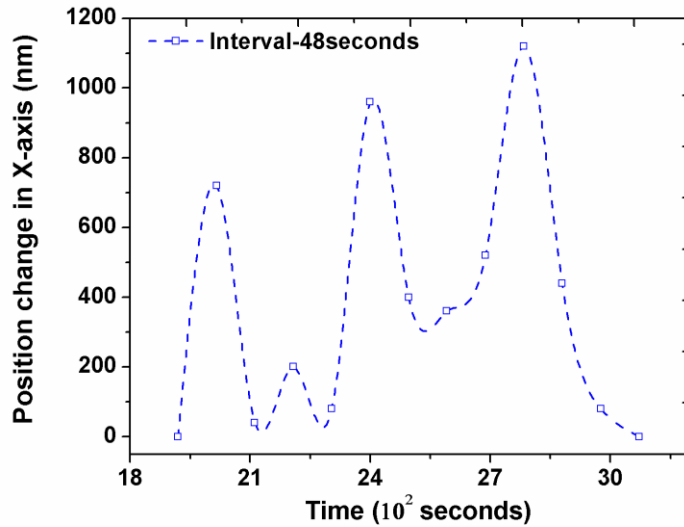


Figure 6.9 Transient response with 48 seconds sampling interval

6.12 shows the changes of the transient deflection generated by the micropost '1' with the sampling interval of 96 seconds. Only one period is found during the 20 minutes observation. The result is consistent with that along the X-axis. The transient response as a function of time is shown in **Figure 6.11**. A higher oscillation component is added to the profile and plotted in **Figure 6.12**. The period of faster oscillation is 400 seconds. This higher oscillation frequency component is extracted and is shown in **Figure 6.13**.

Based on the analysis of transient deflection change of the micropost along the X-axis and Y-axis, the following conclusion is obtained: The external stimulus of ANGII to the VSMC

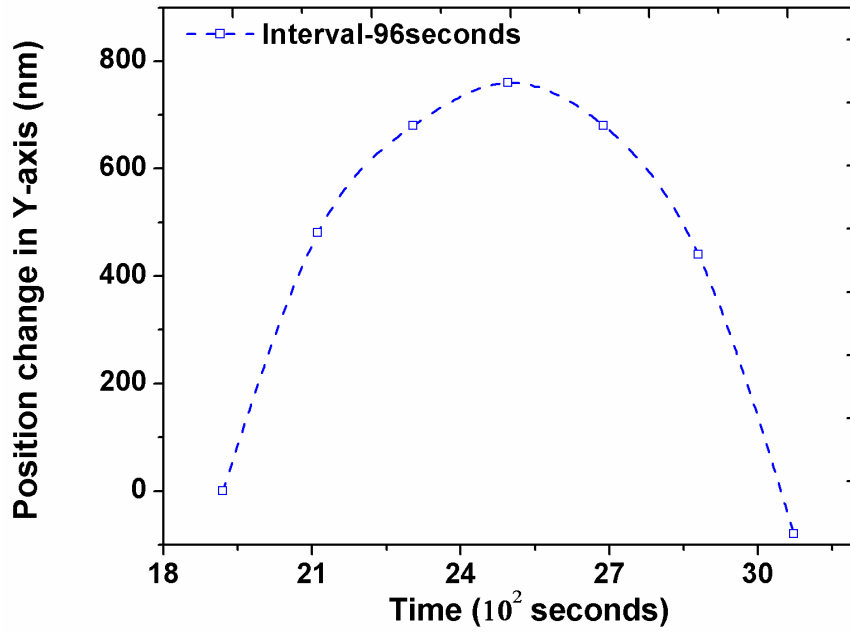


Figure 6.10 Transient response with 96 second sampling interval

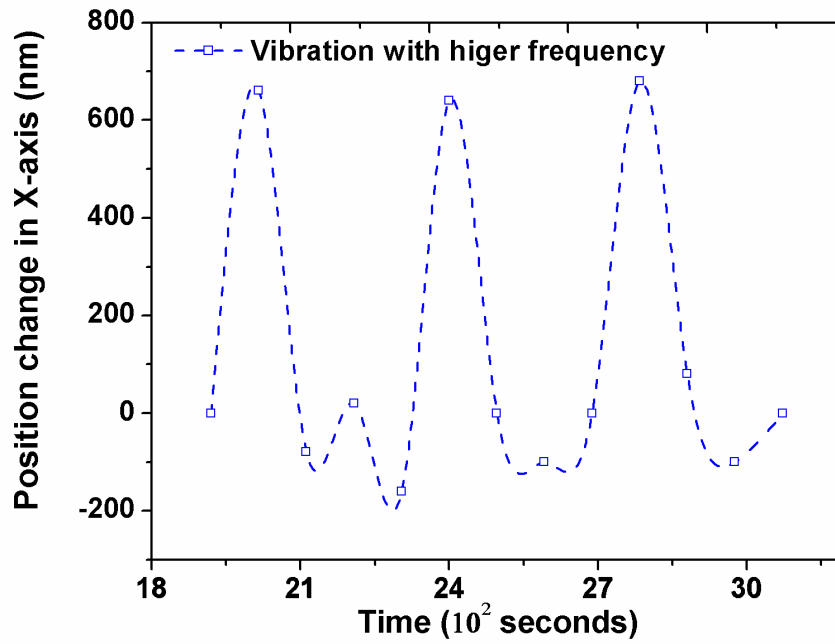


Figure 6.11 Transient response with higher vibrating frequency

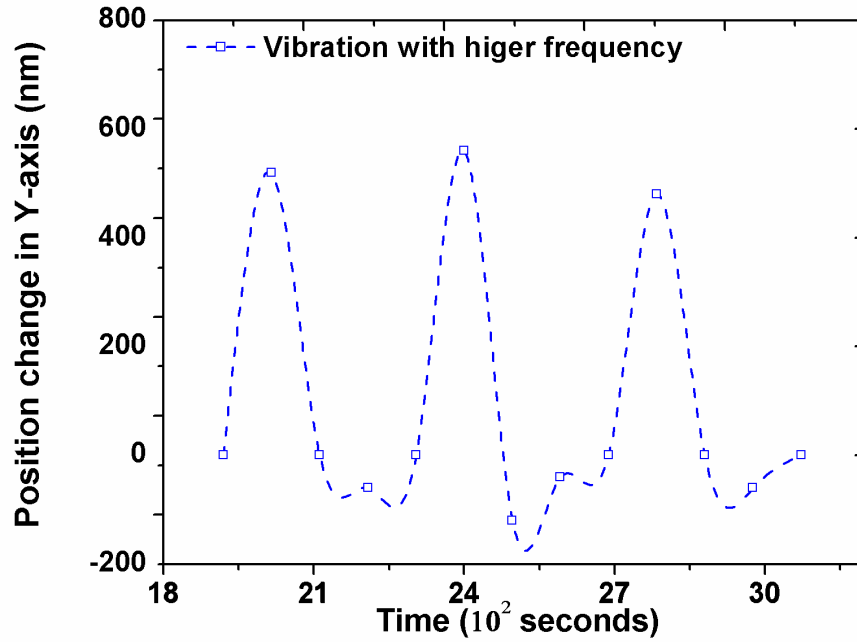


Figure 6.4 Transient response with higher vibrating frequency

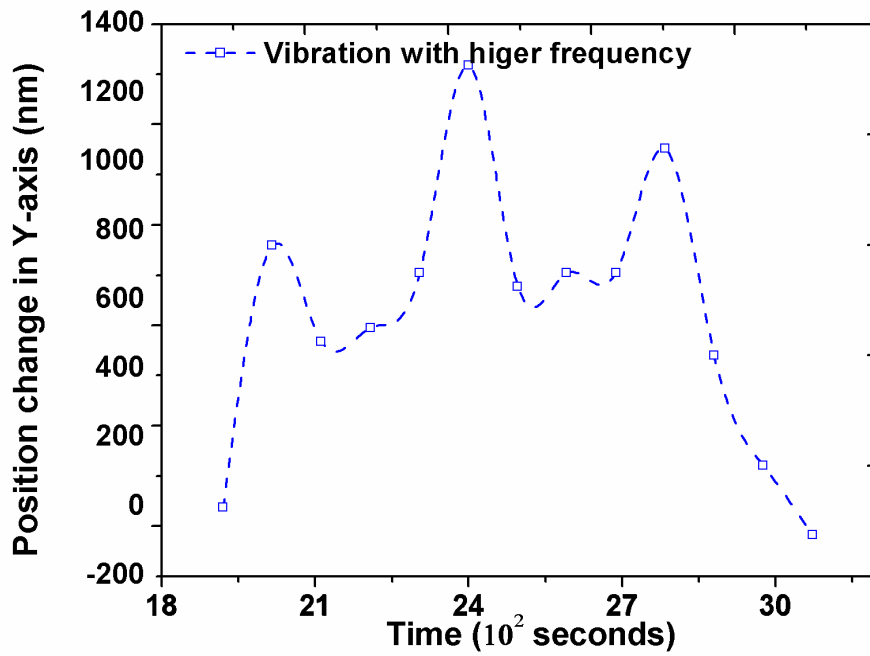


Figure 6.5 Transient response with 48 second sampling interval

extends the time span of oscillation with the long period. The period is prolonged from 900 seconds to 1200 seconds.

1. The external stimulus of ANGII does not reduce the period of the VSMC with higher oscillation frequency. Such oscillation with a period of around 350 seconds is strengthened.

6.4 TRANSIENT RESPONSE OF VASCULAR SMOOTH MUSCLE CELL UNDER STIMULUS OF CYTOCHALASIN

In the last part of the transient analysis, a certain amount of Cytochalasin D (10^{-7} mol/ml) has been added to the cell as external stimulus. The micropost '1' is scanned by the confocal microscope and the images are continuously recorded every 8 seconds for 40 minutes. They are sampled every 6 and 12 images to extract the information of transient response from VSMC. The transient displacement changes of the VSMC are first divided to the sections along X-axis and Y-axis. **Figure 6.14** shows the displacement change along X-axis with 96 seconds

It should be noted that the oscillation has a long period which lasts more than 30 minutes. At the same time, the vibration of the VSMC after adding CYTO has larger amplitude than those in the other sections of the experiment. The change of the deflection of the micropost ranges between 800 nm and more than 1200 nm. When the sampling time interval is reduced to 48 seconds, another oscillation component is appeared and the superposition of such two components

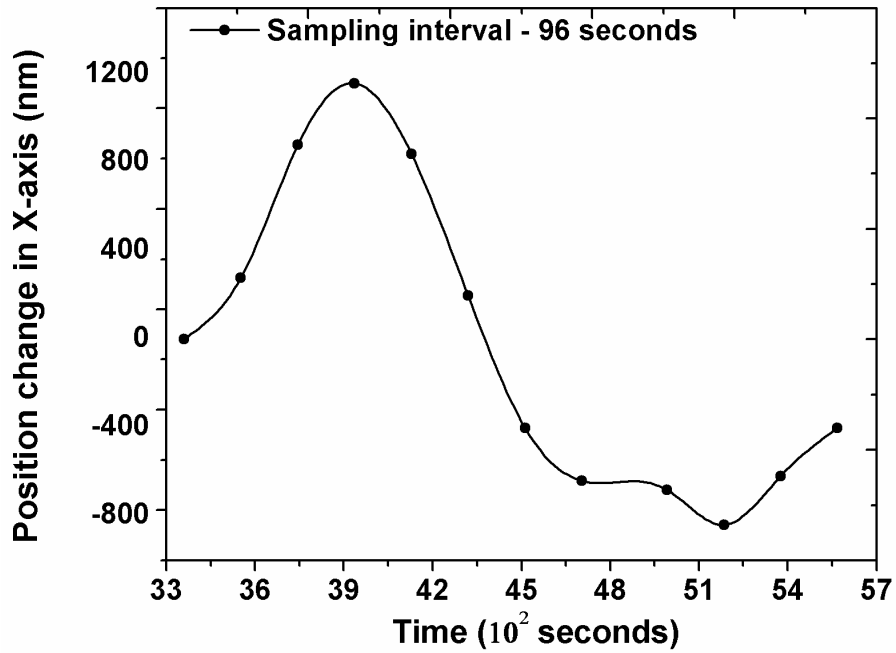


Figure 6.14 Transient response with 96 seconds sampling interval

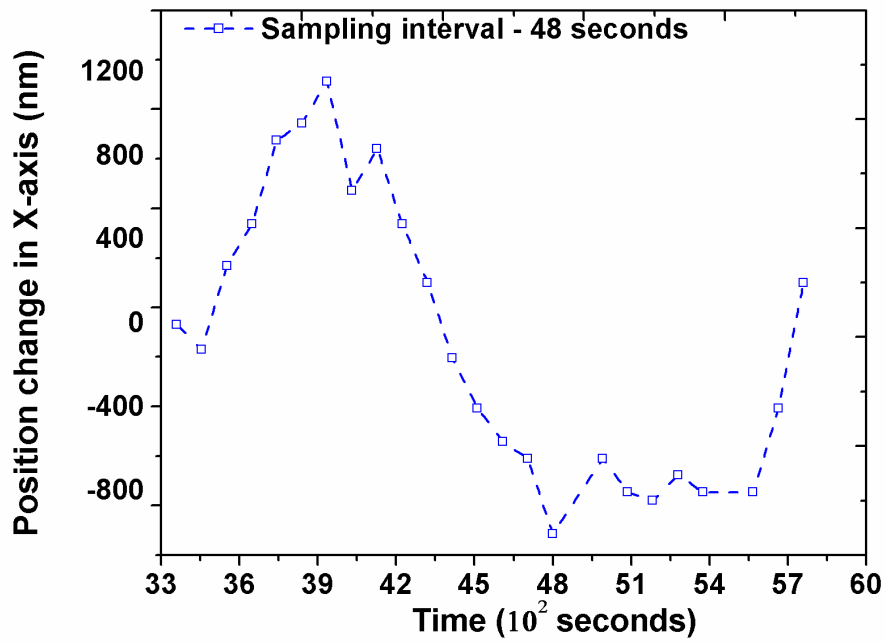


Figure 6.15 Transient response with 48 seconds sampling interval

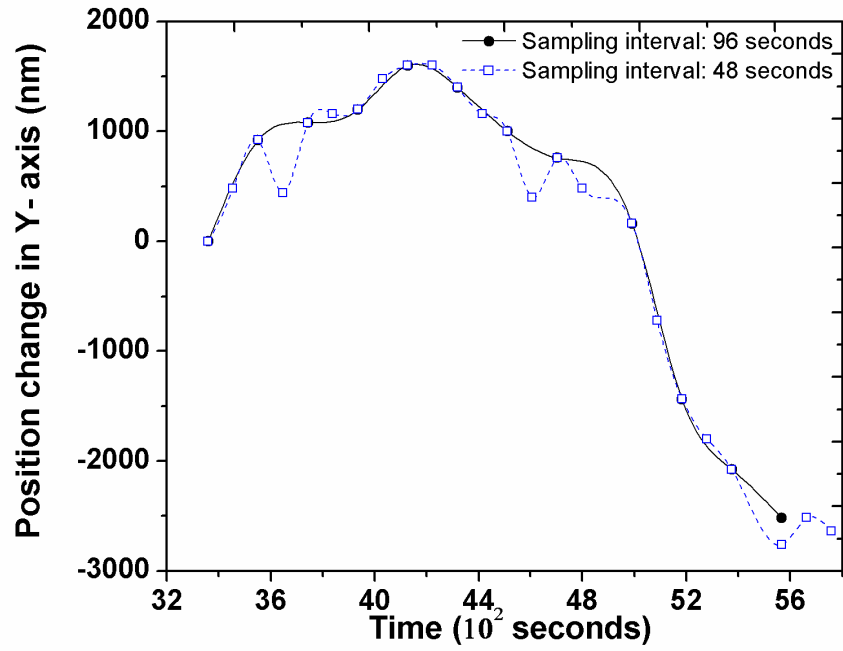


Figure 6.7 Transient response with sampling interval of 48 seconds and 96 seconds

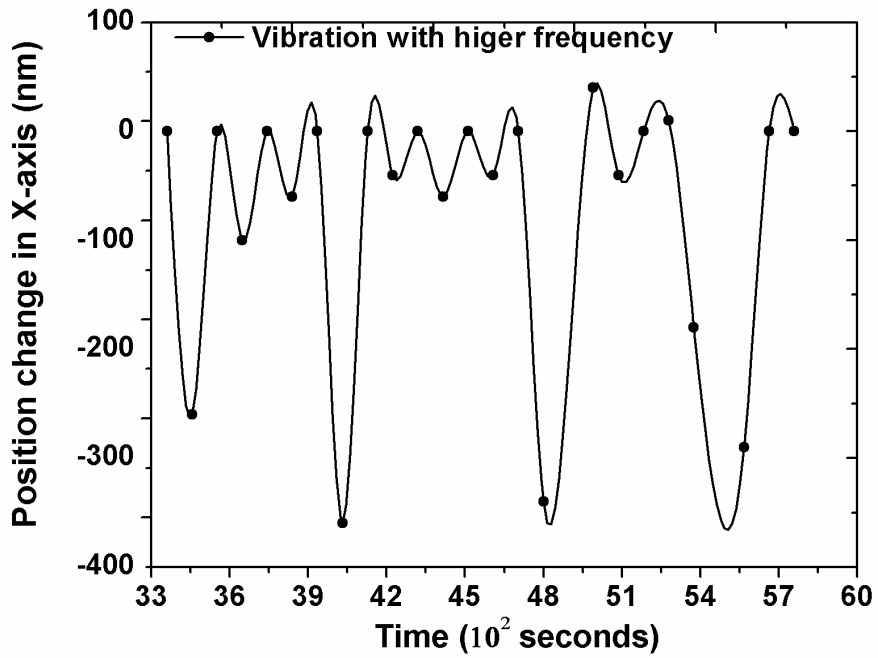


Figure 6.6 Transient response with higher vibrating frequency

is different from **Figure 6.14**. The oscillation with higher frequency is extracted by taking the deflection difference between the plots made by sampling with 96 seconds and 48 seconds,

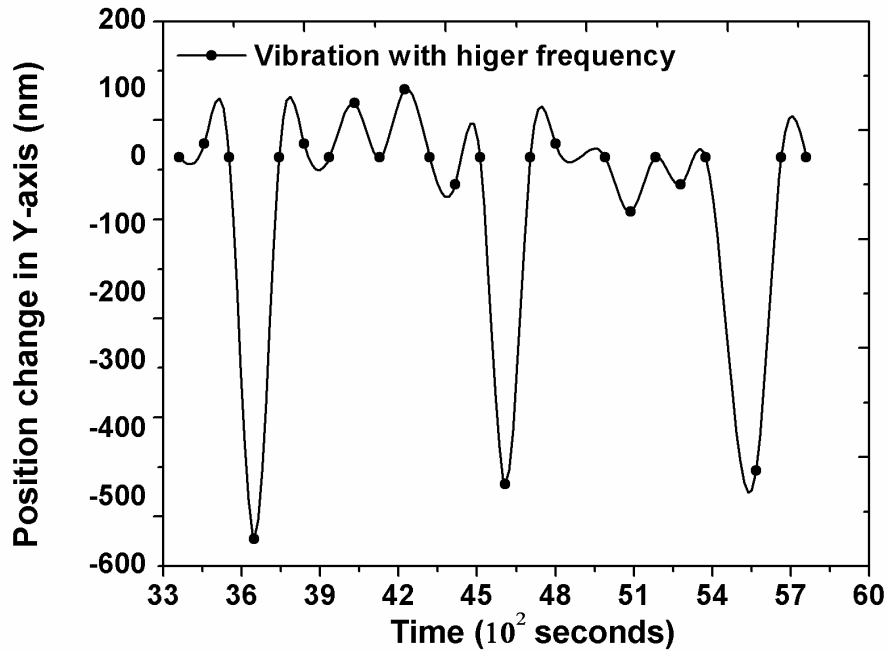


Figure 6.8 Transient response with high vibration frequency

respectively (see **Figure 6.16**). The period of oscillation is between 650 – 750 seconds.

The transient oscillation of micropost ‘1’ along Y-axis is also analyzed by using sampling interval of 96 seconds and 48 seconds. The trend is plotted in **Figure 6.17**. The profile made by sampling interval of 48 seconds includes different frequency components. The high frequency components are extracted and plotted in **Figure 6.18**. Similar to the previous results, the vibration stimulus of CYTO the vibration amplitude increased significantly. The period of faster vibration is 1000 seconds.

6.5 TRANSIENT RESPONSE OF A SINGLE VASCULAR SMOOTH MUSCLE CELL AT MULTI-LOCATIONS

The same method is used to analyze the deflection change of the microposts labeled as '2' and '3' in **Figure 6.1**. In normal conditions, the three microposts reflect regular force changes with periods around 600 seconds to 750 seconds. For example, both micropost 2 and micropost 3 have three constant periods during the first 30 minutes observation. Two regular periods are found on micropost 1 during the time when the VSMC was in resting. A shorter oscillation

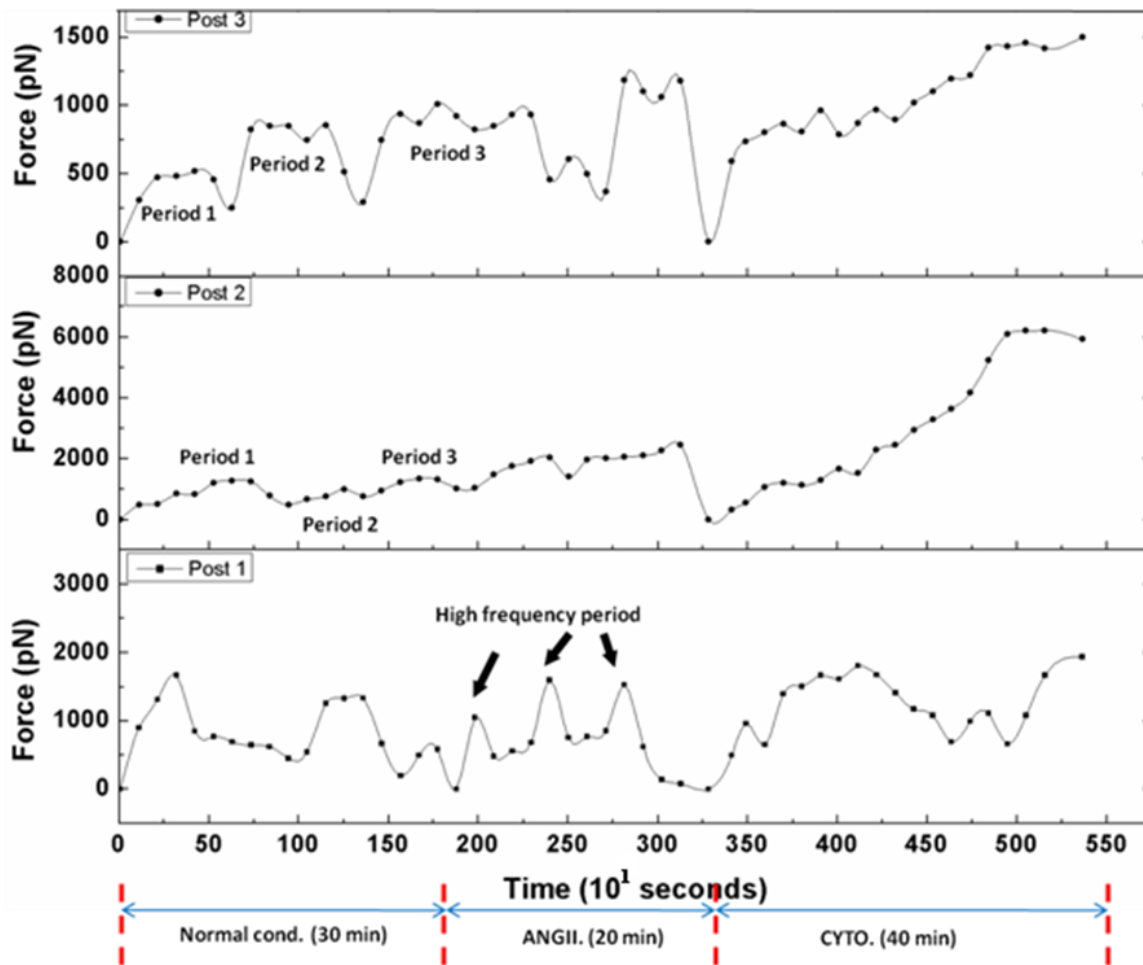


Figure 6.19 Transient force change reflected by post 1 to 3

period is found on micropost 1 when adding ANG II. The period is around 350 seconds. The other two microposts reflect no large change of the transient changes of force. After adding CYTO, the regular changes of the force which are found in the previous two time periods are disappeared. The amplitude of the force changes increases significantly in this period. The plot of micropost 1 in **Figure 6.19** also indicates that the traction force generated in the area where micropost 1 is attached to the VSMC is increased initially right after adding ANGII which indicates that the VSMC tends to make extra contract. The traction force tends to reduce after a certain period of time. This trend is consistent with what we have found during the steady state experiment. However, the plots of micropost 2 and 3 in **Fig. 6.19** indicate that the traction forces generated in those areas keep on increasing which means the cell in those locations tends to make extra contract during the whole period. The results demonstrate that the reactions of a single cell at different locations are not same.

The transient change of forces on these three microposts may have close relationship between each other. For example, the curve profile of micropost 2 and micropost 3 in Fig. 6.19 are similar. Moreover, the independent feature of micropost 1 to 3 offers a great opportunity to analyze such relation. The calculated correlation coefficient of transient changes of force between micropost 1 and 2; micropost 2 and 3; and micropost 1 and 3 are 0.29, 0.77 and 0.20, respectively. High correlation coefficient 0.77 between micropost 2 and 3 demonstrates that they has strong relation between each other. Micropost 1 is far away from micropost 2 and 3. The correlation coefficients 0.29 and 0.20 indicate that the transient changes of force of VSMC near micropost 1 are more independent to those locations near microposts 2 and 3.

6.6 CONCLUSIONS

The PDMS micropost array is used to detect generation of nanoscale forces and movements from the VSMC. There is dynamic behavior or response from the VSMC in normal conditions. Due to the high sensitivity of the micropost, the vibration as small as 200 nm, which is equivalent to 210 pN is detected. The vibration of the micropost consists of different frequency component.

Due to the external stimulus such as angiotensin II and Cytochalasin, the natural vibration frequency of the VSMC is changed. The vibration amplitude is also changed due to the reaction between cell and external stimulus. A close correlation of the transient changes of force was observed from microposts close to each other, but not from microposts away from each other, suggesting that the traction forces on adjacent microposts are similarly regulated.

7. SUMMARY AND CONCLUSION

7.1 HIGH ASPECT RATIO PDMS MICROPOST FORCE SENSOR ARRAY

Novel high aspect ratio PDMS micropost force sensor arrays are developed. The arrays are fabricated using MEMS fabrication technology and micromold replica technology. The micromold is prepared using deep reactive ion etching system that etches deep holes on a 4 inches silicon wafer. The PDMS is cured in the micromold and peeled off manually.

The high quality micropost array is accomplished by optimizing the fabrication process. The anisotropic etching of the deep reactive ion etching process is accomplished. The etch rate is 1.2 μm per cycle. The etching phase of each cycle is 7.5 seconds and the deposition phase is 2 seconds. The smallest feature in the patterned silicon wafer is the open circle with 3 μm diameter. The yield of the patterned Shipley 1813 or Shipley 1827 is more than 99%. The highest aspect ratio of fabricated micropost is 13 with the 3 μm wide and 35 μm high.

The accurate Young's modulus of the PDMS micropost is obtained and evaluated using AFM and Matlab. The calibrated samples are divided into 4 groups. During each comparison, there is only one different factor: curing temperature or micropost's size. The statistical evaluation of the influence of such factors on the Young's modulus of PDMS was performed by calculating the p-value of each comparison. It should be noticed that the p-value of any comparison is much less than 0.01. Therefore, the Young's modulus or the stiffness of the micropost is not only determined by the curing temperature but also determined by the size of the silicon micromold. There is also another assumption that the large size micropost may need more

time to cure to the same level as that of the small size micropost. It implies that the micromold size may affect the curing speed instead of PDMS micropost.

Finally, the Young's modulus of the micropost used in later biological experiment is determined. It is 1.38 MPa. The micropost with different diameter and height possessing such Young's modulus has a wide range of spring constant. The spring constant of the micropost is tuned from 487.7 nN/ μm to 0.257 nN/ μm when the diameter of the micropost changed from 3 μm to 10 μm and the height changed from 10 to 40 μm . Such flexible measurement sensitivity was not reported previously. It allows the PDMS micropost force sensor array to be applicable not only to the study of vascular smooth muscle cells which possess relatively large traction force but also to the study of cells with small force in pico Newton (pN) range.

7.2 THE STUDY OF LONG TERM MECHANICAL RESPONSE OF VSMC USING PDMS MICROPOST ARRAY

The growth of VSMCs on PDMS micropost array is optimized. The coating of specific protein to make PDMS micropost top surface sticky to cell is not necessary anymore. The oxygen plasma is used to treat micropost top surface and made it to become sticky to cells grown on it. Due to high aspect ratio, the smallest spring constant is 1.05 nN/ μm and the corresponding minimum detectable traction force is 0.21 nN.

The CK4 cells and ILK cells are successfully grown on microposts array with two different geometries. It is found that both cells tend to exert large traction force when grown on stiffer micropost array. This phenomenon is found both from CK₄ cell's and ILK cell's mechanical behavior. By comparing these two types of VSMCs using the micropost arrays with

the same size, it is observed that CK4 cells generate larger average traction force than ILK cells when both of them are grown in normal media solution. It is also found that ILK cells lose the ability of excessive vasoconstrict under the stimulus of angiogenesis II which was found in CK4 cells during the dynamic study. This demonstrates that the ILK molecule is involved in the mechanical constriction of VSMCs and has great impact on controlling cell's traction force. The micropost array can locate multipoint of a single cell at one time and the difference of behavior at different location in a single cell can be carefully studied.

7.3 THE STUDY OF TRANSIENT RESPONSE OF VSMC USING PDMS MICROPOST ARRAY

The regular mechanical behavior of the vascular smooth muscle cell is not only reflected by the cell's long term response but also reflected by cell's transient behavior in relatively short period of time. Such transient behavior cannot be observed or studied using flat substrate or traditional tool. The PDMS micropost array is used to detect tiny movement from the vascular smooth muscle cell due to its high sensitivity of deflection and force measurement. The biological experiment using the combination of high aspect ratio PDMS micropost array and fast scanning confocal microscope made it possible to detect transient response of vascular smooth muscle cell in normal situation. Such method has not been reported in any other literature.

It is demonstrated that vascular smooth muscle cell has the regular transient behavior or response in normal conditions. We also found that such regular vibration is not single frequency mechanical movement but the regular vibration with the regular periods of 900 seconds and 500

seconds. Due to the high sensitivity of the micropost, the vibration as small as 200 nm, which is equivalent to 210 pN is detected.

The natural vibration frequency of the VSMC is changed due to the addition of external stimulus such as angiotensin II and Cytochalasin. Both angiotensin II and Cytochalasin has large effect on cell's long vibration period. The vibration period is extended from 900 seconds to 20-30 minutes. The short vibration period keeps relatively constant when there is external stimulus or not. The vibration amplitude can also be changed due to the reaction between cell and external stimulus.

REFERENCE

1. K.Suzuki, and B.W. Smith, “Microlithography: Science and Technology”, **2007**, pp 149-151
2. J. N. Helbert, “Handbook of VLSI Microlithography, 2nd Edition”, **2011**, pp 1-5
3. E. Reichmanis and L. F. Thompson, “Polymer Materials for Microlithography”, Annual Review of Materials Science, Vol. 17: 235-271, **1987**, pp 235-241
4. G. C. Schwartz and P. M. Schaible, “Reactive ion etching of silicon”, Journal of Vacuum Science and Technology, Vol 16, **1979**, pp 410-413
5. F. Laermer and A. Urban, “Challenges, developments and applications of silicon deep reactive ion etching”, MicroElectronic Engineering, Vol 67-68, **2003**, pp 349-355
6. F. Marty, L. Rousseau, B. Saadany, B. Mercier, O. Français, Y. Mita and T. Bourouina, “Advanced etching of silicon based on deep reactive ion etching for silicon high aspect ratio microstructures and three-dimensional micro- and nanostructures”, MicroElectronics Journal, Vol 36, **2005**, pp 673-677
7. W. A. Yarbrough and R. Messier, “Current Issues and Problems in the Chemical Vapor Deposition of Diamond”, Science, Vol. 247, **1990**, pp. 688-696
8. J. R. Conrad, J. L. Radtke, R. A. Dodd, Worzala, J. Frank;Tran, C. Ngoc; “Plasma source ion-implantation technique for surface modification of materials”, Journal of Applied Physics, Vol. 62, **1987**, pp 4591-4596

9. I. Moerman, P.P. Van Daele, P.M. Demeester, “A review on fabrication technologies for the monolithic integration of tapers with III-V semiconductor devices”, IEEE Journal of Selected Topics in Quantum Electronics, Vol. 3, **2002** pp 1308-1320
10. R. G. Poulsen, “Etching in integrated circuit manufacture—A review”, Journal of Vacuum Science and Technology, Vol 14, **1977**, pp 266-274
11. C. H. Tung, T. T. Sheng and C. Y. Lu, “ULSI Semiconductor Technology Atlas”, **2003**, pp 36-49
12. A. J. Chung, Y. S. Huh and D. Erickson, “A robust, electrochemically driven microwell drug delivery system for controlled vasopressin release”, Biomedical Microdevices, Vol. 11, **2009**, pp 861-867
13. M. Du, X. Y. Ye, K. Wu and Z.Y. Zhou, “A Peristaltic Micro Pump Driven by a Rotating Motor with Magnetically Attracted Steel Balls”, Sensors, Vol 9, **2009**, pp 2611-2620
14. M. Shoji, I. Hiroyuki; “Optically driven viscous micropump using a rotating microdisk”, Applied Physics Letters, Volume: 91, **2007**, pp 084101-084101
15. T. W. Lim, Y. Son, Y. J. Jeong, D. Y. Yang, H. J. Kong, K. S. Lee and D. P. Kim, “Three-dimensionally crossing manifold micro-mixer for fast mixing in a short channel length”, Lab on a Chip, Vol. 11, **2011**, pp 100-103
16. P. I Oden, P. G.Datskos, T. Thundat, R. J.Warmack; “Uncooled thermal imaging using a piezoresistive microcantilever”, Applied Physics Letters, Vol. 69, **1996**, pp 3277-3279

17. D. W. Dareing, T. Thundat, S. Jeon, M. Nicholson, “Modal analysis of microcantilever sensors with environmental damping”, *Journal of Applied Physics* Vol. 97, **2005**, pp 084902-084902
18. W. C. Qu, S. K. Islam, M. R. Mahfouz, M. R. Haider, G. To; S. Mostafa; “Microcantilever Array Pressure Measurement System for Biomedical Instrumentation”, *Sensors Journal, IEEE*, Vol. 10, **2010**, pp 321-330
19. G. Meng, W. M. Zhang, H. Huang, H. G. Li and D. Che, “Micro-rotor dynamics for micro-electro-mechanical systems (MEMS)”, *Chaos, Solitons & Fractals*, Vol. 40, **2009**, pp 538-562
20. M. Godin, A. K. Bryan, T. P. Burg, K. Babcock, S. R. Manalis, “Measuring the mass, density, and size of particles and cells using a suspended microchannel resonator”, *Applied Physics Letters*, Vol. 91, **2007**, pp 123121-123121
21. V. Maselli, R. Osellame, G. Cerullo, R. Ramponi, P. Laporta, L. Magagnin, P. L. Cavallotti, “Fabrication of long microchannels with circular cross section using astigmatically shaped femtosecond laser pulses and chemical etching”, *Applied Physics Letters*, Vol. 88, **2006**, pp 191107-191107
22. T. Lemke, J. Kloeker, G. Biancuzzi, T. Huesgen, F. Goldschmidtboeing and P. Woias, “Fabrication of a normally-closed microvalve utilizing lithographically defined silicone micro O-rings *Journal of Micromechanics and Microengineering*”, Vol. 21, **2011**, 025011

23. E. Nuxoll, R. Siegel, “BioMEMS devices for drug delivery”, *Engineering in Medicine and Biology Magazine, IEEE*, Vol. 28, **2009**, pp 31-39
24. M. Ni, W. H. Tong, D. Choudhury, N. A. A. Rahim, C. Iliescu, and H. Yu, “Cell Culture on MEMS Platforms: A Review”, *International Journal of Molecular Sciences*, Vol. 10, **2009**, pp 5411–5441
25. B. Bhushan, *MEMS/NEMS and BioMEMS/BioNEMS: Materials, Devices, and Biomimetics*, Springer Handbook of Nanotechnology, **2010**, pp1664-1683
26. R. Narayan, “BioMEMS general presentation”, *Biomedical Materials*, **2009**, pp 444-470
27. T. Stieglitz, “Development of a micromachined epiretinal vision prosthesis”, *Journal of Neural Engineering*, Vol. 6, 2009, 065005
28. S. Benmerah, S. P. Lacour, E. Tarte, “Design and fabrication of neural implant with thick microchannels based on flexible polymeric materials”, *Annual International Conference of the IEEE*, **2009**, pp 6400-6403
29. J. Held, J. Gaspar, P. Ruther, M. Hagner, A. Cismak, A. Heilmann and O. Paul, “Design of experiment characterization of microneedle fabrication processes based on dry silicon etching”, *Journal of Micromechanics and Microengineering*, Vol. 20, **2010**, 025024
30. M. W. Ashraf, S. Tayyaba, N. Afzulpurkar, T. Lomas, A. Tuantranont, A. Nisar, E. L. J. Bohez, “Design, analysis and fabrication of MEMS-based silicon microneedles for bio-

- medical applications”, Electrical Engineering/Electronics Computer Telecommunications and Information Technology , International Conference , **2010**, pp 950-953
31. S. A. Coulman, A. Anstey, C. Gateley, A. Morrissey, P. McLoughlin, C. Allender and J. C. Birchall, “Microneedle mediated delivery of nanoparticles into human skin”, International Journal of Pharmaceutics, Vol.366, **2009**, pp 190-200
 32. D. Jia and J. Liu, “Human power-based energy harvesting strategies for mobile electronic devices”, Frontiers of Energy and Power Engineering in China, Vol. 3, **2009**, pp 27-46
 33. Y.Zhu, S.O. R. Moheimani, M. R. Yuce, “2-DOF MEMS Ultrasonic Energy Harvester”, IEEE Sensors Journal, Vol. 11, **2011**, pp 155-161
 34. A. K. Harris, P. Wild and D. Stopak, “Silicone Rubber Substrata: A New Wrinkle in the Study of Cell Locomotion”, Science, Vol. 208, **1980**, pp 177-179
 35. A. Tsukamoto, Y. Mitsuoka, T. Watanabe, K. S. Furukawa and T. Ushida, “Analysis of Subcellular Traction Force in Cells under Uniaxial Stretch for Mechanobiology”, IFMBE Proceedings, Vol. 31, **2010**, pp 1129-1132
 36. N. Q. Balaban, U. S. Schwarz, D. Riveline, P. Goichberg, G. Tzur, I. Sabanay, D. Mahalu, S. Safran, A. Bershadsky, L. Addadi and B. Geiger, “Force and focal adhesion assembly: a close relationship studied using elastic micropatterned substrates”, Nature Cell Biology Vol. 3, **2001**, pp 466-472

37. J. L. Tan, J. Tien, D. M. Pirone, D. S. Gray, K. Bhadriraju , C. S. Chen, “Cells lying on a bed of microneedles: An approach to isolate mechanical force”, Proceedings of National Academy Science, Vol.100, **2003**, pp 1484-1489
38. Y. Zhao, C. C. Lim, D. B. Sawyer, R. Liao, X. Zhang, “Cellular force measurements using single-spaced polymeric microstructures: isolating cells from base substrate”, Journal of Micromechanics and Microengineering, Vol. 15, **2005**, pp 1649-1656
39. R. J. Podolsky, T. Hall, and S. L. Hatchett, “Identification of oxalate precipitates in striated muscle fibers”, the journal of general physiology, vol. 48, **1970**, pp 699-702
40. W. S. Parkhouse, “Regulation of skeletal muscle myofibrillar protein degradation: Relationships to fatigue and exercise”, International Journal of Biochemistry, Vol. 20, 1988, pp 769-775
41. S. Yang and M. T. A. Saif, “Microfabricated Force Sensors and Their Applications in the Study of Cell Mechanical Response”, Experimental Mechanics, Vol 49, **2009**, pp 135-151
42. X. L Peng, J. Y. Huang, L. Qin, C. Y. Xiong and J. Fang, “A method to determine Young’s modulus of soft gels for cell adhesion”, Acta Mechanica Sinica, Vol. 25, **2007**, pp 565-570
43. S. Fernandes, H. V. M. Rijen, V. F., S. Evain, A.-L. Leblond, J. Mérot, F. Charpentier, J. M. T. Bakker, P.Larchand, “Cardiac cell therapy: overexpression of connexin43 in skeletal myoblasts and prevention of ventricular arrhythmias”, Journal of Cellular and Molecular Medicine, Vol. 13, **2009**, pp 3703–3712

44. S. Yang and M.T.A. Saif, “Microfabricated Force Sensors and Their Applications in the Study of Cell Mechanical Response”, *Experimental Mechanics*, Vol 49, **2009**, pp135–151
45. K. A. Corin and L. J. Gibson, “Cell contraction forces in scaffolds with varying pore size and cell density”, *Biomaterials*, Vol. 31, 2010, pp 4835-4845
46. M. T Yang, J. Fu, Y. K. Wang, R. A. Desai, C. S. Chen, “Assaying stem cell mechanobiology on microfabricated elastomeric substrates with geometrically modulated rigidity”, *Nature Protocols*, Vol. 6, **2011**, pp 187–213
47. F. M. Sasoglu, A. J. Bohl, K. B. Allen, B. E. Layton, “Parallel force measurement with a polymeric microbeam array using an optical microscope and micromanipulator”, *Computer methods and programs in biomedicine*, Vol 93, 2009, pp 1-8
48. Bin Li, Luke Xie, Z. C. Starr, Z. C. Yang, J. S. Lin, J. H. C. Wang, “Development of micropost force sensor array with culture experiments for determination of cell traction forces”, *Cell Motility and the Cytoskeleton*, Vol. 64, **2007**, pp 509–518
49. Y. C. Lin, C. Kramer, C. Chen, D. Reich, “Dynamics of Traction Force Reinforcement in Smooth Muscle Cells American Physical Society”, *American Physical Society*, **2010**
50. N. J. Sniadecki, C. M. Lamb, Y. Liu, C. S. Chen, and D. H. Reich, “Magnetic microposts for mechanical stimulation of biological cells: Fabrication, characterization, and analysis”, *Review of Scientific Instruments* Vol. 79, **2008**, 044302

51. N. J. Sniadecki and C. S. Chen, "Microfabricated Silicone Elastomeric Post Arrays for Measuring Traction Forces of Adherent Cells", *Methods in Cell Biology*, Vol. 83, **2007**, pp 313-328
52. S. Wojciech, S. T. Waldemar, N. Danz, E. Forester, J. P. Kaiser, A. Bruinink, K. Kurzydłowski, ".Microsensor for Cell Force Measurement" *Sensor Letters*, Vol. 8, **2010** , pp. 736-743
53. Mohamed GadelHak, "The MEMS Handbook: Design and Fabrication", **2006**, pp 9-11
54. A. Bubendorfer, X. M. Liu¹ and A. V Ellis, "Microfabrication of PDMS microchannels using SU-8/PMMA moldings and their sealing to polystyrene substrates", *Smart Materials and Structures*, Vol. 16, **2007**, pp 367-371
55. S. W. Park, J. H. Lee, H. C. Yoon, B. W. Kim, S. J. Sim, H. Chae and S. S. Yang, "Fabrication and testing of a PDMS multi-stacked hand-operated LOC for use in portable immunosensing systems", *BioMedical Microdevices*, **2008**, s10544-008-9200-9
56. W. T. Gerthoffer, "Mechanisms of Vascular Smooth Muscle Cell Migration", *Circulation Research*, Vol. 100, **2007**, pp 607-621
57. E. Q. Scherer, "Sphingosine-1-phosphate modulates spiral modiolar artery tone: A potential role in vascular-based inner ear pathologies?", *Cardiovasc Research*, Vol. 70, **2006**, pp79–87

58. E. T. Yeh, S. Zhang, H.D. Wu, M. Korbling, J. T. Willerson and Z. Estrov, “Transdifferentiation of human peripheral blood CD34₊-enriched cell population into cardiomyocytes, endothelial cells, and smooth muscle cells in vivo”, *Circulation*, Vol. 108, **2003**, pp 2070–2073
59. C. E. Murry, C. T. Gipaya, T. Bartosek, E. P. Benditt and S. M. Schwartz, “Monoclonality of smooth muscle cells in human atherosclerosis”, *The American Journal of pathology*, Vol. 151, **1997**, pp 697–705
60. M. A. Reidy, “Factors controlling smooth-muscle cell proliferation”, *Archives of Pathology & Laboratory Medicine*, Vol. 116, **1992**, pp 1276–1280.
61. A. Jawien, D. F. Bowen-Pope, V. Lindner, S. M. Schwartz, A. W. Clowes, “Platelet-derived growth factor promotes smooth muscle migration and intimal thickening in a rat model of balloon angioplasty”, *The journal of clinic investigation*, Vol. 89, **1992**, pp 507-511
62. S. R. Peyton, A. J. Putnam, “Extracellular matrix rigidity governs smooth muscle cell motility in a biphasic fashion”, *The journal of cell physiology*, Vol. 204, **2005**, pp 198-209.
63. M. R. Ward, R. S. Tsao, A. Agrotis, R. J. Dilley, G. L. Jennings, A. Bobik, “Low blood flow after angioplasty augments mechanisms of restenosis: inward vessel remodeling, cell migration, and activity of genes regulating migration”, *Arteriosclerosis, thrombosis, and vascular Biology*, Vol. 21, **2001**, pp 208-213

64. M. Hellstrom, M. Kalen, P. Lindahl, A. Abramsson, C. Betsholtz, "Role of PDGF-B and PDGFR-beta in recruitment of vascular smooth muscle cells and pericytes during embryonic blood vessel formation in the mouse", *Development*, Vol. 126, **1999**, pp 3047–3055
65. L. Liaw, M. Almeida, C. E. Hart, S. M. Schwartz and C. M. Giachelli, "Osteopontin promotes vascular cell adhesion and spreading and is chemotactic for smooth muscle cells in vitro", *Circular Research*, Vol. 74, **1994**, pp 214-224
66. J. T. Parsons, "Focal adhesion kinase: the first ten years", *Journal of cell science*, Vol. 116, **2003**, pp 1409-1416
67. R. Z. Bar, M. Cohen, L. Addadi and B. Geiger, "Hierarchical assembly of cell-matrix adhesion complexes", *Biochemical Society Transactions*, Vol. 32, 2004, pp 416-420
68. C. R. Hauck, D. A. Hsia, D. D. Schlaepfer, "Focal adhesion kinase facilitates platelet-derived growth factor-BB-stimulated ERK2 activation required for chemotaxis migration of vascular smooth muscle cells", *Journal of Biological Chemistry*, Vol. 275, 2000, pp 41092-41099
69. S. S. Okada, J. E. Tomaszewski, E. S. Barnathan, "Migrating vascular smooth muscle cells polarize cell surface urokinase receptors after injury in vitro", *Experimental Cell Research*, Vol. 217, **1995**, pp 180-187

70. H. Abedi, K. E. Dawes, I. Zachary, "Differential effects of platelet-derived growth factor BB on p125 focal adhesion kinase and paxillin tyrosine phosphorylation and on cell migration in rabbit aortic vascular smooth muscle cells and Swiss 3T3 fibroblasts", *Journal of Biological Chemistry*, Vol. 270, **1995**, pp 11367-11376
71. B. Jiang, S. Yamamura, P. R. Nelson, L. Mureebe, K. C. Kent. "Differential effects of platelet-derived growth factor isotypes on human smooth muscle cell proliferation and migration are mediated by distinct signaling pathways", *Surgery*, Vol. 120, **1996**, pp 427-431
72. C. Wu, and S. Dedhar, "Integrin-linked kinase (ILK) and its interactors: a new paradigm for the coupling of extracellular matrix to actin cytoskeleton and signaling complexes", *The journal of cell biology*, Vol. 155, **2001**, pp 505-510
73. S. N. Nikolopoulos, C. E. Turner, "Integrin-linked kinase (ILK) binding to paxillin LD1 motif regulates ILK localization to focal adhesions", *The journal of biological chemistry*, Vol. 276, **2001**, pp 23499-23505
74. J. T. Deng, C. Sutherland, D. L. Brautigan, M. Eto, M. P. Walsh, "Phosphorylation of the myosin phosphatase inhibitors, CPI-17 and PHI-1, by integrin-linked kinase", *Biochemistry journal*, Vol. 367, **2002**, pp 517-524
75. E. Cukierman, R. Pankov, D. R. Stevens, K. M. Yamada, "Taking cell-matrix adhesions to the third dimension", *Science*, Vol. 294, **2001**, pp 1708-1712

76. M. H. Zaman, L. M. Trapani, A. L. Sieminski, D. Mackellar, H. K. Gong, A. Wells, D. A. Lauffenburger, P. Matsudaira, "Migration of tumor cells in 3D matrices is governed by matrix stiffness along with cell matrix adhesion and proteolysis", .Proceedings of National Academy Science, Vol. 103, **2006**, pp 10889-10894
77. D. Dormann, C. J. Weijer, "Imaging of cell migration", EMBO Journal, Vol 25, **2006**, pp 3480-3493
78. J. Lee, M. Leonard, T. Oliver, A. Ishihara, K. Jacobson, "Traction forces generated by locomoting keratocytes", Journal of Cell Biology, Vol. 127 ,**1994**, pp 1957-1964
79. K. Burton, D. L. Taylor, "Traction forces of cytokinesis measured with optically modified elastic substrata", Nature, Vol. 385, **1997**, pp. 450-454
80. N. Wang, E. Ostuni, G. M. Whitesides, D. E. Ingber, "Micropatterning tractional forces in living cells", Cell Motil Cytoskeleton Vol. 52, **2002**, pp 97-106
81. K. A. Beningo, C. M. Lo, Y. L. Wang "Flexible polyacrylamide substrata for the analysis of mechanical interactions at cellsubstratum adhesions", Methods of Cell Biology, Vol. 69, **2002**, pp 325-339
82. N. J. Sniadecki, A. Anguelouch, M. T. Yang, C. M. Lamb, Z. Liu, S. B. Kirschner, Y. Liu, D. H. Reich, C. S. Chen, "Magnetic microposts as an approach to apply forces to living cells," PNAS, Vol. 104, **2007**, pp14553-14558

83. O. du Roure, A. Saez, A. Buguin, R. H. Austin, P. Chavrier, P. Silberzan, B. Ladoux, "Force mapping in epithelial cell migration," *Proceedings of National Academy Science*, Vol. 102, **2005**, pp 2390-2395
84. C. A. Lemmon, N. J. Sniadecki, S. A. Ruiz, J. L. Tan, L. H. Romer, C. S. Chen, "Shear force at the cell-matrix interface: Enhanced analysis for microfabricated post array detectors", *Mechanics and Chemistry of Biosystem*, Vol. 2, **2005**, pp. 1–16
85. A. Saez, A. Buguin, P. Silberzan, B. Ladoux, "Is the mechanical activity of epithelial cells controlled by deformations or forces?", *Biophysics Journal*, Vol. 89, **2005**, pp. L52–L54
86. Y. Zhao, X. Zhang, "Adaptation of flexible polymer fabrication to cellular mechanics study", *Applied Physics Letter*, Vol. 87, **2005** 144101
87. B. E. Layton, K. B. Allen, M. D. Stokes, K. A. Myers, P. W. Baas, "Towards a method for peripheral nervous system axonal stiffness measurements with mems-based microgrippers", *2nd Annual IEEE-EMBS Conference on Neural Engineering*, 2005
88. F. M. Sasoglu, A. J. Bohl, B. E. Layton, "Design and microfabrication of a high-aspect-ratio PDMS microbeam array for parallel nanonewton force measurement and protein printing", *Journal of Micromechanics and Microengineering*, Vol. 17, **2007**, pp. 623-632
89. C.W. Wang, W.R. Chen, C. C. Wu, H. C. Chang," "Study on the Cell Mechanics of MDCK Cells by Elastic Micro-pillars Arrays", *IEEE International Conference on Nano/Micro Engineered and Molecular Systems*, **2007**, pp.1125-1128

90. J. Park, J. Ryu, S. K. Choi, E. Seo, J. M. Cha, S. Ryu, J. Kim, B. Kim, S. H. Lee, "Real-time measurement of the contractile forces of self-organized cardiomyocytes on hybrid biopolymer microcantilevers", *Analytical Chemistry*, Vol. 77, **2005**, pp 6571-6580
91. F. P Miller, A. F. Vandome, J. McBrewster, *Deep Reactive-Ion Etching*, 2010, pp 12-28
92. Y. Fainman, D. Psaltis, "Optofluidics: fundamentals, devices, and applications", **2009**, pp 8-20
93. L. Kuo, W. M. Chilian, et al., "Coronary arteriolar myogenic response is independent of endothelium," *Circulation Research*, Vol. 66, **1990**, pp. 860-866
94. J. C. Falcone, M. J. Davis, et al., "Endothelial independence of myogenic response in isolated skeletal muscle arterioles." *The American journal of Physiology*, Vol. 260, **1991**, pp H130-H135
95. B. Williams, "Mechanical influences on vascular smooth muscle cell function", *Journal of Hypertens*, Vol. 16, **1998**, pp 1921-1929
96. F. J. Alenghat, D. E. Ingber, "Mechanotransduction: all signals point to cytoskeleton, matrix, and integrins", *Sci STKE*, Vol. 119, **2002**, PE6
97. Q. Cheng, Z. Sun, G. A Meininger and M. Almasri, "Note: Mechanical study of micromachined polydimethylsiloxane elastic microposts", *Review of Scientific Instrument*, Vol. 81, **2010**, 106104(2010)

VITA

Qi Cheng received the B.Sc. and M.Sc. degrees from Nanjing University of Science and Technology, Nanjing, China, in 2000 and 2003, respectively, and the M.Sc. degree from the Royal Institute of Technology (KTH), Sweden in 2006, all in electrical engineering. He received the Ph.D. degree in electrical engineering at the University of Missouri, Columbia. His research interests during Ph. D. study include MEMS and bioMEMS design and fabrication, characterization of infrared sensing material silicon germanium oxide thin film (SiGeO), optical, thermal, and mechanical design and modeling of uncooled tunable microbolometers for infrared detection, and micropost array. He is currently joining the Intel Cooperation and working on semiconductor manufacturing and process technology development.